ANTHRACENE-BASED MOLECULES FOR ORGANIC THIN-FILM TRANSISTOR INTEGRATION

BY:

MIKHAIL VORONA

A THESIS

SUBMITTED TO THE UNIVERSITY OF OTTAWA

IN PARTIAL FULFILMENT OF THE REQUIREMENTS FOR THE

MASTER OF APPLIED SCIENCE DEGREE

IN CHEMICAL ENGINEERING

DEPARTMENT OF CHEMICAL AND BIOLOGICAL ENGINEERING

UNIVERSITY OF OTTAWA

MASc in Chemical Engineering (2020) University of Ottawa

Chemical and Biological Engineering Ottawa, Ontario, Canada

TITLE: Anthracene-based Molecules for Organic Thin-Film Transistor Integration

AUTHOR: Mikhail Yuriyevich Vorona

B.A.Sc, (Chemical Engineering)

University of Toronto (Toronto, Ontario, Canada)

SUPERVISOR: Prof. Benoît H. Lessard

NUMBER OF PAGES: xx, 84

Abstract:

Organic electronics are devices based on semiconductors derived from carbon based molecules and polymers. These devices can be made flexible, lightweight and potentially inexpensive with the development of economies of scale. Specific examples of organic electronics include organic thin-film transistors (OTFTs), organic light-emitting diodes (OLEDs) and organic photovoltaic (OPVs). Anthracene-based semiconductors are materials that have generated great interest primarily because of their structural planarity, potential for strong intermolecular interactions, air stability and ideal frontier molecular orbital energy levels. In this thesis, we detail two publications that examined functionalized anthracene molecules integrated into OTFTs, along with their thermal, electrochemical and optical properties. We started by examining seven novel 9,10-anthracene-based molecules. It was found that functionalization of the 9,10-positions with different phenyl derivatives resulted in negligible variation in the optical properties with minor (±0.10 eV) changes in electrochemical behaviour, while the choice of phenyl derivative greatly affected the thermal stability whereby the decomposition temperatures (T_d) varied by as much as 128 °C between certain functionalized derivatives. The findings suggested that functionalization of the 9,10-position of anthracene leads to an effective handle for tuning of the thermal stability while having little to no effect on the optical properties and the solid-state arrangement. We continued with the synthesis of several novel anthracene derivatives which were di-substituted at the 2,6-positions. It was found that 2,6-functionalization with various fluorinated phenyl derivatives led to negligible changes in the optical behaviour while influencing the electrochemical properties (±0.10 eV). Furthermore, the choice of fluorinated phenyl moiety had noticeable effects on melting point and thermal stability ($\Delta T_m < 55$ °C and $\Delta T_d < 65$ °C). OTFTs were fabricated and characterized using the 2,6-anthracene derivatives as the semiconducting layer. The addition of fluorine groups on the phenyl groups led to a transition from p-type behaviour to n-type behaviour in BGBC OTFTs. The results indicated that the choice of functional group as well as its functionalization location, at the 9,10- and 2,6-positions, can act as powerful handles to engineer high performance OTFTs.

Acknowledgments:

I would like to extend my sincere gratitude to Prof. Benoît H. Lessard for providing me with the opportunity to join his research group at the University of Ottawa. Without his faith in my abilities, trust, and patience, none of this would be possible. It is only through his leadership and effort that am able to attain this advanced engineering degree.

I have no doubt that the Lessard Research Group will continue to strive for excellence in the many years to come. I feel deeply proud to have been a part of the group and I am privileged to have worked with so many talented colleagues, many of whom I am honored to call friends.

I would also like to acknowledge and thank Prof. Jaclyn L. Brusso, Dr. Nathan J. Yutronkie and Dr. Owen A. Melville for their guidance in helping me publish my first two papers. Their insight into the subject matter I covered proved to be invaluable.

OTI Lumionics Inc. had placed their trust in me through Prof. Benoît H. Lessard and this allowed me to pursue my research to the fullest extent possible, for which I am also deeply grateful.

I would like to express my appreciation to Gabs, my parents, and my friends that have supported me along the way of achieving this advanced degree.

Thanks to the administrative and technical staff at University of Ottawa Department of Chemical and Biological Engineering for their administrative and technical support.

Thank you to the thesis committee for your consideration of this report.

Table of Contents:

1.0 Introduction:

Anthracene was first synthetically derived and characterized in 1832 [1]. Subsequent purification process developments enabled anthracene to be industrially produced as a petrochemical dye [2]. In 1953, Mette et al. observed that anthracene exhibits blue fluorescence under ultra-violet radiation [1, 2]. In subsequent years, anthracene became the first organic material to be studied for electrical charge conductivity [3,]. By the early 2000s, anthracene-based derivatives became dominant molecules in OTFTs and OLEDs with charge mobilites as high as 1.0 $cm^2\ V^{-1}s^{-1}$, respectively by the early-2000s [4, 5].

An anthracene molecule can be substituted with functional groups at ten positions along the periphery of the core in order to tailor the molecule (Figure 1). Since 2013, there has been a surge in anthracene-based semiconductor research, with over 150 derivatives have been synthesized, providing the footings for developing various structure-property-mobility relationships [6-9]. 2,6-diphenyl anthracene (DPA) has afforded the highest p-type mobilities yet, with 14.8 $cm^2\ V^{-1}s^{-1}$ in OTFTs and 34.0 $cm^2\ V^{-1}s^{-1}$ in organic single-crystal transistors [6, 7]. Charge mobility can be traced from three key factors: (1) the energy level, whereby the alignment of the semiconductor E_{HOMO} or E_{LUMO} levels with the Fermi level of the source or drain electrodes define charge injection barriers; (2) the stacking motif, whereby the packing style plays a significant role in charge transport ability; and (3) the thin film morphology, whereby an ordered stacking structure and dense grains with few boundaries and traps reduce the obstruction for charge transport.

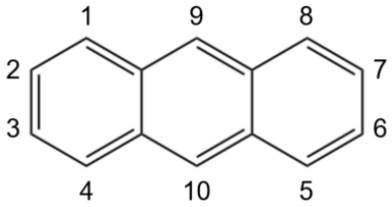

Figure 1: The anthracene molecule. The labelled 2-, 3-, 6-, 7- locations are known as the *end*-positions, and 1-, 4-, 5-, 8-, 9-, 10- locations are known as the *peri*-positions.

In the last five years, considerable effort has been devoted to researching anthracene functionalized at the 2,6-, 9,10-, and 2,6,9,10- positions because they have afforded the highest mobilities [6-9]. Accordingly, these studies suggest that symmetrical structures correlate best to crystallinity, and thus, good charge mobilities. In some cases a symmetrical structure is not beneficial, such as for

2-substitued derivatives, because an asymmetric structure has a positive effect on crystallinity and mobility measurements [9]. Many of the substitute attachments have been aryl moieties as this extends the π-π conjugated network and can offer better molecular overlap, like in the cases of 2,6-DPA, 9,10-DPA, and 2,6,9,10-DPA [9-10].

Chemistry of Anthracene-Based Molecules: The Suzuki-Miyaura Cross-Coupling Reaction

We can obtain high mobility OTFTs by increasing the overall conjugation (π-electron delocalization) and by arranging the anthracene-based molecules in a thin-film more favourably [11-13]. This ultimately leads to greater π-π stacking between adjacent molecules [12, 13]. By modifying anthracene using chemical mechanisms such as the Suzuki coupling reaction, aryl groups may be added to anthracene to extend its π-electron system and adjust the molecular packing motif.

The palladium-catalyzed Suzuki-Miyaura cross-coupling reaction is one of the most versatile and frequently employed methods for carbon-carbon bond formation in academia and industry [14, 15]. It is a particularly powerful synthetic strategy for the construction of numerous pharmaceuticals, agrochemicals, and even some polymers [10, 16-19]. The Suzuki reaction consists of the coupling of organoboron compounds with aryl, alkenyl, and alkynyl halides (core) in the presence of an alkaline salt and a homogeneous palladium catalyst, typically a phenyl ligand (Scheme 1) [20-22]. Many boronic acids, which are a class of organoboron compounds, are commercially available for use in cross-coupling reactions.

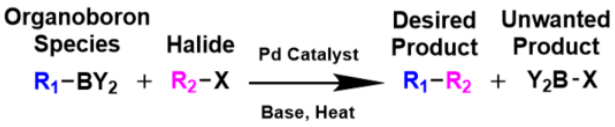

Scheme 1: Suzuki-Miyaura cross-coupling scheme for the functionalization of halides (core) and organoboron species (boronic acid).

Suzuki coupling reactions are usually conducted in an organic medium or in a biphasic organic–aqueous media. There are a number of solvents that can enable the reaction, such as n-methyl-2-pyrrolidone (NMP), dimethylformamide (DMF), dioxane, and tetrahydrohuran (THF) or toluene [23]. The solvent choice is dependent on the dissolution of the reagents being used and the temperature of reaction. However, typically ~10 v/v% of water should be present in the solvent mixture to adequately dissolve the alkaline salt, which is crucial for the transmetalation step of the coupling mechanism. Current chemistry research focuses on eliminating the use of ligand catalytic systems (employing $Pd(OAc)_2$ and $PdCl_2$) and using environmentally benign solvents such as water or ionic liquids [20-25].

In the synthesis of anthracene-based molecules, the core anthracene molecule would be brominated and would constitute the aryl halide species. The moiety that would be used to functionalize a core anthracene molecule would be found on the arylboronic acid. The reaction would be catalyzed by stoichiometric quantities of tetrakis(triphenylphosphine)palladium(0) ($Pd(PPh_3)_4$) in the presence of an added alkaline salt, namely potassium carbonate (K_2CO_3). Suzuki coupling reactions are air sensitive, as the $Pd(PPh_3)_4$ catalyst readily oxidizes, reducing their efficacy. Therefore, all reagents must be degassed/sparged of air prior to mixing [24, 25].

Properties of Anthracene-Based Molecules: Electrochemical, Optimal, Thermal, Thin Film Packing Properties

There are a number of unique properties of anthracene-based molecules that make them highly desirable for electrical applications. Researchers have discovered that the $\boldsymbol{T_d}$ of most anthracene-based molecules ranges from 300°C to 500°C [25-29]. This decomposition temperature allows for physical vapour deposition to safely be used as a thin-film deposition fabrication technique. 2-substituted and 2,6-substituted derivatives typically have E_{HOMO} levels around -5.50 eV (indicating good air stability), and 9,10-substituted and 1,5-substituted derivatives have E_{HOMO} levels of -5.25 eV [25-27]. This allows 9,10-substituted and 1,5-substituted derivatives to align well with Au Fermi level of -5.10 eV (source and drain electrodes) [26-28]. These molecules tend to be p-conductor dominant. Lastly, most anthracene-based OTFTs have optical band gaps (E_g) of 2.70-2.90 eV, whereas 2,6,9,10-substituted derivatives are bathochromic (red) shifted to 2.18-2.38 eV, due to more electron-rich (electron-donating) functional elements [25-30]. Accordingly, the excitation peaks resemble a three-finger shaped absorption, at 420 nm, 395 nm, and 375nm (in

thin film). The thin film packing structure of anthracene-based molecules tend to considerably vary with the peripheral positions that are functionalized [25-30]. Examining packing can reveal the nature of intermolecular interactions, as it relates to charge transfer in an OSC. A dense packing motif of anthracene molecules, particularly of the conjugated centres, translates to increased charge transfer integrals and higher mobilities.

Anthracene, like most aromatic compounds, tends to adopt herringbone packing to increase the intermolecular van der Waals forces, maximize the stacking density, and lower the energy state [10]. The packing styles are: (1) herringbone style I (without face-to-face overlap between the adjacent molecules); (2) herringbone style II (with face-to-face overlap between the adjacent molecules); (3) lamellar style I (slipped stacking); and (4) lamellar style II (bricklayer stacking) [10].

The analysis of the packing motifs can be performed by single-crystal X-ray diffraction (SC-XRD), whereby the exact crystalline arrangement can be identified. However, fabricated OTFTs do not arrange themselves in pure crystalline structures. Instead, fabricated OTFTs arrange themselves in poly-crystalline structures, which combine amorphous and crystalline regions. Therefore, atomic force microscopy (AFM) may be employed to analyze crystallinity, uniformity, and overall quality of a thin-film. AFM may also be used to analyze film quality of totally crystalline films, such as the ones used in organic single-crystal transistors (OSCTs).

Anthracene derivatives substituted at the 9,10-position challenge the regular herringbone stacking observed in 2,6-functionalized derivatives and tend to form a more overlapped lamellar structure [7-8]. Only a small handful of 9,10-position anthracene molecules have been reported to date; all with modest charge mobilities [9]. Researchers have functionalized anthracene at the 2,6-positions with phenyl, 4-trifluoromethylphenyl, 4-methoxyphenyl, 4-ethylphenyl, 4-thiophene, as well as a number of other groups. All of these devices performed well when characterized with mobilities on the order of 10^{-1}-10^{1} $cm^2 V^{-1} s^{-1}$ [9]. 2,6-diphenyl anthracene (DPA) reached the highest p-type mobilities yet, with 14.8 $cm^2 V^{-1} s^{-1}$ in OTFTs and 34.0 $cm^2 V^{-1}s^{-1}$ in a single crystal OTFT device [7, 8].

Organic Electronics and Organic Thin-Film Transistors (OTFTs)

Organic thin-film transistors (OTFTs) are three-terminal electrical devices that consist of a thin-film organic semiconducting (OSC) layer that is separated from a gate electrode by a layer of electronically insulating material (Figure 2). OTFTs can be integrated into flexible lightweight substrates and can be manufactured at lower temperatures and lower cost compared to conventional silicon-based transistors. For instance, OTFTs may be used as effective sensors to detect certain gases or to measure biomedical diagnostics critical for patient monitoring [31-33].

Typical gate electrodes would be made of pure silicon and the dielectric would be made of silicon oxide (SiO_2). The region between the source and drain electrodes is called the channel, which possesses a width (***W***) given by the width of the electrodes and length (***L***) representing the distance between the electrodes.

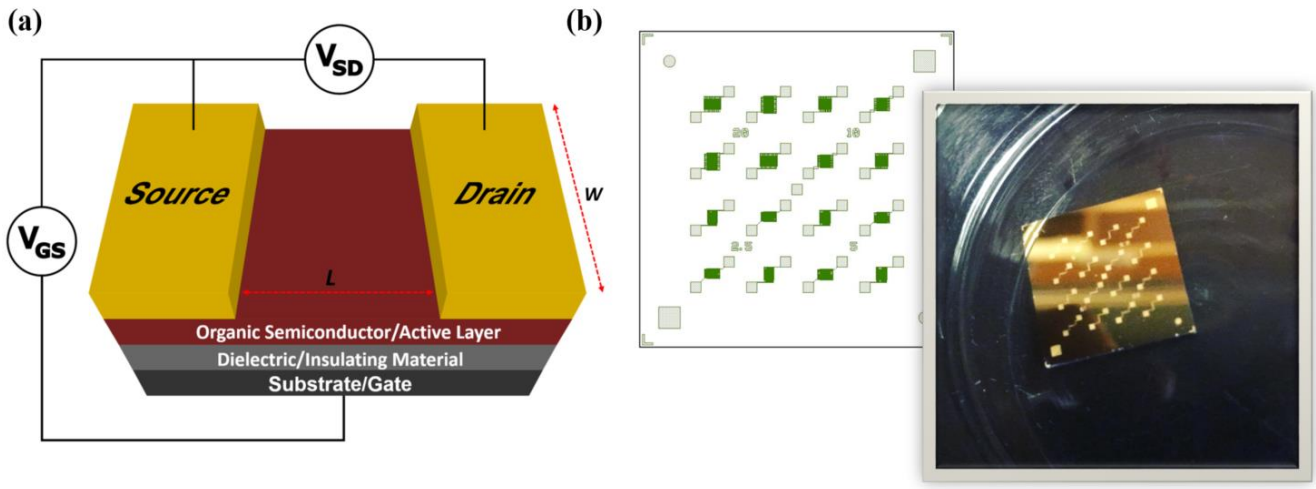

Figure 2: (a) Basic structure of an OTFT in bottom gate top contact configuration (BGTC), with the channel length given by ***L*** and the channel width given by ***W***. (b) BGBC (Fraunhofer pre-fabricated chip) with 16 devices positions there are four varying channel lengths (2.5 µm, 5.0 µm, 10.0 µm and 20 µm).

The source electrode is grounded, and thus, can be used as the reference for the voltage applied to the gate and drain electrodes. The difference in potential between the gate and the source is termed as the gate-source voltage, $\boldsymbol{V_{GS}}$, commonly referred to as the gate voltage. In a similar fashion, the difference in potential between the drain and source is termed the drain-source voltage, $\boldsymbol{V_{DS}}$, commonly referred to as the drain voltage. Additionally, the currents of each electrode (source $\boldsymbol{I_S}$,

drain $\boldsymbol{I_D}$, gate $\boldsymbol{I_G}$) are defined as being positive if they flow into the device and the sum of all three currents is zero, according to Kirchoff's Circuit Laws [34, 35]. There are four different OTFT architectures, depending on the position of the electrodes relative to the active layer. The stack of layers is either placed with the gate electrode at the bottom (bottom-gate), or at the top (top-gate). Likewise, the source and drain electrodes are either placed on top of the semiconductor (top-contact) or beneath the semiconductor (bottom-contact). Each of these structures exhibits different benefits and drawbacks [34, 35]. Additionally, it should be noted that different OTFT structures fabricated using the same materials but different architectures can display different device characteristics [34]. When quantifying the performance of an OTFT, two characteristics are important: charge mobility (μ) and threshold voltage (V_T). The mobility (in $cm^2\ V^{-1}s^{-1}$) is a measurement of how easily holes or electrons move in a p-type and n-type semiconductor, respectively. The threshold voltage (in Volts) indicates the ease with which charge can be injected into the semiconductor from the electrodes, whereby electrons will be injected into the lowest unoccupied molecular orbital (E_{LUMO}) and holes into the highest occupied molecular orbital (E_{HOMO}). For this thesis, we will be focused on either BGBC or BGTC for simplicity and ease of electrical performance comparison.

OTFT Fabrication Techniques: Thermal Evaporation vs. Solution Processing

Physical vapour deposition (PVD) by thermal evaporation is a technique used to develop thin-films and coatings of organic or inorganic materials. In PVD, a material is heated to its sublimation temperature in a vacuum chamber ($<10^{-6}$ Torr), whereby the vapour of the material will condense onto a substrate at a controllable rate. All materials have both a unique sublimation temperature (which is a function of pressure) and a decomposition temperature ($\boldsymbol{T_d}$) (material dependent). It is therefore critical that the processing temperature is selected between the two temperatures above to avoid loss of yield and off-spec electronics, $\boldsymbol{T_d}$ is determined by thermogravimetric analysis (TGA). The sublimation temperature of most organic materials is under 350 ^oC, while the decomposition temperature is highly dependent on the structure and can vary from 50 ^oC to >500 ^oC. There are a number of factors we can control that affect thin-film formation, including substrate temperature, the distance from the source to the substrate, heating and rotation speed of the substrate stage, and the rate of deposition [36-38].

Solution processing techniques such as spin coating and drop casting can only be used on materials that are soluble in a specific solvent or have solubilizing chains that can aid in dissolution. Spin coating is a simple laboratory-scale method whereby the spin rate, substrate surface energy, concentration, and deposition method affect the thickness and consistency of the thin film. Furthermore, the solvent, annealing temperature and time, and substrate treatment and type will also affect the microstructure of the film, which in turn affects the performance of an OTFT [39].

In spin coating by the *dynamic method*, substrates are vacuum-secured on the spinner, the motor is set to a particular rotational speed, and the solution containing the dissolved OSC is deposited onto the rotating substrate allowing to be wicked-off. In the *static method*, the solution is deposited onto the substrate and then the motor is turned on to centrifugally disperse the solution, forming a thin film when dried. In drop casting, the solution is deposited onto a substrate and the solvent is allowed to evaporate. Solution processing methods have the potential to be extremely low cost and applied on a large-scale compared to vacuum-based methods [39, 40]. On the other hand, the highest performing devices, including anthracene-based OTFTs, have all been produced by PVD [34]. PVD tends to result in better quality thin-films due to the high degree of control over the deposition parameters, such as the rate of molecule deposition on the substrate and the temperature of the substrate holder. In the case of solution processing, it is more difficult to consistently control all variables that would contribute to thin-film quality, leading to a diminished performance. For the context of OTFT development, a compromise must be reached wherein cost and performance are adjusted and optimized accordingly.

References

1. H. Mette and H. Pick, Z. “On the Nature of the Electrode Effects in the Conductivity of Anthracene,” Monocrystals. Phys., 1953, 134, 566.
2. M. Yoshizawa and J. K. Klosterman. “Molecular architectures of multi-anthracene assemblies,” Chem. Soc. Rev., 2014, 43, 1885–1898.
3. J. V. Damme and F. D. Prez. “Anthracene-containing polymers toward high-end applications,” Prog. Polym. Sci., 2018.
4. M.-H. Ho, B. Balaganesan and C. H. F. Chen, Isr. “Blue Fluorescence and Bipolar Transport Materials Based on Anthracene and Their Application in OLEDs,” J. Chem., 2012, 52, 484–495.
5. A. N. Aleshin, J. Y. Lee, S. W. Chu, J. S. Kim and Y. W. Park. “Mobility studies of field-effect transistor structures basedon anthracene single crystals,” Appl. Phys. Lett., 2004, 84, 5383–5385.
6. R. M. Glaeser and R. S. Berry. “Mobilities of electrons and holes in organic molecular solids. Comparison of band and hopping models,” J. Chem. Phys., 1966, 44, 3797–3810.
7. J. Liu, H. Dong, Z. Wang, D. Ji, C. Cheng, H. Geng, H. Zhang, Y. Zhen, L. Jiang, H. Fu, Z. Bo,W. Chen, Z. Shuai and W. Hu, “Thin film field-effect transistors of 2,6-diphenylanthracene (DPA),” Chem. Commun., 2015, 51, 11777–11779.
8. J. Liu, H. Zhang, H. Dong, L. Meng, L. Jiang, L. Jiang, Y. Wang, J. Yu, Y. Sun, W. Hu and A. J. Heeger. “High mobility emissive organic semiconductor,” Nat. Commun., 2015, 6, 10032.
9. M. Chen, L. Yan, Y. Zhao, We. Murtaza, H. Meng, and W. Huang. “Anthracene-based semiconductors for organic field-effect transistor,” J. Mater. Chem. C, 2018, 6, 7416.
10. T. Yokozawa, H. Kohno, Y. Ohta, A. Yokoyama. “Catalyst-Transfer Suzuki−Miyaura Coupling Polymerization for Precision Synthesis of Poly(p-phenylene),” Macromolecules. 2010, 7095.
11. A. Dadvand, A. G. Moiseev, K. Sawabe, W.-H. Sun, B. Djukic, I. Chung, T. Takenobu, F. Rosei and D. F. Perepichka. “Maximizing Field-Effect Mobility and Solid-State Luminescence in Organic Semiconductors,” Angew. Chem., Int. Ed., 2012, 51, 3837–3841.

12. A. N. Aleshin, J. Y. Lee, S. W. Chu, J. S. Kim, and Y. W. Park. “Mobility studies of field-effect transistor structures basedon anthracene single crystals,” Appl. Phys. Lett., 2004, 84, 5383–5385.
13. Y. J. Jang, B. T. Lim, S. B. Yoon, H. J. Choi, J. U. Ha, D. S. Chung and S.-G. Lee. “A Small Molecule Composed of Anthracene and Thienothiophene Devised for High-Performance Optoelectronic Applications,” Dyes Pigm., 2015, 120, 30–36.
14. G. B. Smith, G. C. Dezeny, D. L. Hughes, A. O. King, and T. R. Verhoeven. “Mechanistic Studies of the Suzuki Cross-Coupling Reaction,” J. Org. Chem. 1994, 59, 8151.
15. M. N. Zafar, M. A. Mohsin, M. Danish, M. F. Nazar, S. Murtaza, Russ. “Palladium catalyzed Heck-Mizoroki and Suzuki-Miyaura coupling reactions (Review),” J. Coord. Chem. 2014, 40, 781.
16. A. K. Leone, E. A. Mueller, A. J. McNeil. “The History of Palladium-Catalyzed Cross-Couplings Should Inspire the Future of Catalyst-Transfer Polymerization,” Journal of the American Chemical Society 2018, 140 (45). 15126-15139.
17. K. M. Bullock, M. B. Mitchell, J. F. Toczko, and N. Carolina. “Optimization and Scale-Up of a Suzuki−Miyaura Coupling Reaction: Development of an Efficient Palladium Removal Technique,” Org. Process Res. Dev. 2008, 896.
18. P., Leszczyński, T., Hofman, and A., Sporzyński. “Solubility of Phenylboronic Acid and its Cyclic Esters in Organic Solvents,” J Solution Chem 2020, 49, 814–824.
19. Y. Liu, X. Chen, J. Qin, G. Yu, and Y. Liu. “Polymer (Guildf). New linear π-conjugated polymers via Suzuki coupling of (1Z, 3Z)-1,4-dibromo-1,4-diaryl-buta-1,3-diene with aromatic diborates: Synthesis and photophysical properties,” Poly. 51. 2010, 51, 3730.
20. N., Miyaura.; Suzuki, A. “Palladium-Catalyzed Cross-Coupling Reactions of Organoboron Compounds,” Chem. Rev. 1995, 95, 2457.
21. A. J., Suzuki. “Recent advances in the cross-coupling reactions of organoboron derivatives with organic electrophiles,” 1995–1998. Organomet. Chem. 1999, 576, 147.
22. A. F., Little, and G. C. Fu. “Palladium-Catalyzed Coupling Reactions of Aryl Chlorides,” Angew. Chem., Int. Ed. 2002, 41, 4177.
23. C. Mateos, J. A. Rincón, B. J., Martín-hidalgo, and J. Villanueva. “Green and scalable procedure for extremely fast ligandless Suzuki-Miyaura cross-coupling reactions in aqueous IPA using solid-supported Pd in continuous flow,” Tetrahedron Lett. 2014, 55, 3701.

24. A. J. Lennox and G. C. Lloyd-jones. "Transmetalation in the Suzuki–Miyaura Coupling: The Fork in the Trail," Angew. Chem. Int. Ed. 2013, 52, 7362 – 7370
25. Z. Li, W., Gelbaum, W., Heaner, W. Fisk, J., Jaganathan, A., Holden, B., Pollet, P. C., Liotta. "Palladium-Catalyzed Suzuki Reactions in Water with No Added Ligand: Effects of Reaction Scale, Temperature, pH of Aqueous Phase, and Substrate Structure," Org. Process Res. Dev. 2016. 20, 8. 1489-1499
26. L. Yan, Y. Zhao, H. Yu, Z. Hu, Y. He, A. Li, O. Goto, C. Yan, T. Chen, R. Chen, Y.-L. Loo, D. F. Perepichka, H. Meng and W. Huang. "Influence of heteroatoms on the charge mobility of anthracene derivatives," J. Mater. Chem. C, 2016, 4, 3517–3522.
27. J.-H. Park, D. H. Lee, H. Kong, M.-J. Park, We. H. Jung, C. E. Park and H.-K. Shim. "Organic thin-film transistor properties and the structural relationships between various aromatic end-capped triisopropylsilylethynyl anthracene derivatives," Org. Electron., 2010, 11, 820–830.
28. M. Chen, Y. Zhao, L. Yan, S. Yang, Y. Zhu, We. Murtaza, G. He, H. Meng and W. Huang, "A Unique Blend of 2-Fluorenyl-2-anthracene and 2-Anthryl-2-anthracence Showing White Emission and High Charge Mobility," Angew. Chem., Int. Ed., 2017, 56, 722–727.
29. H. Usta, C. Kim, Z. Wang, S. Lu, H. Huang, A. Facchetti and T. J. Marks, "Anthracenedicarboximide-based semiconductors for air-stable, n-channel organic thin-film transistors: Materials design, synthesis, and structural characterization," J. Mater. Chem., 2012, 22, 4459–4472.
30. J., Liu, H., Dong, Z., Wang, D., Ji, C., H., Cheng, H., Geng. H., Zhang. Y., Zhen. L., Jiang, H., Fu. "Thin Film Field-Effect Transistors of 2,6-Diphenyl Anthracene (DPA)," Chem. Commun. 2015, 51 (59), 11777–11779.
31. H. J., Kim. H. H., Lee. J. W., Kim, J., Jang, J. J. Kim. "Surface dependent thermal evolution of the nanostructures in ultra-thin copper(ii) phthalocyanine films," J. Mater. Chem. 2012, 22 (18), 8881–8886.
32. M. R., Kiran. H., Ulla. M. N., Satyanaraya, G., Umesh. "Effect of deposition rate on the charge transport in Vanadyl-phthalocyanine thin films," Synth. Met. 2017, 224, 63–71.
33. H., Wang, F., Zhu, J., Yang. Y., Geng. D., Yan. "Weak Epitaxy Growth Affording High-Mobility Thin Films of Disk-Like Organic Semiconductors," Adv. Mater. 2007, 19 (16), 2168–2171.
34. H., Klauk. "Organic thin-film transistors," Chem. Soc. Rev. 2010, 39, 2643–2666.

35. S. A., DiBenedetto, A., Facchetti, M. A., Ratner, and T. J. Marks. “Molecular self-assembled monolayers and multilayers for organic and unconventional inorganic thin-film transistor applications,” Adv. Mater. 2009, 21 (14-15), 1407–1433.
36. A., Hussain, Y., Chianiago, A., Riaz, and M., Lee. “Process Design Alternatives for Producing Ultra-high-purity Electronic-Grade Propylene Glycol Monomethyl Ether Acetate,” Ind. Eng. Chem. Res. 2019, 5, 86 2246-2257.
37. S., Yadav, P., Kumar, and S., Ghosh. “Optimization of surface morphology to reduce the effect of grain boundaries and contact resistance in small molecule based thin film transistors,” Appl. Phys. Lett. 2012, 101 (19), 193304–193307.
38. H. J., Kim, H. H. Lee, J. W., Kim, J., Jang, and J. J., Kim. “Surface dependent thermal evolution of the nanostructures in ultra-thin copper(ii) phthalocyanine films,” J. Mater. Chem. 2012, 22 (18), 8881–8886.
39. D.B., Hall, P., Underhill, and J. M. Torkelson. “Spin coating of thin and ultrathin polymer films,” Polym. Eng. Sci. 1998, 38 (12), 2039–2045.

2.0 Developing 9,10-anthracene Derivatives: Optical, Electrochemical, Thermal and Electrical Characterization

2.1 Contributions of Authors

This section describes the context in which the research was performed, relating it to the development of the lab and my own research goals at the time. It describes the contributions of each author and the significance of the research.

Supplementary Materials: The following are available online at https://www.mdpi.com/1996-1944/12/17/2726, crystallography and UV-Vis absorption spectroscopy.

Author Contributions: Conceptualization was performed by B.H.L. and J.L.B. Methodology by, M.Y.V., N. J. Y., O.A.M.; validation, M.Y.V., N. J. Y., O.A.M., A.J.D., K.T.A., J.S.O.; formal analysis, M.Y.V., N. J. Y., J.S.O.; investigation, M.Y.V., N. J. Y., O.A.M., A.J.D., K.T.A., J.S.O.; data curation, M.Y.V., N. J. Y.,; writing—original draft preparation, M.V.; writing—review and editing, N.J.Y., J.L.B., B.H.L.; supervision, J.L.B., and B.H.L.; project administration, J.L.B., and B.H.L.; funding acquisition, J.L.B., and B.H.L.

The rest of this section has been adapted from Materials by MDPI: Vorona, M. Y.; Yutronkie, N. J.; Melville, O.; Daszczynski, A. J.; Agyei, K. T.; Brusso, J. L.; Lessard, B. H., "Developing 9,10-anthracene Derivatives: Optical, Electrochemical, Thermal, and Electrical Characterization," Materials, vol. 12, no. 17, pp. 1–16, 2019. https://doi.org/10.3390/ma12172726

2.2 Abstract

Anthracene-based semiconductors are a class of molecules that have attracted interest due to their air stability, planarity, potential for strong intermolecular interactions and favourable frontier molecular orbital energy levels. In this study seven novel 9,10-anthracene-based molecules were synthesized and their optical, electrochemical and thermal properties were characterized along with their single crystal arrangement. We found that functionalization of the 9,10-positions with different phenyl derivatives resulted in negligible variation in the optical properties with minor (±0.10 eV) changes in electrochemical behaviour, while the choice of phenyl derivative greatly affected the thermal stability (T_d >258 °C). Preliminary organic thin film transistors (OTFTs) were

fabricated and characterized using the 9,10-anthracene-based molecules as the semiconductor layer. These findings suggest that functionalization of the 9,10-position of anthracene leads to an effective handle for tuning of the thermal stability while having little to no effect on the optical properties and the solid-state arrangement.

2.3 Introduction

Organic electronic materials, namely organic light emitting diodes (OLEDs) have attracted considerable attention in academia and industry as a substitute for silicon-based devices such as liquid crystal displays and inorganic LEDs [1, 2]. One advantage of OLEDs, as well as other organic electronic devices such as organic photovoltaics and organic thin film transistors (OTFTs) versus traditional technologies, include their ability to be fabricated through solution processing techniques, including spin-coating [3], drop casting [4, 5], and ink-jet printing [6]. OTFTs have found to be an integral component of next generation applications such as pixel modulators in active matrix OLED displays [7], radiofrequency tags [8], and even biosensors [9].

The organic semiconducting (OSC) layer is the primary focus of research in OTFT technology, as it governs the operation of the device. A wide variety of materials have been proposed and investigated over the years [10]. Anthracene, being the first organic compound used to study organic semiconductor conductivity in the 1950s-1960s, is still a promising molecule [11-13]. Researchers developed OTFTs that employed anthracene-based molecules with mobilities as high as 0.02 $cm^2\ V^{-1}s^{-1}$ (p-type) by 2003 [14-16]. Since 2013, over 150 derivatives have been synthesized, providing the basis for developing various structure-property-mobility relationships [10, 17]. 2,6-Diphenyl anthracene (2,6-DPA) has afforded the highest p-type mobilities yet, with 14.8 $cm^2\ V^{-1}s^{-1}$ in OTFTs and 34.0 $cm^2\ V^{-1}s^{-1}$ in organic single-crystal transistors [18, 19]. According to the variety of anthracene-derivatives implemented in devices, charge mobility may be traced from mainly three key factors: (1) the relative energy levels – the alignment of the semiconductor highest occupied molecular orbital (HOMO) and or lowest unoccupied molecular orbital (LUMO) energy levels with the Fermi level of the source or drain electrodes defines the injection barriers; (2) the supramolecular arrangement of molecules in the solid-state – packing in either the herringbone or lamellar fashion, along with intermolecular distances, plays a significant role in charge transport ability; and (3) the thin-film morphology – ordered stacking and dense

grains with few boundaries and traps can reduce the obstruction for charge transport [10, 20, 21]. By examining the crystalline packing of anthracene-based derivatives via X-ray diffraction (XRD), we can gain an understanding of the intermolecular distances between conjugated centres of molecules arranged in a single-crystal. In general, the shorter the distance between π-orbital centres of molecules, the greater the charge mobility of an OSC will be in a device. For instance, relatively short intermolecular distances of 2.84–2.86 Å indicates strong π-π interactions, which likely contribute to the high charge mobility observed in devices containing 2,6-DPA [18-19]. Therefore, such an analysis gives us some insight into how such anthracene-derivatives will arrange themselves in thin-film. This facilitates the prediction of charge mobilities in an OSC device. Modifying the anthracene structure through coupling reactions can extend the π-electron system and tune the molecular packing, while simultaneously modifying the frontier molecular orbital energy levels or the thermal stability of the derivative; factors that are all crucial to the proper function of materials in devices [22, 23].

Over the years, considerable effort has been devoted to synthesizing 2,6- and 2,6,9,10-substituted anthracene derivatives as they have seemingly afforded the highest mobilities; however, relatively few 9,10-functionalized derivatives have been reported.[10] Anthracene derivatives substituted at the 9,10-position challenge the regular herringbone stacking observed in 2,6-functionalized derivatives and tend to form a more overlapped lamellar structure. This is an advantageous propensity for charge transport and an even better performance should be expected if closer molecular distance can be realized by more abundant and intensive intermolecular effects. In this study, we report several novel 9,10-substituted anthracene-based molecules, whereby we characterize their optical, electrochemical and thermal properties to build a structure-property-mobility relationship for anthracene-based semiconductors. We also analyzed the materials by single-crystal XRD and incorporated the materials in OTFTs, facilitating the comparison between solid-state arrangement and charge mobility.

2.3 Results and Discussion

2.3.1 Synthesis of 9,10-Disubstiuted Anthracenes

A series of 9,10-disubstituted anthracenes (1a-c, 2a-d) were synthesized utilizing a palladium-catalyzed Suzuki-Miyura cross-coupling reaction starting from commercially available reagents

as shown in Scheme 1. The general procedure for the aforementioned cross-coupling reactions employs tetrakis(triphenylphosphine)palladium(0) ($Pd(PPh_3)_4$) as the catalyst [24, 25], coupling substituted bromoanthracenes with varying boronic acids in a degassed solvent mixture of toluene, ethanol and water. The completion of coupling was determined through thin layer chromatography; conversion was achieved with heating of the mixtures overnight. The crude product was isolated by removal of the solvent and passing a dichloromethane (DCM) solution through a silica plug, separating the catalyst remnants. Sublimation of the crude materials provided a crystalline film of each desired product of high electronic purity. In some instances, recrystallization of the crude product in isopropanol produced a cleaner material for sublimation resulting in reduced yields. For analogue 2d, a N,N-dimethylformamide (DMF)/water solvent system had been chosen to circumvent the solubility issues of the reagents.

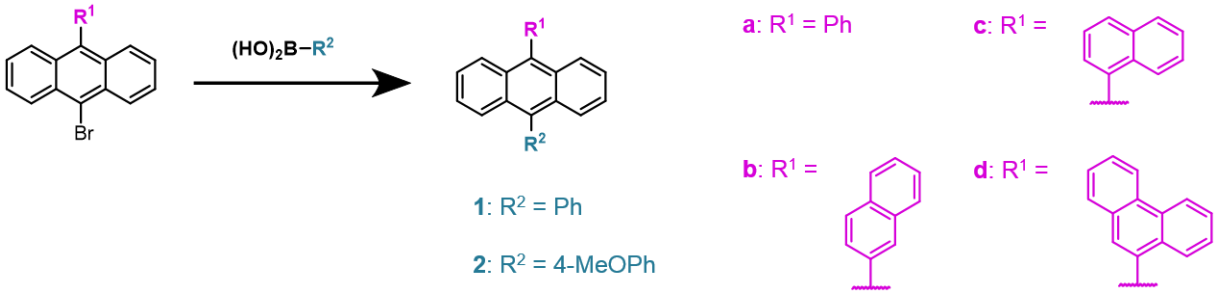

Scheme 1. Synthesis of 9,10-disubstituted anthracenes (1a-c, 2a-d) via Suzuki-Miyura cross-coupling reactions.

2.3.2 Optical and Electrochemical Properties

Solutions of compounds 1a-c and 2a-d in DCM were characterized by UV-visible (UV-Vis) and photoluminescence (PL) spectroscopy; their corresponding maximum peak absorbance ($\lambda_{\max}^{\text{abs}}$), energy gap ($E_{\text{gap}}$) and photoluminescence maximum peak emissions ($\lambda_{\max}^{\text{em}}$) are all tabulated in Table 1 and their respective spectra can be found in the ESI (Figures S6–S12). The absorption profiles of each compound are similar to previously reported 9,10-disubstituted anthracenes, exhibiting four vibronic bands found between 325–425 nm corresponding to π-π* ($S_0 \rightarrow S_1$) transitions of the anthracene core [26-30]. The minimal discrepancies between each of the $\lambda_{\max}^{\text{abs}}$ suggests minimal orbital contribution from the exterior aryl groups, despite the alignment of the optical transition dipole moment along the short axis of these molecules. These observations can be rationalized through the twisted arrangement of the aryl groups in respect to the anthracene

moiety [10, 14, 19, 20, 31-35]. With nearly identical absorption features, E_{gap} were between 2.96–2.99 eV for each derivative.

Table 1. Electrochemical and optical characterization of compounds 1a-c and 2a-d.

	$E_{1/2}$ (V)[a]	E_{HOMO} (eV)[b]	$\lambda_{\mathrm{max}}^{\mathrm{abs}}$ (nm)	E_{gap} (eV)[c]	$\lambda_{\mathrm{max}}^{\mathrm{em}}$ (nm)	Stokes Shift (nm)
1a	1.241	-5.68	342, 358, 376, 397	2.98	420, 435	23
1b	1.323	-5.73	341, 357, 376, 396	2.98	414, 430	18
1c	1.377	-5.73	341, 357, 376, 396	2.99	420, 435	24
2a	1.303	-5.69	339, 358, 376, 396	2.96	421, 431	25
2b	1.215	-5.59	343, 359, 377, 398	2.96	405, 430	7
2c	1.279	-5.68	343, 358, 377, 398	2.97	428	30
2d	1.237	-5.61	342, 358, 377, 397	2.97	427	30

[a]Volts versus SCE.
[b] $E_{\mathrm{HOMO}} = -4.80\ eV - (E_{\mathrm{onset}}^{\mathrm{ox}}\ vs.\ \mathrm{Fc/Fc^{+}})$
[c]E_{gap} was calculated from the onset of the lowest energy absorbance peak.

Excitation of the compounds with the lowest energy $\lambda_{\mathrm{max}}^{\mathrm{abs}}$ produced emission spectra lacking mirror image quality with a blending of the fine structure. Stokes shifts varied between derivatives, where the largest shifts were 30 nm for both 2c and 2d and the smallest shift was attributed to 2b of 7 nm. Solutions of each derivative were also excited with the next two higher energy $\lambda_{\mathrm{max}}^{\mathrm{abs}}$ and nearly identical emission profiles are observed, indicating similar relaxation pathways.

In addition to studying the photophysical properties, cyclic voltammetry (CV) was performed on solutions of 1a-c and 2a-d in DCM (0.1 M *n*-Bu_4NPF_6 supporting electrolyte) to investigate their electrochemical behaviour, as seen in Figure 1. A quasi-reversible oxidation process is observed for all derivatives with similar halfway oxidation potentials ($E_{1/2}$). The HOMO energy levels (E_{HOMO}) were estimated using the onset of the oxidation potentials [32, 36-40]. The calculated

E_{HOMO} values were all around -5.59 eV and -5.73 eV, which is more negative than other derivatives reported [10, 32, 41].

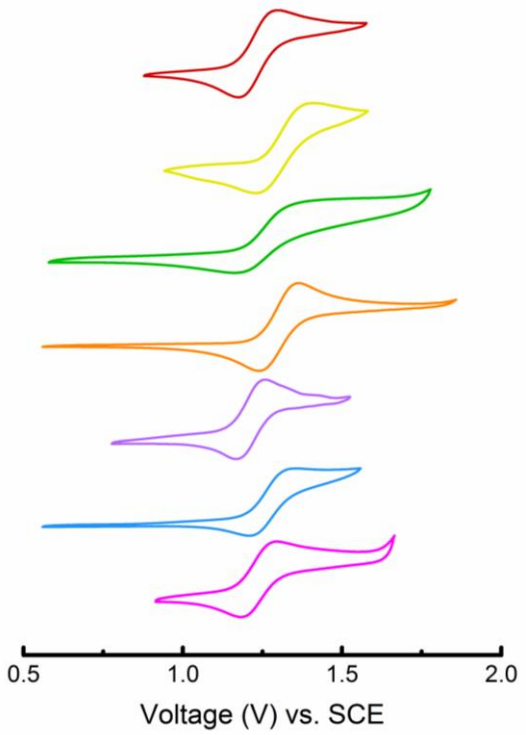

Figure 1. CV scans of 1a (red), 1b (yellow), 1c (green), 2a (orange), 2b (purple), 2c (blue) and 2d (magenta) in DCM.

The fact that all the CV data was similar indicates that the E_{HOMO} levels relative to the work function of the metal electrodes are similar as well, and therefore charge injection behaviour should be similar throughout the materials. This E_{HOMO} level, in combination with the E_{gap}, obtained from UV-Vis spectroscopy, would also suggest that all materials have similar stability to oxidation.

2.2.3 Thermogravimetric Analysis

In addition to frontier molecular orbital energy levels, the thermal stability of a material is of considerable importance when attempting to develop a successful device. High temperatures associated with phase transitions (i.e. fusion) and decomposition pathways of these materials are ideal as to avoid structural changes and morphological arrangements of the thin films. Therefore, the melting points (T_m) and decomposition temperatures (T_d) have been measured for compounds 1a–c and 2a–d and are tabulated in Figure 2. Unlike the optical properties, the choice in substituent

played a significant role in the thermal properties. Thermogravimetric analysis (TGA) was performed on all compounds, where the decomposition temperature (T_d) is determined at 5% weight loss. TGA was performed at a ramp heating rate of 5.0 ^{O}C min under a nitrogenous atmosphere. In general, molecules of 1 (258–302 °C) possessed lower T_d in comparison to their methoxy counterparts (275–386 °C), as the size of the peripheral aryl substituents has shown to influence this property.[42] This trend is also recognized as the R^1 group increases within each series, where 2d is superior with the highest T_d of 386 °. In regards to T_m, a similar pattern is apparent with 2, whereas the reverse is true for 1. These results may be a reflection of solid-state packing with stronger and/or more intermolecular interactions.

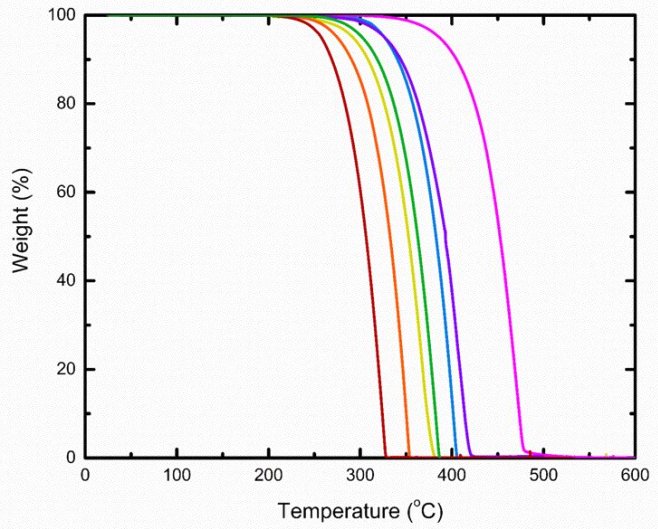

	T_m (°C)	T_d (°C)
1a	247–252	258
1b	232–235	292
1c	232–238	302
2a	228–232	275
2b	250–256	326
2c	257–261	326
2d	298–302	386

Figure 2. Thermogravimetric analysis curves (left) of 1a (red), 1b (yellow), 1c (green), 2a (orange), 2b (purple), 2c (blue) and 2d (magenta) and their associated T_m and T_d (corresponding to 5% weight loss).

2.3.4 Single Crystal X-Ray Diffraction

To elucidate the structure-property relationship of the 9,10-disubstituted anthracenes, the molecular and solid-state structures have been analyzed through X-ray crystallography. Single crystals were grown by train sublimation for each derivative and the crystallographic data is presented in Table S1, as found in the ESI of this study. Between molecular entities, a number of commonalities are present with respect to their crystallographic features. For example, slight distortions are adopted along the backbone of the anthracene cores that disrupts its planarity. The degree of distortion has been characterized by the dihedral angle (ω) created by intersecting planes

bearing the terminal carbon atoms of the peripheral rings (Figure 3; i.e. C^1–C^4 and C^5–C^8), as well as based on the distance between the individual carbon atoms and the mean plane of the anthracene moiety (Table S2). The largest distortion is observed in 1b, which has two unique molecules in the asymmetric unit, with a dihedral angle of 5.1° and twelve out of the fourteen carbon atoms deviating from the mean plane by at least 0.03 Å for one of the molecules in the asymmetric unit. Interestingly, the other molecule experiences this distortion to a lesser extent with a dihedral angle of 3.1°, and half the number of carbon atoms deviating from the mean plane. Based on the family of compounds described here, it is apparent this distortion minimizes with the attachment of larger aryl groups and as such, may be resulting from a response to the packing arrangement of the molecules in the solid-state. Deviations in torsion angles (τ) between the pendent aryl substituents and the anthracene cores deviate from co-planarity with angles ranging from 67.3–89.43°, which can be attributed to steric interactions between the *peri*-hydrogen atoms of the anthracene core and the *ortho*-hydrogen atoms of the aryl substituents [32]. As a result, the twisting of the aryl substituents provides the foundation for self-assembly of the molecules in packing arrangements dominated by C–H···π interactions with anthracene units and aryl groups.

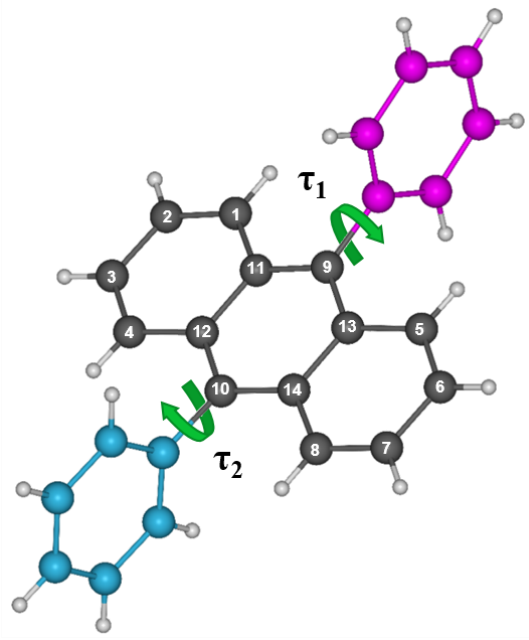

	ω (°)	τ_1 (°)	τ_2 (°)
1a	3.6	89.2	89.2
1b	5.1 3.1	75.3 81.5	67.3 81.7
1c	2.0	75.2	71.8
2a	3.5	72.1	81.3
2b	3.1	85.6	86.1
2c	1.4	74.3	80.2
2d	1.8	89.0	74.6

Figure 3. Molecular distortions depicted by the dihedral angle (ω) between intersecting planes from the outer blades of the anthracene backbone (C1–C4 and C5–C8) and the mean torsion angles (τ) between pendant aryl groups and anthracene unit. Compound 1b contains two unique molecules in the asymmetric unit.

Understanding the molecular properties of these compounds can give us insights towards the supramolecular arrangements and the interactions between molecules. In regards to 1a, the near orthogonal phenyl substituents guide molecules in two-dimensional arrays parallel to the (010) plane arranging in a lamellar-like structure (Figure 4). Where one phenyl moiety facilitates the C–H···π interactions (2.72–2.89 Å) with anthracene cores along the arrays, the other joins adjacent arrays through weaker C–H···π interactions (2.84 Å).

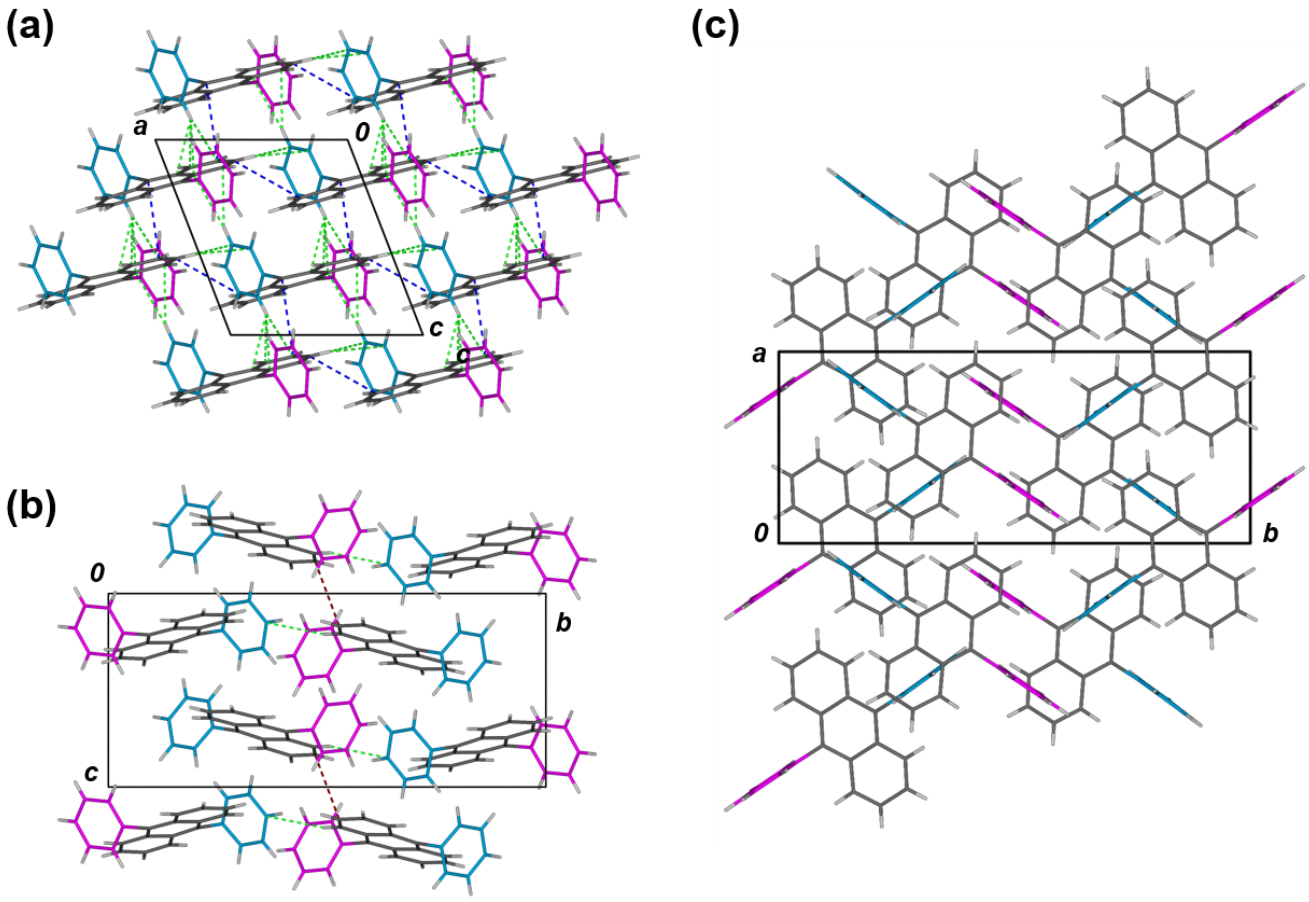

Figure 4. Two dimensional array of 1a parallel to the (010) plane (a) and its intercalating adjacent array viewed down *a*-direction (b) and *c*-direction (c). C–H···π interactions between pendent substituents (R^1 = magenta; R^2 = blue) and anthracene cores are shown in green, while π-π contacts between anthracene units are shown in blue (within array) and red (between arrays).

A consequence resulting from the aforementioned interactions is the lack of superposition between anthracene units locked in a zig-zag pattern, significantly reducing π-orbital overlap between

neighbouring molecules. Consequently, the closest π-contacts are 3.79 and 3.92 Å within the arrays and 3.67 Å between arrays.

Replacement of the R^1 phenyl substituent with a naphthalene moiety induces greater π-overlap amongst the anthracene cores, as shown in polycyclic hydrocarbons 1b and 1c. Compound 1b crystallizes with two unique molecules in the asymmetric unit, where spirals of alternating molecules run parallel to the *b*-axis connected by C–H···π interactions (2.80–2.84 Å) as seen in Figure 5.

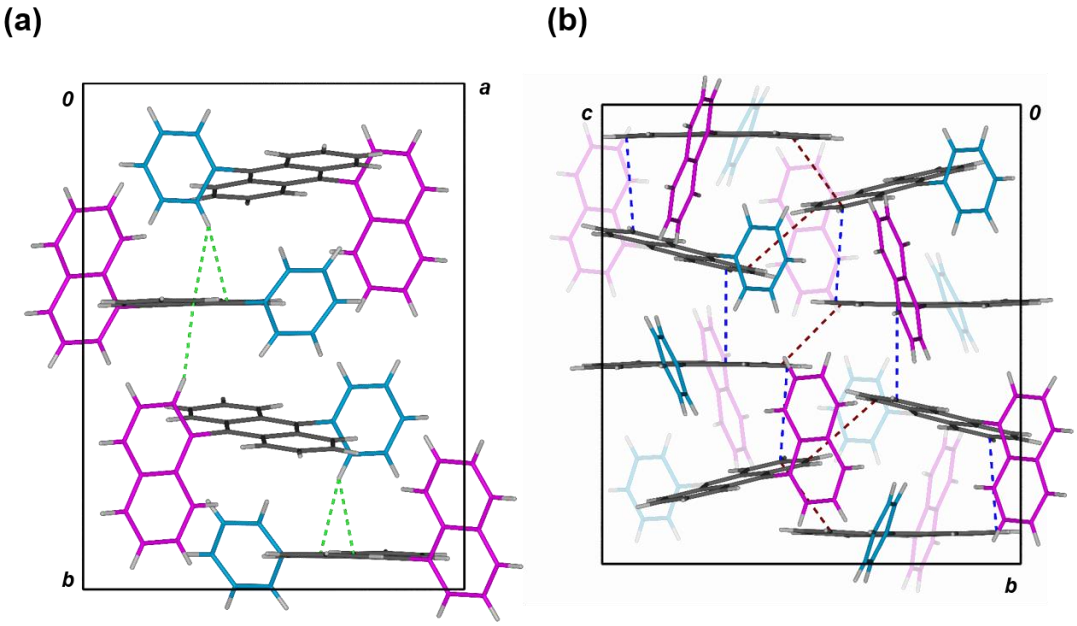

Figure 5. (a) Spiral of 1b along the *b*-direction. (b) Unit cell containing two interlocking spirals. C–H···π interactions between pendent substituents (R^1 = magenta; R^2 = blue) and anthracene cores are shown in green, while π-π contacts between anthracene units are shown in blue (within spiral) and red (between spirals).

While the mean plane of the anthracene backbone belonging to one of the unique molecules is relatively planar to the (010) plane (i.e. perpendicular to the stacking axis; 88.6°), the other core deviates from the axis at an angle of 77.0° rendering alternating π-π distances of 3.71 and 3.74 Å. This structural feature, in addition to the molecular distortions described earlier, could be a response to minimize the steric interactions arising from the protruding naphthyl substituents alongside of the spiral. More interesting is the interlocking of adjacent spirals through additional C–H···π interactions (2.89 Å) along the *c*-direction providing shorter C–C contacts (3.46–3.60 Å) between neighbouring anthracene units in two dimensions.

In contrast to 1b, molecules of 1c form slipped π-stacks parallel to the *b*-axis with the shortest π-contact of 3.72 Å between anthracene units (Figure 6).

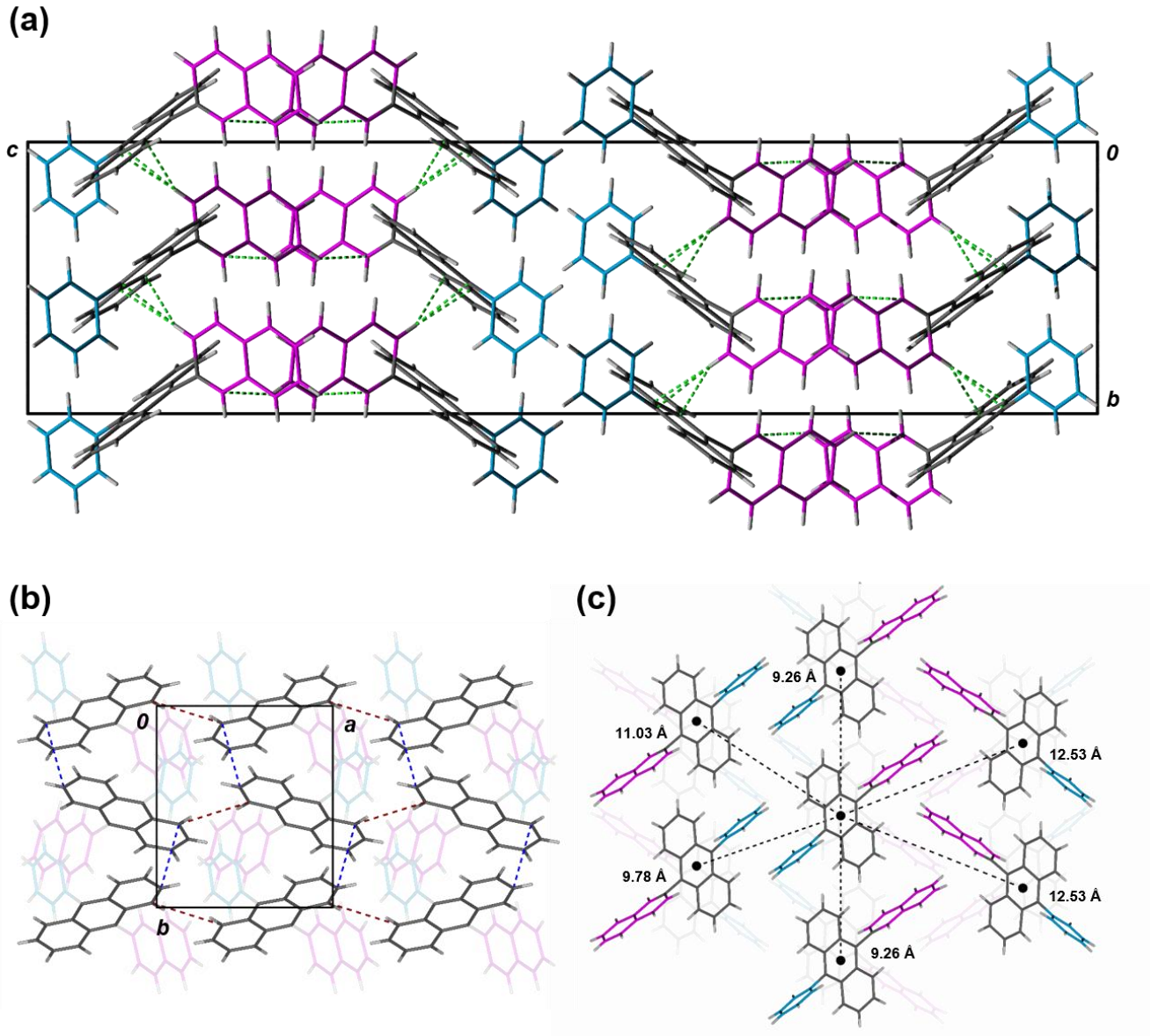

Figure 6. Slipped π-stacks of 1c viewed along the *a*-direction (a) and *c*-direction (b). C–H···π interactions between pendent substituents (R^1 = magenta; R^2 = blue) and anthracene cores are shown in green, while π-π contacts between anthracene units are shown in blue (intrastack) and red (interstack). (c) Distances between the centroids of neighbouring molecules are illustrated between adjacent π-stacks along the *c*-direction.

The attachment of the naphthyl group at the 2 position hinders superposition of the anthracene π-systems, similar to 1a, as C–H···π interactions (2.71–2.89 Å) lock anthracene domains in a criss-cross configuration. In addition, the naphthyl groups also facilitate C–H···π interactions (2.87 Å) that segregate π-stacks in staggered rows across the *b*-direction. Although interstack interactions are suppressed across this direction, adjacent stacks along the *a*-direction are closer together providing additional but weaker π–π interactions (3.88 Å) between stacks.

Inclusion of a methoxy group as the R^2 substituent reinforces the π-stacking found in 2a, 2c and 2d (Figures 7, 8, 9).

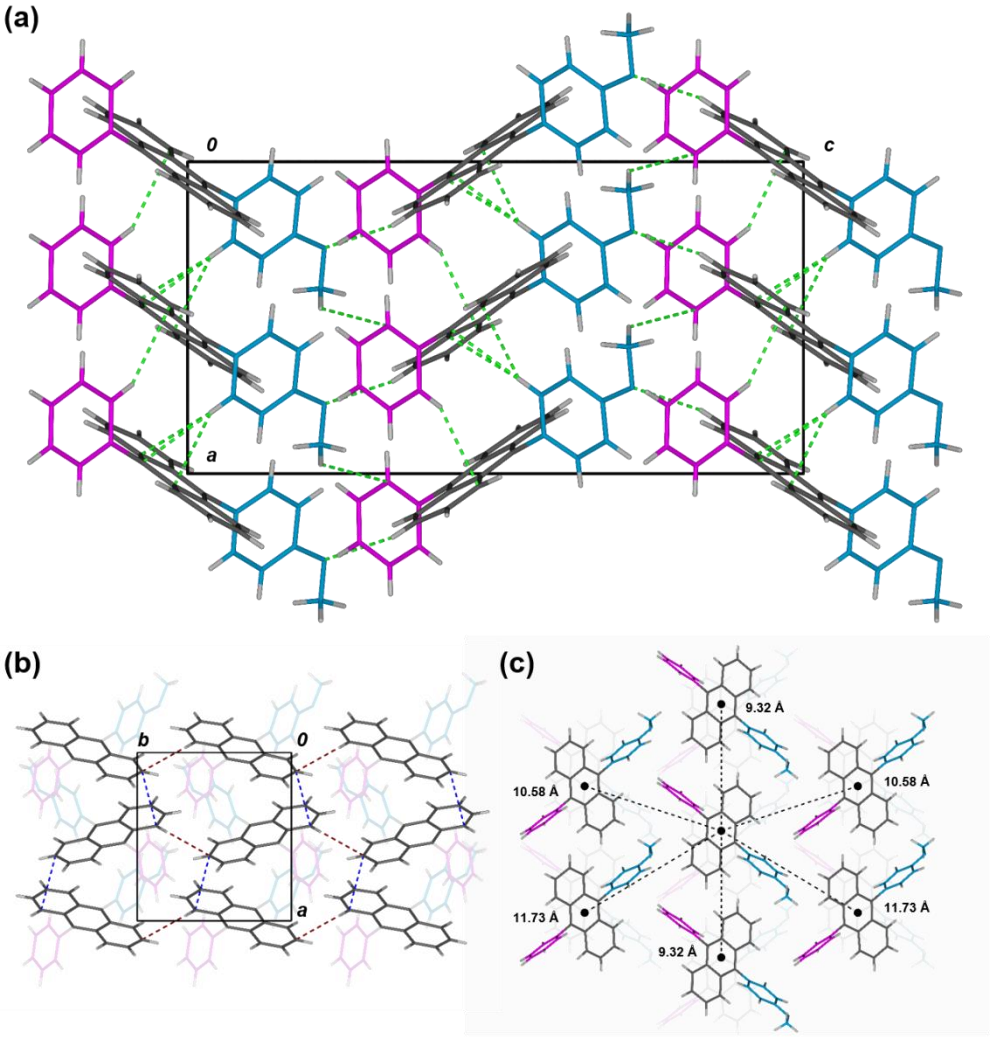

Figure 7. Slipped π-stacks of 2a viewed along the c-direction (a) and b-direction (b). C–H···π interactions between pendent substituents (R^1 = magenta; R^2 = blue) and anthracene cores are shown in green, while π-π contacts between anthracene units are shown in blue (intrastack) and

red (interstack). (c) Distances between the centroids of neighbouring molecules are illustrated between adjacent π-stacks down the c-direction.

Self-assembly of these derivatives are similar to 1c, such that staggered rows of stacked anthracene cores in a criss-cross arrangement, suggesting the size of the group influences this type of packing. As a result, the shortest π-contact within these stacks measures to 3.63, 3.71 and 3.54 Å for 2a, 2c and 2d, respectively.

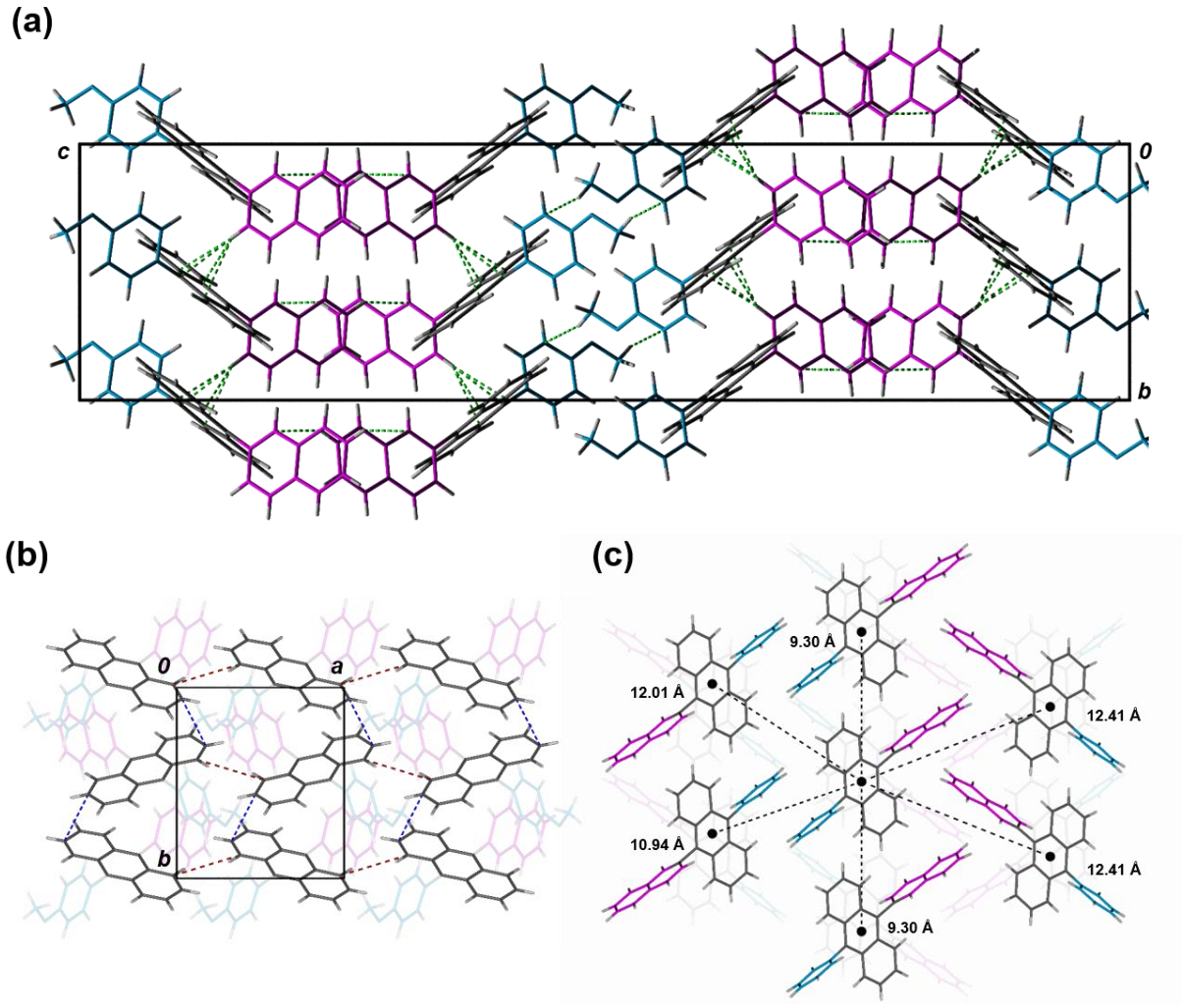

Figure 8. Slipped π-stacks of 2c viewed along the *c*-direction (a) and *a*-direction (b). C–H···π interactions between pendent substituents (R^1 = magenta; R^2 = blue) and anthracene cores are shown in green, while π-π contacts between anthracene units are shown in blue (intrastack) and red (interstack). (c) Distances between the centroids of neighbouring molecules are illustrated between adjacent π-stacks along the *b*-direction.

Interestingly, the addition of the various molecular substitutions did not have a large influence on the distance between the stacks of each row, thus retaining the weaker interstack π–π interactions of 3.90, 3.91 and 3.97 Å for 2a, 2c and 2d, respectively. The same cannot be said for 2b, as hydrogen bonds in addition to C–H···π interactions lock in co-planarity between anthracene frameworks parallel to the (100) plane ultimately disrupting the spiral motifs observed in 1b. The molecules are spaced out along their stacking axes in pairs to mitigate the steric repulsion from the protruding naphthalene groups, where the shortest C-C contact between anthracene moieties is 4.82 Å.

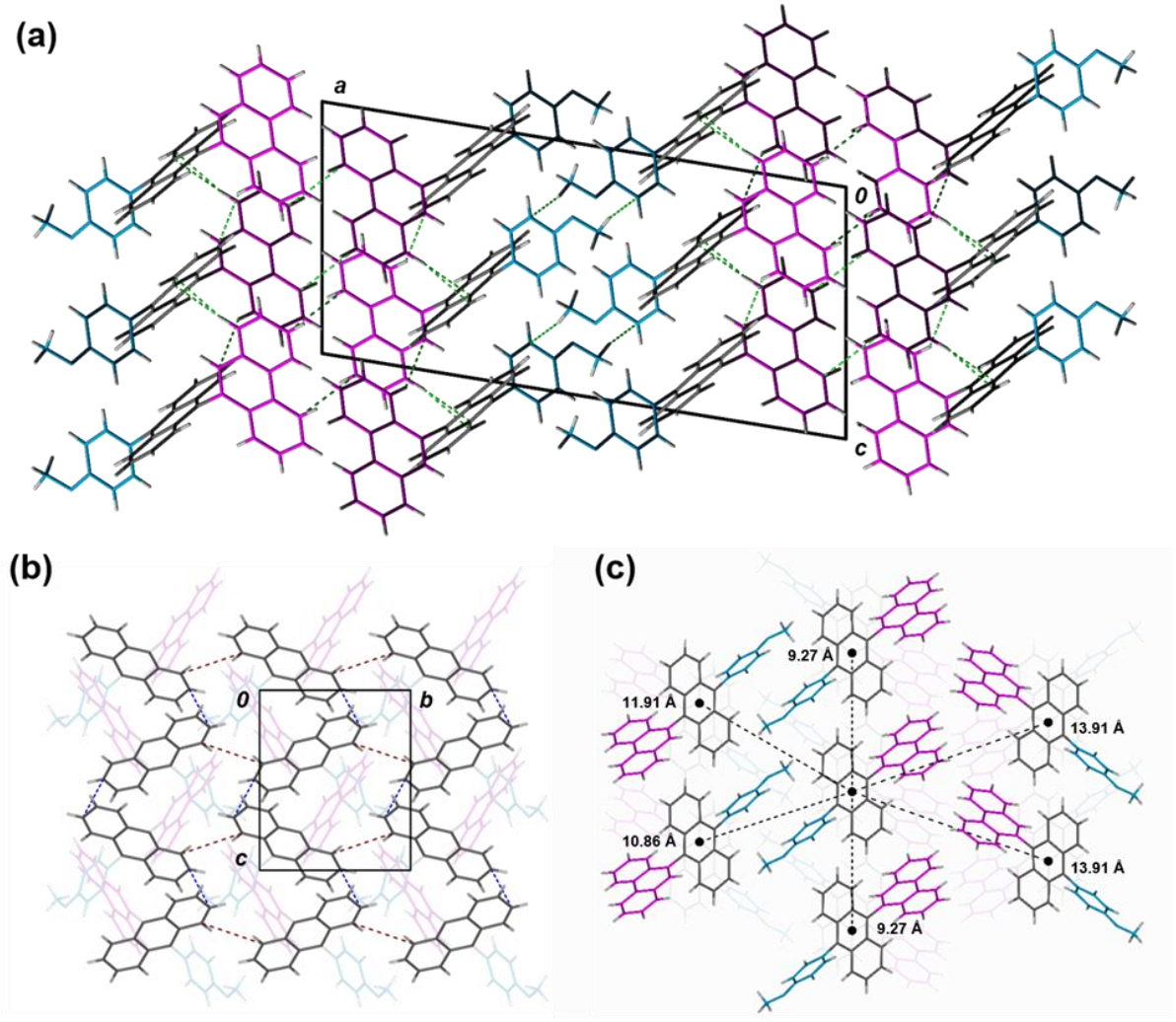

Figure 9. Slipped π-stacks of 2d viewed along the *a*-direction (a) and *b*-direction (b). C–H···π interactions between pendent substituents (R^1 = magenta; R^2 = blue) and anthracene cores are shown in green, while π-π contacts between anthracene units are shown in blue (intrastack) and red (interstack). (c) Distances between the centroids of neighbouring molecules are illustrated between nearest π-stacks along the *c*-direction.

Analysis of the crystals by Marcus Inversion Region (MIR) theory would be beneficial for determining the electronic coupling and to estimate the charge transfer rate between adjacent molecules. We did not attempt to do this because very little interaction can clearly be seen between the molecules in the single crystal data. Furthermore, to be able to address unconventional charge transport regime requires an active control over the driving force of the charge carriers, which could be facilitated by differences in their electronic energies [43-45]. The critical crossover point between the MIR and the normal region would exhibit a minimum in the activation energy for charge transport between neighbouring molecules [43-45]. We do not have access to the necessary software suite in order to run the required calculations to assess the transport regime of our molecules.

2.4.5 OTFT Performance

Compounds 1b and 2a–d were implemented into OTFTs by spin-coating the semiconductor onto Si/SiO_2 substrates with prefabricated gold source-drain electrodes with channel widths, *W*, of 2000 μm and channel length, L, of 2.50 μm (Figure 10a). OTFT characteristics of compounds can be found in Table 2. All OTFTs were test in air. Characteristic output and transfer curves of the integrated compounds are shown in Figure 5.

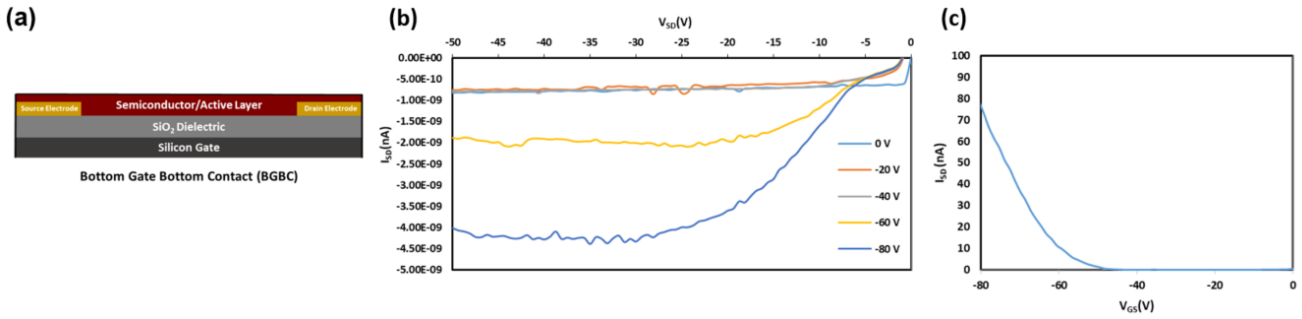

Figure 10. (a) Bottom gate bottom configuration used for OTFT integration of compounds 1b and 2a–d. (b) Characteristic output curve of fabricated OTFTs (1c) (c) Characteristic transfer curve of fabricated OTFTs (1c).

Compounds 1b and 2a,c-d exhibited field effect mobility, while compound 2b did not produce any field effect. On average hole mobilities (μ_{avg}) for compounds 1b and 2a,c-d were on the order of $\approx 3.2 \times 10^{-6}$ cm^2 V^{-1} s^{-1} with an average threshold voltage (V_T) from -13 V to -43 V, and $I_{on/off}$ ranging between 10^1-10^2. As expected, the OTFT performance is modest in comparison to previously reported examples, likely due to the relatively large π-π intermolecular distances as described

above. All channels lengths were tested (2.5, 5.0, 10.0, 20.0 μm). Only channel 2.5 μm length devices had observed field-effects. Annealing at 120 °C for 40 minutes was attempted to improve the performance, but had resulted in poorer mobilties; agglomeration of the thin-film was visible by microscopy. Typical film thickness of these BGTC devices ranged from 157 nm to 1173 nm, significantly larger than the height of the Au electrodes (40 nm) relative to the SiO_2 dielectric. These performance metrics are similar to other derivatives with comparable intermolecular packing distances, such as Silvestri et al.'s PA-P6d [41]. Wurthner et al.'s anthracene derivative also showed no field affect, whereby the π-π overlap of the face-to-face interactions of their molecule was approximately 50% and at a distance of 3.39 Å [46]. These results suggest that while 9,10-substitutions can act as handles to tune significantly tune the thermal stability they also impart significant modifications to the solid-state arrangement, which can have detrimental effects on the OTFT performance. Compounds 1a and 1c were not incorporated into devices based on the poor expected device performance which would likely result from the large π-π distances obtained from single crystal diffraction (similar to device obtained using 2a and 2c).

Table 2. P-type OTFT testing summary[a] of compounds 1a–c and 2a–d.

	π-π Distance (Å)[b]	$I_{on/off}$	μ_{avg} ($cm^2\ V^{-1}\ s^{-1}$)	μ_{max} ($cm^2\ V^{-1}\ s^{-1}$)	$V_{T,Avg}$ (V)	$V_{T,max}$ (V)
1a	3.67, 3.79, 3.92	-	-	-	-	-
1b	3.46, 3.58, 3.60, 3.71, 3.74	10^2	5.31×10^{-6}	7.26×10^{-6}	-37	-21
1c	3.72, 3.88	-	-	-	-	-
2a	3.63, 3.90	10^2	8.08×10^{-7}	4.44×10^{-6}	-41	-14
2b[c]	4.82	–	–	–	–	–
2c	3.71, 3.91	10^1	1.48×10^{-7}	1.91×10^{-6}	-29	-13
2d	3.54, 3.97	10^2	6.68×10^{-6}	7.07×10^{-6}	-43	-34

[a]Field-effect observed at gate voltages varied from -80 V to -40V; Channel length of 2.5 μm and electrode width of 2000 μm, where $I_{on/off}$ order of magnitude of on/off current ratios, μ_{avg} = average hole mobility, μ_{max} = max hole mobility, $V_{T,Avg}$ = average threshold voltage and $V_{T,max}$ = average threshold voltage

[b]Closest π-π contacts between neighbouring molecules determined through single crystal X-ray diffraction.

[c]OTFTs based on compound 2b exhibited no significant field effect.

2.4. Conclusions

Seven novel 9,10-functionalized anthracene-based molecules were synthesized, their optical, photoluminescent, electrochemical and thermal characteristics were probed and they were implemented as the active semiconducting layer in OTFTs. Based on this study, substitution of the 9,10-position proved to be an effective way to tune the thermal stability of the material while having negligible effects on the frontier molecular orbital energy levels. Additionally, functionalization at the 9,10-position was found to strongly affect the solid-state arrangement, as determined through single crystal X-ray diffraction (XRD) analysis. These significant changes in solid-state structures resulted in OTFTs with modest performance where the highest mobility obtained was on an order of 10^{-6} cm^2 V^{-1} s^{-1} with a V_{GS} of -80 V. These findings suggest that moiety functionalization strongly affects physicochemical properties such as melting point and decomposition temperatures, yet has little effect on optical and electrochemical properties. These results further indicate that towards improving anthracene-based OTFTs it is wise to explore functionalization at various locations about the anthracene core rather than exclusively focusing on the 9,10-position. Future work will investigate the development of new molecules with such design strategies in mind to provide insight into their effect on solid-state engineering.

2.5 Materials and Methods

2.5.1 General Methods and Procedures

The reagents 9-bromo-10-phenylanthracene (Lumtec Corp., Taipei, Taiwan), 9-bromo-10-(naphthalene-1-yl)anthracene (Lumtec Corp., Taipei, Taiwan), 9-bromo-10-(phenanthrene-10-yl)anthracene (Lumtec Corp., Taipei, Taiwan), 9-bromo-10-(naphthalen-2-yl)anthracene (Lumtec Corp., Taipei, Taiwan), phenylboronic acid (Oakwood Products Inc., Estill, South Carolina, USA), 4-methoxybenzeneboronic acid (Oakwood Products Inc., Estill, South Carolina, USA), potassium carbonate (K_2CO_3) (Oakwood Products Inc., Estill, South Carolina, USA), tetrakis(triphenylphosphine)palladium(0) ($Pd(PPh_3)_4$) (Strem Chemicals, Newburyport, Massachusetts, USA), toluene, N,N-dimethylformamide (DMF) (Caledon Laboratories Ltd., Georgetown, Ontario, Canada) and ethanol were commercially obtained and used as received. All solvents were ACS grade. All reactions were performed under an atmosphere of dry nitrogen. Melting points were taken using a Mel-Temp apparatus and are uncorrected. NMR spectra were

run in $CDCl_3$ solutions at room temperature on a Bruker 400 MHz spectrometer (Billerica, MA, USA) and were referenced to the deuterated solvent peak. Film thickness measurements were performed with the Bruker DektakXT Profilometer (Billerica, MA, USA). IR spectra were recorded on an Agilent Technologies Cary 630 FT-IR spectrometer. UV-Vis spectra were measured with a Varian Cary Series 6000 UV-Vis-NIR spectrophotometer and photoluminescence spectra were obtained using a Varian Cary Eclipse fluorescence spectrophotometer. UV-Vis and fluorescence spectra were measured in HQGC-grade DCM solutions with 1 cm precision quartz cuvettes. TGA analyses were performed in 70 ul alumina crucible using a TGA/DSC 1 Mettler Tolledo instrument under nitrogen gas with a heating rate of 5.0 °C min^{-1}. Gas Chromatgraphy/Mass Sectrometry (GC/MS) was performed using Agilent 6890 GC coupled to Agilent 5975 MS. The inlet temperature was set 320ºC with a split ratio 50:1 at 1 uL injections. The initial oven temperature 275ºC, held for 15 min, then ramped to 300ºC (40ºC/min) and held for 25 min. The column was HP-5MS (30 m x 250 um x 0.25 um), and its initial flow was 1.6 mL min^{-1}. A toluene and 1,2-dichloroethane solvent mixture was used for all GC/MS experiments.

2.5.2 Preparation of 9,10-diphenylanthracene (1a)

A bubbled-degassed solution of toluene, ethanol and water (1:0.25:0.15, 347 mL) was transferred to a mixture of 9-bromo-10-phenylanthracene (1.51 g, 4.53 mmol), phenylboronic acid (1.11 g, 9.10 mmol), K_2CO_3 (1.88 g, 13.60 mmol) and $Pd(PPh_3)_4$ (0.79 g, 0.68 mmol). The reaction was stirred for 16 hours at 65°C. After the reaction was cooled to room temperature, the solvent was removed *in vacuo*. The resulting solid was dissolved in a minimal amount of DCM, washed with a 1.0 M aqueous NaOH solution and subsequently with water and brine. The organic phase was dried with $MgSO_4$, filtered through a silica plug and dried *in vacuo* resulting in an off-white crude product. The crude product was recrystallized in isopropanol (Yield 0.42 g, 1.27 mmol, 28%) and further purified through sublimation at a temperature range of 205–215°C under a pressure of 10^{-3} Torr with CO_2 as a carrier gas, which afforded 1a as white crystals. Yield 0.26 g (0.79 mmol, 17%). GC/MS reported an elution time of 6.760 min with abundance of $2.1x10^6$ and reported an M^+ peak of 330.2 m/z compared to a prediction of 330.14 m/z. MP: 247–252 °C. ^1H NMR (δ, 400 MHz, $CDCl_3$): 7.69–7.73 (4H, m), 7.54–7.64 (6H, m), 7.48–7.52 (4H, m), 7.32–7.36 (4H, m). ^{13}C NMR (δ, 100 MHz, $CDCl_3$): 139.24 (2C), 137.26 (2C), 131.47 (4CH), 130.02 (4C), 128.55 (4CH), 127.61 (2CH), 127.11 (4CH), 125.13 (4CH). FT-IR (ν_{max}): 3059 (w), 3032 (w), 1656 (w), 1598

(w), 1492 (w), 1439 (m), 1389 (m), 1369 (w), 1278 (w), 1193 (w), 1174 (w), 1158 (w), 1073 (m), 1025 (m), 999 (w), 942 (m), 923 (w), 856 (w), 845 (w), 767 (s), 748 (s), 732 (m), 700 (s), 661 (s) cm^{-1}.

2.5.3 Preparation of 9-phenyl-10-(1-naphthalenyl)-anthracene (1b)

Prepared analogously to 1a using 9-bromo-10-(naphthalene-1-yl)anthracene (1.50 g, 3.91 mmol), phenylboronic acid (0.95 g, 7.79 mmol), K_2CO_3 (1.62 g, 11.72 mmol) and $Pd(PPh_3)_4$ (0.68 g, 0.59 mmol) in 300 mL of the solvent mixture yielding an off-white crude solid. Sublimation at a temperature range of 205–215°C under a pressure of 10^{-3} Torr with CO_2 as a carrier gas afforded 1b as white crystals. Yield 0.41 g (1.08 mmol, 28%). GC/MS reported an elution time of 16.114 min with abundance of $2.1x10^7$ and reported an M^+ peak of 380.2 m/z compared to a prediction of 380.16 m/z. MP: 232–235 °C. ^{1}H NMR (δ, 400 MHz, $CDCl_3$): 8.01–8.09 (2H, m), 7.70–7.76 (3H, m), 7.44–7.67 (9H, m), 7.30–7.35 (2H, m), 7.17–7.26 (5H, m). ^{13}C NMR (δ, 100 MHz, $CDCl_3$): 139.23 (1C), 137.63 (1C), 136.96 (1C), 135.15 (1C), 133.86 (1C), 133.76 (1C), 131.54 (2CH), 130.79 (2C), 130.08 (2C), 129.37 (CH), 128.58 (CH), 128.57 (CH), 128.37 (CH), 128.25 (CH), 127.66 (CH), 127.20 (2CH), 127.20 (2CH), 126.83 (CH), 126.42 (CH), 126.15 (CH), 125.75 (CH), 125.31 (2CH), 125.21 (2CH). FT-IR (ν_{max}): 3047 (w), 2922 (w), 2853 (w), 1702 (w), 1655 (w), 1592 (w), 1561 (w), 1508 (w), 1438 (m), 1372 (m), 1255 (w), 1069 (w), 1028 (m), 1016 (w), 936 (m), 801 (m), 791 (w), 778 (s), 765 (s), 756 (s), 735 (m), 705 (s), 670 (m), 657 (s) cm^{-1}.

2.5.4 Preparation of 9-phenyl-10-(2-naphthalenyl)-anthracene (1c)

Prepared analogously to 1a using 9-bromo-10-(naphthalene-2-yl)anthracene (1.51 g, 3.94 mmol), phenylboronic acid (0.96 g, 7.88 mmol), K_2CO_3 (1.63 g, 11.80 mmol) and $Pd(PPh_3)_4$ (0.68 g, 0.59 mmol) in 287 mL of the solvent mixture yielding an off-white crude solid. The crude product was recrystallized in isopropanol (Yield 0.39 g, 1.01 mmol, 26%) and further purified through sublimation at a temperature range of 155–185°C under a pressure of 10^{-3} Torr with CO_2 as a carrier gas, which afforded 1c as white crystals. Yield 0.29 g (0.76 mmol, 19%). GC/MS reported an elution time of 19.523 min with abundance of $5.1x10^6$ and reported an M^+ peak of 380.2 m/z compared to a prediction of 380.16 m/z. MP: 232–238 °C. ^{1}H NMR (δ, 400 MHz, $CDCl_3$): 7.91–8.10 (4H, m), 7.71–7.76 (4H, m), 7.51–7.65 (8H, m), 7.29–7.35 (2H, m), 7.17–7.37 (4H, m). ^{13}C NMR (δ, 100 MHz, $CDCl_3$): 139.23 (1C), 137.42 (1C), 137.04 (1C), 136.76 (1C), 133.58 (1C),

132.92 (1C), 131.49 (2CH), 130.39 (1CH), 130.20 (2C), 130.06 (2C), 129.72 (1CH), 128.58 (2CH), 128.25 (1CH), 128.11 (1CH), 128.05 (1CH), 127.64 (1CH), 127.17 (2CH), 127.16 (2CH), 126.58 (1CH), 126.36 (1CH), 125.24 (2CH), 125.18 (2CH). FT-IR (ν_{max}): 3051 (w), 1702 (w), 1655 (w), 1599 (w), 1561 (w), 1498 (w), 1438 (m), 1394 (m), 1370 (w), 1271 (w), 1244 (w), 1202 (w), 1176 (w), 1135 (w), 1070 (w), 1028 (m), 1017 (w), 1002 (w), 970 (w), 955 (w), 936 (m), 917 (w), 898 (w), 878 (w), 857 (w), 849 (w), 820 (m), 794 (w), 772 (m), 759 (s), 748 (s), 703 (s), 676 (m), 658 (s) cm^{-1}.

2.5.5 Preparation of 9-(4-methoxyphenyl)-10-phenylanthracene (2a)

Prepared analogously to 1a using 9-bromo-10-phenylanthracene (1.39 g, 4.17 mmol), 4-methoxybenzeneboronic acid (1.26 g, 8.29 mmol), K_2CO_3 (1.73 g, 12.52 mmol) and $Pd(PPh_3)_4$ (0.72 g, 0.62 mmol) in 318 mL of the solvent mixture yielding an off-white crude solid. The crude product was recrystallized in isopropanol (Yield 0.76 g, 2.11 mmol, 51%) and further purified through sublimation at a temperature range of 150–180°C under a pressure of 10^{-3} Torr with CO_2 as a carrier gas, which afforded 2a as white crystals. Yield 0.45 g (1.25 mmol, 30%). GC/MS reported an elution time of 11.715 min with abundance of $3.0x10^6$ and also reported an M^+ peak of 360.2 m/z compared to a prediction of 360.15 m/z. MP: 228–232 °C. ^{1}H NMR (δ, 400 MHz, $CDCl_3$): 7.74–7.79 (2H, m), 7.68–7.73 (2H, m), 7.53–7.63 (3H, m), 7.47–7.50 (2H, m), 7.39–7.43 (2H, m), 7.31–7.37 (4H, m), 7.14–7.17 (2H, m), 3.97 (3H, s). ^{13}C NMR (δ, 100 MHz, $CDCl_3$): 159.18 (1C), 139.28 (1C), 137.08 (1C), 137.06 (1C), 132.53 (2CH), 131.48 (2CH), 131.25 (1C), 130.36 (2C), 130.06 (2C), 128.54 (2CH), 127.58 (CH), 127.19 (2CH), 127.10 (2CH), 125.10 (2CH), 125.05 (2CH), 114.02 (2CH), 55.54 ($1CH_3$). FT-IR (ν_{max}): 3067 (w), 3042 (w), 2999 (w), 2963 (w), 2936 (w), 2910 (w), 2841 (w), 1607 (m), 1575 (w), 1560 (w), 1513 (s), 1497 (m), 1463 (m), 1439 (m), 1409 (w), 1391 (m), 1370 (w), 1305 (w), 1284 (m), 1242 (s), 1190 (w), 1182 (m), 1176 (m), 1169 (m), 1158 (w), 1145 (w), 1136 (w), 1105 (m), 1071 (m), 1028 (s), 943 (m), 917 (w), 879 (w), 850 (m), 831 (s), 821 (m), 792 (m), 771 (s), 765 (s), 756 (s), 737 (m), 732 (m), 715 (m), 705 (s), 670 (s), 666 (s) cm^{-1}.

2.5.6 Preparation of 9-(4-(methoxyphenyl))-10-(1-naphthalenyl)anthracene (2b)

Prepared analogously to 1a using 9-bromo-10-(naphthalene-1-yl)anthracene (1.49 g, 3.89 mmol), 4-methoxybenzeneboronic acid (0.74 g, 4.86 mmol), K_2CO_3 (1.00 g, 7.29 mmol) and $Pd(PPh_3)_4$ (0.42 g, 0.36 mmol) in 191 mL of the solvent mixture yielding an off-white crude solid. Sublimation at a temperature range of 155–185°C under a pressure of 10^{-3} Torr with CO_2 as a carrier gas afforded 2b as white crystals. Yield 0.76 g (1.86 mmol, 48%). GC/MS reported an elution time of 51.288 min with abundance of $1.3x10^6$ and also reported a M^+ peak of 410.2 m/z compared to a prediction of 410.1 m/z. MP: 250–256°C. ^{1}H NMR (δ, 400 MHz, $CDCl_3$): 8.01–8.08 (2H, m), 7.79–7.81 (2H, m), 7.69–7.73 (1H, m), 7.57–7.59 (1H, m), 7.42–7.51 (5H, m), 7.31–7.35 (2H, m), 7.16–7.25 (6H, m), 3.99 (3H, s). ^{13}C NMR (δ, 100 MHz, $CDCl_3$): 159.23 (1C), 137.44 (1C), 137.01 (1C), 134.97 (1C), 133.86 (1C), 133.77 (1C), 132.60 (1CH), 132.59 (1CH), 131.24, 1 30.83 (2C), 130.43 (2C), 129.37 (1CH), 128.36 (1CH), 128.22 (1CH), 127.28 (2CH), 127.19 (2CH), 126.84 (1CH), 126.40 (1CH), 126.13 (1CH), 125.75 (1CH), 125.28 (2CH), 125.12 (2CH), 114.07 (1CH), 114.03 (1CH), 55.57 ($1CH_3$). FT-IR (ν_{max}): 3037 (w), 2958 (w), 2931 (w), 2837 (w), 1606 (m), 1561 (w), 1512 (m), 1509 (m), 1484 (w), 1459 (w), 1455 (m), 1444 (m), 1438 (m), 1405 (w), 1375 (m), 1302 (w), 1284 (m), 1244 (s), 1176 (m), 1148 (w), 1142 (w), 1107 (m), 1072 (w), 1026 (m), 1012 (m), 959 (w), 937 (m), 882 (w), 852 (w), 830 (m), 817 (w), 804 (s), 780 (s), 768 (s), 734 (m), 700 (m), 672 (m), 665 (m) cm^{-1}.

2.5.7 Preparation of 9-(4-methoxyphenyl)-10-(naphthalen-2-yl)anthracene (2c)

Prepared analogously to 1a using 9-bromo-10-(naphthalene-2-yl)anthracene (0.93 g, 2.44 mmol), 4-methoxybenzeneboronic acid (0.74 g, 4.86 mmol), K_2CO_3 (1.00 g, 7.24 mmol) and $Pd(PPh_3)_4$ (0.42 g, 0.36 mmol) in 318 mL of the solvent mixture yielding an off-white crude solid. The crude product was recrystallized in isopropanol (Yield 0.39 g, 0.94 mmol, 39%) and further purified through sublimation at a temperature range of 155–180°C under a pressure of 10^{-3} Torr with CO_2 as a carrier gas, which afforded 2c as white crystals. Yield 0.33 g (0.80 mmol, 33%). GC/MS reported an elution time of 26.614 min with abundance of $1.7x10^5$ and also reported an M^+ peak of 410.2 m/z compared to a prediction of 410.17 m/z. MP: 257–261°C. ^{1}H NMR (δ, 400 MHz, $CDCl_3$): 7.90–8.09 (4H, m), 7.71–7.80 (4H, m), 7.57–7.63 (3H, m), 7.41–7.45 (2H, m), 7.29–7.41 (4H, m), 7.15–7.19 (2H, m), 3.98 (3H, s). ^{13}C NMR (δ, 100 MHz, $CDCl_3$): 159.21 (1C), 137.23 (1C), 136.87 (1C), 136.81 (1C), 133.58 (1C), 132.91 (1C), 132.55 (2CH), 131.25 (1C), 130.40

(2C), 130.39 (1CH), 130.24 (2C), 129.74 (1CH), 128.24 (1CH), 128.10 (1CH), 128.05 (1CH), 127.26 (2CH), 127.15 (2CH), 126.56 (1CH), 126.34 (1CH), 125.21 (2CH), 125.09 (2CH), 114.05 (1CH), 114.04 (1CH), 55.55 ($1CH_3$). FT-IR (ν_{max}): 3035 (w), 2954 (w), 2932 (w), 2901 (w), 2835 (w), 1720 (w), 1702 (w), 1686 (w), 1655 (w), 1605 (w), 1560 (w), 1544 (w), 1509 (m), 1459 (w), 1438 (w), 1395 (w), 1296 (w), 1285 (w), 1271 (w), 1241 (s), 1202 (w), 1173 (m), 1136 (w), 1107 (w), 1033 (m), 1028 (m), 968 (w), 954 (w), 936 (m), 902 (w), 880 (w), 858 (w), 850 (w), 830 (w), 823 (m), 815 (m), 786 (w), 771 (m), 763 (s), 751 (s), 733 (m), 720 (w), 698 (w), 697 (w), 675 (m), 667 (m), 663 (m), 652 (w) cm^{-1}.

2.5.8 Preparation of 9-(4-methoxyphenyl)-10-(phenanthrene-10-yl)anthracene (2d)

A bubbled-degassed solution of DMF and water (9:1, 150 mL) was transferred to a mixture of 9-bromo-10-(phenanthrene-10-yl)anthracene (1.50 g, 3.46 mmol), 4-methoxybenzeneboronic (1.19 g, 7.83 mmol), K_2CO_3 (1.62 g, 11.74 mmol) and $Pd(PPh_3)_4$ (0.68 g, 0.59 mmol). The reaction was stirred for 16 hours at 90°C. After the reaction was cooled to room temperature, water (1.5 L) was added to the reaction. The resulting precipitate was filtered, washed with water and dried. Sublimation at a temperature range of 220–245°C under a pressure of 10^{-3} Torr with CO_2 as a carrier gas, which afforded 2d as faint yellow crystals. Yield 1.26 g (2.74 mmol, 79%). GC/MS reported an elution time of 51.288 min with abundance of $4.3x10^5$ and also reported an M^+ peak of 460.3 m/z compared to a prediction of 460.3 m/z. MP: 298–302°C. ^1H NMR (δ, 400 MHz, $CDCl_3$): 8.88–8.90 (2H, m), 7.92–7.95 (1H, m), 7.76–7.88 (4H, m), 7.65–7.71 (2H, m), 7.58–7.60 (2H, m), 7.46–7.54 (2H, m), 7.32–7.36 (3H, m), 7.18–7.28 (5H, m), 4.00 (3H, s). ^{13}C NMR (δ, 100 MHz, $CDCl_3$): 159.25 (1C), 137.56 (1C), 135.63 (1C), 134.80 (1C), 132.89 (1C), 132.61 (1CH), 132.59 (1CH), 131.92 (1C), 131.22 (1C), 130.89 (2C), 130.64 (1C), 130.57 (1C), 130.49 (2C), 130.15 (1CH), 128.93 (1CH), 127.71 (1CH), 127.34 (2CH), 127.21 (2CH), 127.10 (1CH), 127.04 (2CH), 126.84 (1CH), 125.39 (2CH), 125.19 (2CH), 123.00 (1CH), 122.88 (1CH), 114.09 (1CH), 114.04 (1CH), 55.56 ($1CH_3$). FT-IR (ν_{max}): 3060 (w), 3034 (w), 2953 (w), 2931 (w), 2899 (w), 2835 (w), 1606 (w), 1561 (w), 1510 (m), 1450 (w), 1438 (w), 1407 (w), 1390 (w), 1368 (w), 1310 (w), 1284 (m), 1281 (m), 1241 (m), 1172 (m), 1144 (w), 1108 (w), 1031 (m), 951 (w), 930 (w), 904 (w), 848 (w), 829 (m), 816 (w), 790 (w), 769 (s), 758 (m), 747 (s), 735 (s), 725 (s), 717 (m), 684 (m), 671 (m), 665 (m), 660 (m) cm^{-1}.

2.5.9 Electrochemistry

Cyclic voltammetry was performed using a BASi Epsilon potentiostat employing a glass cell and platinum wires for working, counter and pseudo-reference electrodes. The measurements were carried out on acetonitrile solutions (dried by J. C. Meyer solvent purification system and stored over 3 Å molecular sieves) containing 0.1 M tetrabutylammonium hexafluorophosphate (Oakwood) as supporting electrolyte with a scan rate of 100 mV/s. The experiments were referenced to the Fc/Fc+ redox couple of ferrocene at +0.475 V vs. SCE [36-38, 47].

2.5.10 Thermogravimetric Analysis

TGA analyses were performed in 70 ul alumina crucible using a TGA/DSC 1 Mettler Tolledo instrument under nitrogen gas with a heating rate of 5.0 °C min^{-1}. All compounds, where the decomposition temperature (T_d) is determined at 5% weight loss.

2.5.11 Crystallographic Characterization

Crystallographic data were collected from single crystals mounted on thin glass fibers using parabar oil and secured with clear nail polish. Data were collected on a Bruker Smart or Kappa APEX II single crystal diffractometer equipped with a graphite monochromator. Both instruments are equipped with a sealed tube Mo Kα source ($\lambda = 0.71073$ Å), an APEX II CCD detector and a dry compressed air cooling system. All samples were cooled to 200(2) K during data collection except for 2d which remained at room temperature. Raw data collection and processing were performed with the APEX3 software package from Bruker [48]. Initial unit cell parameters were determined from 36 data frames from select ω scans. Semi-empirical absorption corrections based on equivalent reflections were applied [49]. Systematic absences in the diffraction data-set and unit-cell parameters were consistent with the assigned space group. The initial structural solutions were determined using SHELXT direct methods [50], and refined with full-matrix least-squares procedures based on F^2 using SHELXL or ShelXle [51]. Hydrogen atoms were placed geometrically and refined using a riding model.

2.5.12 Electrical Characterization

Organic thin film transistors (OTFTs) were fabricated in a bottom gate bottom contact configuration by spin coating the organic semiconductor onto Si/SiO_2 substrates with prefabricated

gold source-drain electrodes from Fraunhofer IPMS (W= 2000 μm, L = 2.5 μm). Prior to deposition, the substrates were washed by sequential sonication baths (5 min each) in soapy water, acetone, isopropanol and dried with nitrogen followed by oxygen plasma for 15 minutes to clean and hydrolyze the surface. Substrates were then rinsed with water and isopropanol then dried in nitrogen, before a 1.0 hour surface treatment in 1% v/v octyltrichlorosilane (OTS) in toluene at 70 °C [52] . Silane-treated substrates were washed with toluene and isopropanol and dried for 1 hour at 70 °C under vacuum. 10 mg mL^{-1} solutions of compounds 1-5 were spin-coated by applying 1 mL drops of the respective solution onto the pre-patterned substrates and rotating at 2000 RPM. The substrates were then allowed to dry at 40°C for 30 min under vacuum. Chloroform was used as the solvent to spin-coat material onto the substrate surface at 2000 RPM. All channels lengths were tested (2.5, 5.0, 10.0, 20.0 μm). All values were taken as an average value from a minimum of four working devices. Characterization was performed in air. Electrical measurements were performed using a custom electrical probe station with a chamber allowing for controlled atmosphere, oesProbe A10000-P290 (Element Instrumentation Inc. & Kreus Design Inc.) with a Keithley 2614B to control source-drain voltage (V_{DS}), gate voltage (V_{GS}), and measure source-drain current (I_{DS}). V_{DS} was maintained at a constant -50 V while V_{GS} was varied from -40 V to -80 V to obtain measurements of I_{DS}. From these measurements, saturation-region field-effect mobility, on/off current ratio, and threshold voltage were determined.

The general expression relating current to field-effect mobility and gate voltage in the saturation mode is given in Equation 1:

$$I_{DS} = \frac{\mu C_i W}{2L}(V_{GS} - V_T)^2 \quad (1)$$

Where I_{DS} is the source-drain voltage, μ is the field-effect mobility of the material (electron mobility in this study), C_i is the capacitance, W is the width of the channel, L is the length of the channel, V_{GS} is the gate-source voltage, and V_T is the threshold voltage. To obtain a linear relation, the square root of Equation 1 is taken, giving Equation 2, so that the mobility and threshold voltage can be calculated directly from the slope and x-intercept of an $\sqrt{I_{DS}}$ vs V_{GS} curve, respectively.

$$\sqrt{I_{\mathrm{DS}}} = \sqrt{\frac{\mu C_{\mathrm{i}} W}{2L}} (V_{\mathrm{GS}} - V_{\mathrm{T}}) \quad (2)$$

Finally, the on/off ratio is determined by Equation 3:

$$\mathrm{On/Off\ Ratio} = \frac{I_{\mathrm{on}}}{I_{\mathrm{off}}} \quad (3)$$

Where I_{on} and I_{off} are the highest and lowest currents, respectively, measured in the characterized gate voltage range.

References

1. Chang, Y. L.; Song, Y.; Wang, Z.; Helander, M. G.; Qiu, J.; Chai, L.; Liu, Z.; Scholes, G. D.; Lu, Z. Highly Efficient Warm White Organic Light-Emitting Diodes by Triplet Exciton Conversion. Adv. Funct. Mater. 2013, 23 (6), 705–712.
2. Qiu, J.; Greiner, M.; Liu, Z.; Helander, M. G. Unlocking the Full Potential of Organic Light-Emitting Diodes on Flexible Plastic. 2011, No. October.
3. Piliego, C.; Jarzab, D.; Gigli, G.; Chen, Z.; Facchetti, A.; Loi, M. A. High Electron Mobility and Ambient Stability in Solution-Processed Perylene-Based Organic Field-Effect Transistors. Adv. Mater. 2009, 21 (16), 1573–1576.
4. Bettinger, C. J.; Becerril, H. A.; Kim, D. H.; Lee, B. L.; Lee, S.; Bao, Z. Microfluidic Arrays for Rapid Characterization of Organic Thin-Film Transistor Performance. Adv. Mater. 2011, 23 (10), 1257–1261.
5. Chen, H. Z.; Shi, M. M.; Aernouts, T.; Wang, M.; Borghs, G.; Heremans, P. A Novel Organic N-Type Material: Fluorinated Perylene Diimide. Sol. Energy Mater. Sol. Cells 2005, 87 (1–4), 521–527. https://doi.org/10.1016/j.solmat.2004.07.056.
6. Tian, H.; Han, Y.; Bao, C.; Yan, D.; Geng, Y.; Wang, F. An Asymmetric Oligomer Based on Thienoacene for Solution Processed Crystal Organic Thin-Film Transistors. Chem. Commun. 2012, 48 (29), 3557–3559.
7. Ma, R.-Q.; Hewitt, R.; Rajan, K.; Silvernail, J.; Urbanik, K.; Hack, M.; Brown, J. J. Flexible Active-Matrix OLED Displays: Challenges and Progress. J. Soc. Inf. Disp. 2007, 16 (1), 169.
8. Glawe, A.; Eggerath, D.; Schäfer, F. Printing versus Coating - What Will Be the Future Production Technology for Printed Electronics? 2015, 1646 (February 2015), 87–90.
9. Boileau, N. T.; Melville, O. A.; Mirka, B.; Cranston, R. RSC Advances P and N Type Copper Phthalocyanines as e Ff Ective Semiconductors in Organic Thin- Fi Lm Transistor Based DNA Biosensors at Elevated Temperatures †. 2019, 2133–2142.
10. Chen, M.; Yan, L.; Zhao, Y.; Murtaza, I.; Meng, H.; Huang, W. Anthracene-Based Semiconductors for Organic Field-Effect Transistors. J. Mater. Chem. C 2018, 6 (28), 7416–7444.

11. Xie, H.; Cheng, C. Y.; Li, L.; Deng, X. Y.; Yang, K. K.; Wang, Y. Z. Integrating Shape-Memory Technology and Photo-Imaging on a Polymer Platform for a High-Security Information Storage Medium. J. Mater. Chem. C 2018, 6 (39), 10422–10427.

12. Kommandeur, J. Photoconductivity in Organic Single Crystals. J. Phys. Chem. Solids 1961, 22 (C), 339–349.

13. LeBlanc, O. H. Band Structure and Transport of Holes and Electrons in Anthracene. J. Chem. Phys. 1961, 35 (4), 1275–1280

14. Quinn, J. T. E.; Zhu, J.; Li, X.; Wang, J.; Li, Y. Recent Progress in the Development of N-Type Organic Semiconductors for Organic Field Effect Transistors. J. Mater. Chem. C 2017, 5 (34), 8654–8681.

15. Dong, H.; Fu, X.; Liu, J.; Wang, Z.; Hu, W. 25th Anniversary Article: Key Points for High-Mobility Organic Field-Effect Transistors. Adv. Mater. 2013, 25 (43), 6158–6183.

16. Zhang, X.; Zhao, G.; Zhen, Y.; Tu, Z.; He, P.; Yi, Y.; Dong, H.; Hu, W. The Position Effect of an Ethynyl Spacer on the Carrier Mobility of Anthracene Derivatives. J. Mater. Chem. C 2015, 3 (21), 5368–5371.

17. Chaari, M.; Kelemen, Z.; Planas, J. G.; Teixidor, F.; Choquesillo-Lazarte, D.; Ben Salah, A.; Viñas, C.; Núñez, R. Photoluminescence in: M -Carborane-Anthracene Triads: A Combined Experimental and Computational Study. J. Mater. Chem. C 2018, 6 (42), 11336–11347.

18. Liu, J.; Dong, H.; Wang, Z.; Ji, D.; Cheng, C.; Geng, H.; Zhang, H.; Zhen, Y.; Jiang, L.; Fu, H.; et al. Thin Film Field-Effect Transistors of 2,6-Diphenyl Anthracene (DPA). Chem. Commun. 2015, 51 (59), 11777–11779.

19. Liu, J.; Zhang, H.; Dong, H.; Meng, L.; Jiang, L.; Jiang, L.; Wang, Y.; Yu, J.; Sun, Y.; Hu, W.; et al. High Mobility Emissive Organic Semiconductor. Nat. Commun. 2015, 6 (May), 1–8.

20. Yan, L.; Zhao, Y.; Yu, H.; Hu, Z.; He, Y.; Li, A.; Goto, O.; Yan, C.; Chen, T.; Chen, R.; et al. Influence of Heteroatoms on the Charge Mobility of Anthracene Derivatives. J. Mater. Chem. C 2016, 4 (16), 3517–3522.

21. Li, A.; Yan, L.; Liu, M.; Murtaza, I.; He, C.; Zhang, D.; He, Y.; Meng, H. Highly Responsive Phototransistors Based on 2,6-Bis(4-Methoxyphenyl)Anthracene Single Crystal. J. Mater. Chem. C 2017, 5 (22), 5304–5309

22. Payne, M. M.; Parkin, S. R.; Anthony, J. E.; Kuo, C. C.; Jackson, T. N. Organic Field-Effect Transistors from Solution-Deposited Functionalized Acenes with Mobilities as High as 1 Cm2/V·s. J. Am. Chem. Soc. 2005, 127 (14), 4986–4987.

23. Liu, J.; Liu, J.; Zhang, Z.; Xu, C.; Li, Q.; Zhou, K.; Dong, H.; Zhang, X.; Hu, W. Enhancing Field-Effect Mobility and Maintaining Solid-State Emission by Incorporating 2,6-Diphenyl Substitution to 9,10-Bis(Phenylethynyl)Anthracene. J. Mater. Chem. C 2017, 5 (10), 2519–2523.

24. Zafar, M. N.; Mohsin, M. A.; Danish, M.; Nazar, M. F.; Murtaza, S. Palladium Catalyzed Heck − Mizoroki and Suzuki − Miyaura Coupling Reactions (Review). Russ. J. Coord. Chem. 2014, 40 (11), 781–800.

25. Smith, G. B.; Dezeny, G. C.; Hughes, D. L.; King, A. O.; Verhoeven, T. R. Mechanistic Studies of the Suzuki Cross-Coupling Reaction. J. Org. Chem. 1994, 59, 8151–8156.

26. Wan, Z.; Qi, W.; Xing, F.; Li, Y. Anthracene-Based Derivatives : Synthesis , Photophysical Properties and Electrochemical Properties. 2017, 33 (4).

27. Online, V. A. Extremely Deep Blue and Highly Efficient Non-Doped Organic Light Emitting Diodes Using an Asymmetric Anthracene Derivative with a Xylene Unit †. 2013, 4664–4666.

28. Wang, Z.; Xu, C.; Wang, W.; Duan, L.; Li, Z. High-Color-Purity and High-Efficiency Non-Doped Deep-Blue Electroluminescent Devices Based on Novel Anthracene Derivatives W. 2012, 662–667.

29. Serevic, T. Transport Properties †. 2014, 7089–7101.

30. Angelis, R. De; Industriale, I.; Tor, R.; Chimiche, T.; Tor, R. Synthesis and Photophysical Properties Of. 2015, No. November, 943–952.

31. Gidron, O.; Dadvand, A.; Wei-Hsin Sun, E.; Chung, I.; Shimon, L. J. W.; Bendikov, M.; Perepichka, D. F. Oligofuran-Containing Molecules for Organic Electronics. J. Mater. Chem. C 2013, 1 (28), 4358–4367.

32. Dadvand, A.; Sun, W. H.; Moiseev, A. G.; Bélanger-Gariépy, F.; Rosei, F.; Meng, H.; Perepichka, D. F. 1,5-, 2,6- and 9,10-Distyrylanthracenes As Luminescent Organic Semiconductors. J. Mater. Chem. C 2013, 1 (16), 2817–2825.

33. Usta, H.; Kim, C.; Wang, Z.; Lu, S.; Huang, H.; Facchetti, A.; Marks, T. J. Anthracenedicarboximide-Based Semiconductors for Air-Stable, n-Channel Organic Thin-Film Transistors: Materials Design, Synthesis, and Structural Characterization. J. Mater. Chem. 2012, 22 (10), 4459–4472.

34. Chen, M.; Zhao, Y.; Yan, L.; Yang, S.; Zhu, Y.; Murtaza, I.; He, G.; Meng, H.; Huang, W. A Unique Blend of 2-Fluorenyl-2-Anthracene and 2-Anthryl-2-Anthracence Showing White Emission and High Charge Mobility. Angew. Chemie - Int. Ed. 2017, 56 (3), 722–727.

35. Dadvand, A.; Moiseev, A. G.; Sawabe, K.; Sun, W. H.; Djukic, B.; Chung, I.; Takenobu, T.; Rosei, F.; Perepichka, D. F. Maximizing Field-Effect Mobility and Solid-State Luminescence in Organic Semiconductors. Angew. Chemie - Int. Ed. 2012, 51 (16), 3837–3841.

36. Ding, S. Y.; Gao, J.; Wang, Q.; Zhang, Y.; Song, W. G.; Su, C. Y.; Wang, W. Construction of Covalent Organic Framework for Catalysis: Pd/COF-LZU1 in Suzuki-Miyaura Coupling Reaction. J. Am. Chem. Soc. 2011, 133 (49), 19816–19822.

37. Aranzaes, J. R.; Daniel, M.-C.; Astruc, D. Metallocenes as References for the Determination of Redox Potentials by Cyclic Voltammetry — Permethylated Iron and Cobalt Sandwich Complexes, Inhibition by Polyamine Dendrimers, and the Role of Hydroxy-Containing Ferrocenes. Can. J. Chem. 2006, 84 (2), 288–299.

38. Li, Y.; Cao, Y.; Gao, J.; Wang, D.; Yu, G.; Heeger, A. J. Electrochemical Properties of Luminescent Polymers and Polymer Light-Emitting Electrochemical Cells. Synth. Met. 2002, 99 (3), 243–248.

39. Dang, M. T.; Grant, T. M.; Yan, H.; Seferos, D. S.; Lessard, B. H.; Bender, T. P. Bis(Tri-n-Alkylsilyl Oxide) Silicon Phthalocyanines: A Start to Establishing a Structure Property Relationship as Both Ternary Additives and Non-Fullerene Electron Acceptors in Bulk Heterojunction Organic Photovoltaic Devices. J. Mater. Chem. A 2017, 5 (24), 12168–12182.

40. Lohrman, J.; Zhang, C.; Zhang, W.; Ren, S. Semiconducting Carbon Nanotube and Covalent Organic Polyhedron-C60nanohybrids for Light Harvesting. Chem. Commun. 2012, 48 (67), 8377–8379.

41. Silvestri, F.; Marrocchi, A.; Seri, M.; Kim, C.; Marks, T. J.; Facchetti, A.; Taticchi, A. Solution-Processable Low-Molecular Weight Extended Arylacetylenes: Versatile p-Type Semiconductors for Field-Effect Transistors and Bulk Heterojunction Solar Cells. J. Am. Chem. Soc. 2010, 132 (17), 6108–6123.

42. Hanif, M.; Zhi-ming, W.; Bing, Y.; Ping, L. U.; Yu-guang, M. A. Thermal and Optoelectronic Properties of Anthracene and Dibenz [a , c] Anthracene. 2013, 29 (1), 110–115.

43. Atxabal, A.; Arnold, T.; Parui, S.; Hutsch, S.; Zuccatti, E.; Llopis, R.; Cinchetti, M.; Ortmann, F.; Hueso, L. E. Tuning the Charge Fl Ow between Marcus Regimes. No. 2019, 1–7.

44. Yuan, L.; Wang, L.; Garrigues, A. R.; Jiang, L.; Annadata, H. V.; Antonana, M. A.; Barco, E.; Nijhuis, C. A. Marcus Regions in Molecular Junctions via Molecular Orbital Gating. 2018, 13 (April).

45. Wang, C.; Wang, F.; Yang, X.; Li, Q.; Shuai, Z. Theoretical Comparative Studies of Charge Mobilities for Molecular Materials : Pet versus Bnpery. 2008, 9, 635–640.

46. Schmidt, R.; Göttling, S.; Leusser, D.; Stalke, D.; Krause, A. M.; Würthner, F. Highly Soluble Acenes as Semiconductors for Thin Film Transistors. J. Mater. Chem. 2006, 16 (37), 3708–3714.

47. Transactions, E. C. S.; Society, T. E. Measurements and Prediction of Electronic Properties of Discotic Triphenylenes and Phthalocyanines Mohamed M. Ahmida and S. Holger Eichhorn *. 2010, 25 (26), 1–10.

48. Diffraction, X. APEX2 Release 2010. 2010, No. May.

49. Blessing, B. Y. R. H. An Empirical Correction for Absorption Anisotropy. 1995, 33–38.

50. Hu, C. B.; Sheldrick, G. M.; Dittrich, B. ShelXle : A Qt Graphical User Interface for SHELXL. 2011, 1281–1284.

51. Sheldrick, G. M. A Short History of SHELX. 2008, 112–122. https://doi.org/10.1107/S0108767307043930.

52. Brixi, S.; Melville, O. A.; Boileau, N. T.; Lessard, B. H. The Influence of Air and Temperature on the Performance of PBDB-T and P3HT in Organic Thin Film Transistors. J. Mater. Chem. C 2018, 6 (44), 11972–11979.

Preamble:

Seven novel 9,10-substituted anthracene-based molecules were synthesized and characterized. We began with this particular set of anthracene derivatives because only a small handful of molecules have been reported to date; all with modest charge mobilities. We determined that substitution of the 9,10-position is an effective way to tune the thermal stability of the material while having negligible effects on the frontier molecular orbital energy levels. Furthermore, 9,10-position changes in solid-state packing motifs resulted in OTFTs with modest performance. Consequently, moiety functionalization of 9,10-position anthracene proved to have little to no effect on electrochemical or optical properties. We decided to focus on the development of new anthracene molecules with similar functionalization groups but in the 2,6-position instead of the 9,10-position. Therefore, we reported anthracene derivatives with following 2,6-position functional groups: 2-fluorophenyl, 3-fluorophenyl, 4-fluorophenyl, 3-(trifluoromethyl)phenyl, 4-(trifluoromethyl)phenyl, and 3,4,5-trifluorophenyl. In a similar approach to 9,10-functionalization, we would synthesize and characterize these novel molecules and compare them to the 9,10-functionalizd derivatives.

3.0 Developing and Comparing 2,6-anthracene Derivatives: Optical, Electrochemical, Thermal, and Their Use in Organic Thin Film Transistors

3.1 Contributions of Authors

This section describes the context in which the research was performed, relating it to the development of the lab and my own research goals at the time. It describes the contributions of each author and the significance of the research.

Supplementary Materials: The following are available online at https://www.mdpi.com/1996-1944/13/8/1961, crystallography, cyclic voltammetry and UV-Vis absorption spectroscopy.

Author Contributions: Conceptualization was performed by B.H.L. and J.L.B. Methodology by, M.Y.V., N.J.Y., O.A.M.; validation, M.Y.V., N.J.Y., O.A.M., A.J.D., J.S.O.; formal analysis, M.Y.V., N.J.Y., J.S.O.; investigation, M.Y.V., N.J.Y., O.A.M., J.S.O.; data curation, M.Y.V., N.J.Y.; writing—original draft preparation, M.V.; writing—review and editing, N.J.Y., O.A.M., J.L.B., B.H.L.; supervision, J.L.B. and B.H.L.; project administration, J.L.B. and B.H.L.; funding acquisition, J.L.B. and B.H.L. All authors have read and agreed to the published version of the manuscript.

The rest of this section has been adapted from Materials by MDPI: Vorona M.Y.; Yutronkie, N.J.; Melville, O.A.; Daszczynski, A.J.; Ovens, J.S.; Brusso, J.L.; Lessard, B.H. Developing and Comparing 2,6-Anthracene Derivatives: Optical, Electrochemical, Thermal, and Their Use in Organic Thin Film Transistors. Materials vol. 13, no. 8, pp. 1–16, 2020. https://doi.org/10.3390/ma13081961

3.2 Abstract

Anthracene-based semiconductors have attracted great interest due to their molecular planarity, ambient and thermal stability, tunable frontier molecular orbitals and strong intermolecular interactions that can lead to good device field-effect transistor performance. In this study, we report the synthesis of six anthracene derivatives which were di-substituted at the 2,6-positions, their optical, electrochemical and thermal properties, and their single crystal structures. It was found

that 2,6-functionalization with various fluorinated phenyl derivatives led to negligible changes in the optical behaviour while influencing the electrochemical properties. Furthermore, the choice of fluorinated phenyl moiety had noticeable effects on melting point and thermal stability (ΔT_m < 55 °C and ΔT_d < 65 °C). Bottom-gate top-contact (BGTC) organic thin transistors (OTFTs) were fabricated and characterized using the 2,6-anthracene derivatives as the semiconducting layer. The addition of fluorine groups on the phenyl groups led to a transition from p-type behaviour to n-type behaviour in BGBC OTFTs.

3.3 Introduction

Organic light emitting diodes (OLEDs) [1,2] and other organic electronic devices such as organic photovoltaics (OPVs) [3] and organic thin film transistors (OTFTs) [4] can be fabricated using physical vapour deposition (PVD) at significantly lower temperatures than traditional inorganic semiconductor manufacturing [5–8]. Therefore, PVD can lead to low-cost, high throughput fabrication of large area electronics. In this capacity, OTFTs demonstrate promise as the cornerstone components of next generation electronic devices [5, 7–13].

The choice of the organic semiconducting (OSC) material is critical to the manufacturability and desired operation of an OTFT Various materials have been examined over the last few decades for use as the OSC in OTFTs [14]. Anthracene, the first organic molecule used to study organic semiconductivity in the late-1950s, and its derivatives are still a promising candidate as an OSC [15, 16]. For instance, in 2003 researchers were able to develop anthracene-base molecules with p-type mobilities as high as 0.02 $cm^2\ V^{-1}s^{-1}$ [17, 18]. Over the past two decades, hundreds of derivatives have been synthesized, characterized and integrated into devices, providing a sound foundation for the development of structure–property–mobility relationships for anthracene-based OSCs [14, 19]. In 2015 Liu et al. reported that 2,6-diphenyl anthracene (2,6-DPA) produced record mobilities [20,21]. There are several factors that account for the performance of anthracene-derivatives; however, the most common are: (1) alignment of the frontier molecular orbital energy levels of the material with the Fermi level of the source and drain electrodes, which corresponds to barrier for electron or hole injection; (2) solid-state molecular packing arrangement in either the herringbone or lamellar motif, along with intermolecular distances between adjacent molecules, which serve a crucial role in charge mobility; and (3) ordered stacking and grain density of the thin

film morphology, whereby few boundaries and traps optimize charge mobility [14,22,23]. Environmental stability and operating conditions are also important considerations that affect overall device performance and longevity, but are commonly overlooked when studying OTFT performance. Both p- and n-type OSC devices have been shown to be strongly affected by environmental factors such as temperature, light, humidity exposure and atmosphere (ambient, inert and vacuum) [24–26].

X-ray diffraction (XRD) can elucidate the packing structure of a derivative, quantifying the distances between molecules and their supramolecular arrangements in a single crystal. A shorter distance between adjacent molecules results in greater π-orbital overlap, which often leads to greater charge mobility. For example, the tightly packed herringbone motif of 2,6-DPA crystals indicates strong π–π interactions which may contribute to high charge mobility in a less ordered thin-film [20, 21, 27]. Therefore, the analysis of the crystal structure can provide insight into how anthracene-derivatives pack in a thin film. Chemically modifying an anthracene core by coupling reactions can extend electron delocalization throughout the structure, tune the molecular packing motif, alter the highest occupied molecular orbital (HOMO) and lowest unoccupied molecular orbital (LUMO) energy levels, changing the thermal stability of the derivative. Control of these variables is crucial to obtaining a well-functioning OTFT [14, 27, 28].

A wide variety of high-mobility 2,6-functionalized anthracene derivatives have been synthesized in the last few years; however, only one 2,6-fluorophenyl anthracene derivative has been reported [14]. In our previous study, we reported a series of 9,10-functionalized anthracene derivatives and fabricated preliminary OTFTs with modest performance [29]. In this study, we report five novel 2,6-fluorophenyl anthracene derivatives and their incorporation into OTFTs. We compare these devices to OTFTs using 2,6-DPA and another 2,6-fluorophenyl anthracene derivative developed in 2004 by Yamashita et al. [30]. We attempt to describe the intermolecular interactions in the single crystals of the derivatives and relate them to OTFT device performance. In doing so, we also characterize their optical, electrochemical and thermal properties to further elucidate structure–property–mobility relationship for anthracene-based semiconductors.

3.3 Materials and Methods

3.3.1 General Methods and Procedures

The reagents 2,6-dibromoanthracene (Lumtec Corp., Taipei, Taiwan), 2,6-diphenylanthracene (Lumtec Corp., Taipei, Taiwan), 4-fluorophenylboronic acid (Oakwood Products Inc., Estill, SC, USA), 3-fluorophenylboronic acid (Oakwood Products Inc., Estill, SC, USA), 2-fluorophenylboronic acid (Oakwood Products Inc., Estill, SC, USA) 3,4,5-trifluorophenylboronic acid (Oakwood Products Inc., Estill, SC, USA) 4-trifluoromethylphenylboronic acid (Oakwood Products Inc., Estill, SC, USA), 3-trifluoromethylphenylboronic acid (Oakwood Products Inc., Estill, SC, USA) potassium carbonate (K_2CO_3) (Oakwood Products Inc., Estill, SC, USA), tetrakis(triphenylphosphine)palladium(0) ($Pd(PPh_3)_4$) (Strem Chemicals, Newburyport, MA, USA), toluene, N-methyl-2-pyrrolidone (NMP) (Caledon Laboratories Ltd., Georgetown, ON, Canada), and ethanol were commercially obtained and used as received. All solvents used were ACS grade. Dry nitrogen gas was used as the atmosphere. All reactions were performed under an atmosphere of dry nitrogen.

TGAs were performed in 70 µl alumina crucible using a TGA/DSC 1 Mettler Tolledo instrument (Mettler Tolledo, Columbus, Ohio, USA) under nitrogen gas with a heating rate of 5.0 °C min^{-1}. Mel-Temp apparatus was used to take all melting-points and are reported as uncorrected values. Agilent Technologies Cary 630 FT-IR spectrometer was used to record IR spectra of each compound. A Varian Cary Series 6000 UV-Vis-NIR spectrophotometer (Agilent, Santa Clara, California, USA) was used to measure the UV-Vis spectra and a Varian Cary Eclipse fluorescence spectrophotometer was used to obtain the photoluminescence spectra. HQGC-grade DCM solutions were used to measure all the UV-Vis and fluorescence spectra in 1 cm precision quartz cuvettes. All NMR spectra were run on the Bruker 400 MHz spectrometer (Bruker, Billerica, MA, USA) in DMSO solution at room temperature. Bruker DektakXT Profilometer (Bruker, Billerica, MA, USA) was used to obtain film thickness measurements. Gas Chromatgraphy/Mass Sectrometry (GC/MS) was performed using Agilent 6890 GC (Agilent, Santa Clara, California, USA) coupled to Agilent 5975 M equipped with a HP-5MS column (30 m × 250 µm × 0.25 µm), and a flowrate of 1.6 mL min^{-1}. The initial oven temperature was 275 °C, held for 15 min, then ramped to 300 °C (40 °C /min) and held for 25 min. A 1,2-dichloroethane and toluene solvent

mixture was used for all GC/MS experiments. The same procedure was used for all compounds. Stoichiometric loadings and sublimation temperature varied with each derivative.

3.3.2 Preparation of 2,6-bis(2-fluorophenyl)anthracene (o-FPh)

A bubbled-degassed solution of NMP and water (9:1, 150 mL) was transferred to a mixture of 2,6-dibromoanthracene (1.50 g, 4.46 mmol), 2-fluorophenylboronic acid (1.62 g, 11.60 mmol), K_2CO_3 (1.62 g, 11.74 mmol), and $Pd(PPh_3)_4$ (52.6 mg, 0.59 mmol). The reaction was stirred for 16 h at 90 °C. After the reaction was cooled to room temperature, 1.0 M NaOH solution (1.5 L) was added to the reaction. The resulting precipitate was filtered, washed with water, and dried. Sublimation at a temperature range of 185–205 °C under a pressure of 10^{-3} Torr with CO_2 as a carrier gas, which afforded o-FPh as faint yellow crystals (Yield 1.36 g, 4.04 mmol, 91%). GC/MS reported an elution time of 6.517 min with abundance of 2.2×10^5, and also reported an M^+ peak of 366.0 m/z compared to a prediction of 366.32 m/z. MP: 195–205 °C. ^{1}H NMR (δ, 400 MHz, DMSO): 8.61–8.72 (3H, m), 8.40–8.43 (1H, m), 8.29–8.36 (1H, m), 8.18–8.25 (1H, m), 8.07–8.11 (1H, m), 7.71–7.77 (3H, m), 7.61–7.66 (1H, m), 7.45–7.56 (2H, m), 7.34–7.42 (3H, m). ^{19}F NMR (δ, 400 MHz, DMSO): 117.72–117.88 (m). ^{13}C NMR (δ, 100 MHz, DMSO): 159.72 (2C), 133.28 (2C), 131.89 (2C), 130.59 (2C), 129.03 (2C), 133.01 (2CH), 131.01 (2CH), 130.21 (2CH), 127.28 (2CH), 125.82 (2CH), 125.51 (2CH), 124.81 (2CH), 114.74 (2CH). FT-IR (ν_{max}): 1801 (w), 1705 (w), 1701 (w), 1686 (w), 1664 (w), 1653 (w), 1611 (s), 1575 (w), 1565 (w), 1527 (w), 1495 (s), 1467 (m), 1447 (s), 1402 (m), 1310 (w), 1267 (w), 1262 (w), 1234 (w), 1204 (s), 1156 (w), 1103 (m), 1049 (m), 1017 (w), 941 (w), 904 (s), 872 (m), 840 (w), 820 (m), 796 (s), 749 (s), 712 (m), 710 (w), 667 (m) cm^{-1}.

3.3.3 Preparation of 2,6-(3-fluorophenyl)anthracene (m-FPh)

Prepared analogously to o-FPh using 3-fluorophenylboronic acid (1.62 g, 11.60 mmol) yielding an off-white crude solid. Sublimation at a temperature range of 185–205°C under a pressure of 10^{-3} Torr with CO_2 as a carrier gas afforded m-FPh as white crystals (Yield 1.31 g, 3.58 mmol, 81%). GC/MS reported an elution time of 6.717 min with abundance of 4.6×10^5, and reported an M^+ peak of 366.2 m/z compared to a prediction of 366.46 m/z. MP: 250–258 °C. ^{1}H NMR (δ, 400 MHz, DMSO): 8.60–8.70 (3H, m), 7.22–7.30 (1H, m). 8.32–8.36 (1H, m), 8.18–8.25 (1H, m),

8.05–8.11 (1H, m), 7.89–7.98 (2H, m), 7.74–7.77 (3H, m), 7.52–7.65 (3H, m), 7.34–7.42 (1H, m). ^{19}F NMR (δ, 400 MHz, DMSO): 60.80–60.84 (s), 112.60–112.66 (m). ^{13}C NMR (δ, 100 MHz, DMSO): 161.02 (2C), 141.77 (2C), 133.34 (2C), 132.19 (2C), 131.29 (2C), 130.18 (2CH), 127.51 (2CH), 127.32 (2CH), 125.79 (2CH), 125.53 (2CH), 122.47 (2CH), 116.33 (2CH), 114.39 (2CH). FT-IR (ν_{max}): 2103 (w), 1933 (w), 1803 (w), 1609 (s), 1583 (w), 1521 (m), 1471 (s), 1445 (m), 1394 (m), 1333 (m), 1283 (w), 1238 (w), 1159 (w), 1140 (w), 1120 (w), 1073 (w), 1049 (s), 1014 (m), 964 (m), 913 (m), 900 (s), 865 (m), 840 (m), 796 (s), 740 (w), 710 (s), (m), 667 (w), 665 (w) cm^{-1}.

3.3.4 Preparation of 2,6-bis(4-fluorophenyl)anthracene (p-FPh)

Prepared analogously to o-FPh using 4-fluorophenylboronic acid (1.62 g, 11.60 mmol) yielding an off-white crude solid. Sublimation at a temperature range of 185–205 °C under a pressure of 10^{-3} Torr with CO_2 as a carrier gas afforded p-FPh as white crystals (Yield 1.29 g, 3.57 mmol, 80%). GC/MS reported an elution time of 6.780 min with abundance of 1.1×10^6, and reported an M^+ peak of 366.2 m/z compared to a prediction of 380.41 m/z. MP: 255–265 °C. ^{1}H NMR (δ, 400 MHz, DMSO): 8.59–8.69 (3H, m), 8.37–8.42 (3H, m). 8.16–8.22 (1H, m), 8.05–8.11 (2H, m), 7.85–7.96 (3H, m), 7.66–7.61 (2H, m), 7.33–7.41 (2H, m). ^{19}F NMR (δ, 400 MHz, DMSO): 114.86–115.16 (m). ^{13}C NMR (δ, 100 MHz, DMSO): 161.77 (2C), 137.18 (2C), 133.45 (2C), 132.28 (2C), 130.68 (2C), 133.22 (2CH), 131.56 (2CH), 131.18 (2CH), 126.79 (2CH), 126.56 (2CH), 125.78 (2CH), 116.02 (2CH), 116.10 (2CH). FT-IR (ν_{max}): 1805 (w), 1657 (w), 1606 (m), 1517 (m), 1464 (w), 1444 (m), 1406 (w), 1335 (m), 1301 (w), 1283 (w), 1249 (m), 1178 (w), 1159 (w), 1152 (w), 1100 (w), 1070 (w), 1048 (s), 1012 (m), 962 (m), 913 (m), 900 (s), 865 (m), 845 (m), 796 (s), 733 (w), 710 (s), (m), 691 (w), 654 (w) cm^{-1}.

3.3.5. Preparation of 2,6-bis(3-(trifluoromethyl)phenyl)anthracene (m-CF_3Ph)

Prepared analogously to o-FPh using 3-trifluoromethylbenzeneboronic acid (2.20 g, 11.60 mmol) yielding an off-white crude solid. Sublimation at a temperature range of 195–205°C under a pressure of 10^{-3} Torr with CO_2 as a carrier gas afforded m-CF_3Ph as white crystals (Yield 1.34 g, 2.87 mmol, 64%). GC/MS reported an elution time of 5.613 min with abundance of 4.1×10^5, and also reported an M^+ peak of 466.3 m/z compared to a prediction of 466.43 m/z. MP: 160–170 °C.

^{1}H NMR (δ, 400 MHz, DMSO): 8.61–8.77 (2H, m), 8.52–8.63 (2H, m), 8.17–8.27 (6H, m), 7.91–7.99 (2H, m), 7.77–7.81 (4H, m). ^{19}F NMR (δ, 400 MHz, DMSO): 60.90–60.95 (m). ^{13}C NMR (δ, 100 MHz, DMSO): 142.2 (2C), 133.32 (2C), 132.19 (2C), 131.52 (2C), 130.58 (2C), 130.74 (2CH), 130.14 (2CH), 129.51 (2CH), 127.37 (2CH), 127.01 (2CH), 126.51 (2CH), 125.02 (2CH), 124.98 (2CH), 124.44 (2C). FT-IR (ν_{max}): 1907 (w), 1851 (w), 1797 (w), 1736 (w), 1627 (w), 1529 (w), 1495 (w), 1439 (w), 1411 (w) 1394 (w), 1353 (m), 1327 (s), 1259 (s), 1229 (s), 1173 (m), 1128 (s), 1098 (m), 1072 (s), 1033 (s), 1001 (w), 989 (w), 970 (w), 927 (m), 908 (m), 899 (s), 866 (s), 850 (m), 822 (m), 794 (s), 736 (m), 697 (s), 669 (m), 660 (m) cm^{-1}.

3.3.6 Preparation of 2,6-bis(4-(trifluoromethyl)phenyl)anthracene (p-CF_3Ph)

Prepared analogously to o-FPh using 4-trifluoromethylbenzeneboronic acid (2.20 g, 11.60 mmol) yielding an off-white crude solid. Sublimation at a temperature range of 190-205°C under a pressure of 10^{-3} Torr with CO_2 as a carrier gas afforded p-CF_3Ph as white crystals (Yield 1.22 g, 2.65 mmol, 60%). GC/MS reported an elution time of 6.149 min with abundance of 5.7×10^5, and also reported an M^+ peak of 466.3 m/z compared to a prediction of 466.43 m/z. MP: 285–290 °C. ^{1}H NMR (δ, 400 MHz, DMSO): 8.76–8.83 (1H, m), 8.44–8.57 (2H, m), 8.22–8.29 (1H, m), 8.08–8.14 (2H, m), 7.89–8.00 (3H, m), 7.57–7.75 (7H, m). ^{19}F NMR (δ, 400 MHz, DMSO): 60.80–60.85 (m). ^{13}C NMR (δ, 100 MHz, DMSO): 145.21 (2C), 132.78 (2C), 131.88 (2C), 131.51 (2C), 129.92 (2C), 129.67 (2CH), 129.43 (2CH), 128.21 (2CH), 127.33 (2CH), 126.57 (2CH), 125.82 (2CH), 125.63 (2CH), 124.39 (2CH), 123.64 (2CH). FT-IR (ν_{max}): 1928 (w), 1801 (w), 1737 (w), 1614 (w), 1577 (w), 1542 (w), 1463 (w), 1424 (w), 1408 (w), 1391 (w), 1324 (s), 1281 (w), 1234 (w), 1197 (m), 1178 (m), 1165 (w), 1127 (m), 1111 (m), 1070 (s), 1010 (m), 973 (w), 960(w), 920 (w), 902 (s), 865 (s), 846 (s), 800 (s), 785 (w), 762 (w), 738 (s), 718 (w), 669 (m) cm^{-1}.

3.3.7. Preparation of 2,6-bis(3,4,5-trifluorophenyl)anthracene (3,4,5-F_3Ph)

Prepared analogously to o-FPh using 3,4,5-trifluorophenylbenzeneboronic acid (2.04 g, 11.60 mmol) yielding an off-white crude solid. Sublimation at a temperature range of 190–215°C under a pressure of 10^{-3} Torr with CO_2 as a carrier gas afforded 3,4,5-F_3Ph as white crystals (Yield 1.22 g, 2.79 mmol, 63%). GC/MS reported an elution time of 5.560 min with abundance of 2.6×10^6, and also reported an M+ peak of 438.2 m/z compared to a prediction of 438.37 m/z. MP: 220–230

°C. ^{1}H NMR (δ, 400 MHz, DMSO): 8.65–8.70 (1H, m), 8.58–8.63 (1H, m), 8.49–8.53 (1H, m), 8.38–8.41 (1H, m), 8.18–8.27 (2H, m), 8.08–8.13 (1H, m), 7.86–8.00 (4H, m), 7.59–7.66 (1H, m). ^{19}F NMR (δ, 400 MHz, DMSO): 60.90–60.93 (s), 134.64–134.78 (d), 162.86–163.22 (m). ^{13}C NMR (δ, 100 MHz, DMSO): 151.88 (2C), 151.47 (2C), 137.23 (2C), 135.12 (2C), 132.22 (2C), 133.47 (2C), 130.64 (2C), 128.21 (2CH), 127.39 (2CH), 126.48 (2CH), 124.98 (2CH), 115.02 (2CH), 114.89 (2CH). FT-IR (ν_{max}): 1803 (w), 1614 (m), 1592 (w), 1525 (s), 1470 (m), 1439 (m), 1409 (w), 1394 (m), 1362 (m) 1329 (m), 1301 (m), 1277 (w), 1263 (w), 1229 (s), 1173 (m), 1174 (m), 1130 (m), 1102 (w), 1074 (m), 1036 (s), 964 (w), 924 (w), 900 (s), 887 (m), 869 (m), 854 (s), 822 (w), 798 (s), 761 (s), 746 (m), 703 (m), 699 (m), 673 (w), 662 (w) cm^{-1}.

3.4 Electrochemistry

A glass cell and platinum wires for working, counter and pseudo-reference electrodes was used for cyclic voltammetry in a BASi Epsilon potentiostat. Acetonitrile solutions were used in performing cyclic voltammetry (dried by J. C. Meyer solvent purification system and stored over 3 Å molecular sieves) containing 0.1 M tetrabutylammonium hexafluorophosphate (Oakwood) as supporting electrolyte. A scan rate of 100 mV/s was used for all cyclic voltammetry scans. All experiments were referenced to the Fc/Fc+ redox couple of ferrocene at +0.475 V vs. saturated calomel electrode (SCE) [43–46].

3.5 Thermogravimetric Analysis

70 uL alumina crucible were used for TGA analyses, using a TGA/DSC 1 Mettler Tolledo instrument at a heating rate of 5.0 °C min^{-1} under nitrogen gas. 5% weight loss was used as the decomposition temperature (T_d) for all the compounds.

3.6 Crystallographic Characterization

Crystallographic data collection and processing were performed by the X-Ray Core Facility at the University of Ottawa. Crystals were mounted on MiTeGen sample holders using Parabar oil. Data were collected on a Bruker Smart (o-FPh, m-FPh, and p-FPh) or Kappa (m-CF_3Ph, p-CF_3Ph and 3,4,5-F_3Ph) diffractometer equipped with an ApexII CCD detector and a sealed-tube Mo K source (λ = 0.71073 A). During collection, crystals of m-CF_3Ph, p-CF_3Ph and 3,4,5-F_3Ph were cooled to 213(2) K, crystals of m-FPh and p-FPh were cooled to 200(2) K, and o-FPh was collected at room

temperature. Sample cooling was effected via a refrigerated, dry compressed air stream. Raw data collection and processing were performed with the Apex3 software package from Bruker [31. Initial unit cell parameters were determined from 36 data frames from select ω scans. Semi-empirical absorption corrections based on equivalent reflections were applied [32]. Systematic absences in the diffraction data-set and unit-cell parameters were consistent with the assigned space group. Compound p-CF_3Ph crystallized as a non-merohedral twin. The twin law was discovered using CELL_NOW, and accounted for in the absorption correction via twinabs. [33] The twin law was also accounted for during final refinements. The initial structural solutions were determined using ShelxT direct methods, [33] and refined with full-matrix least-squares procedures based on F^2 using ShelXle.[34] Hydrogen atoms were placed geometrically and refined using a riding model. Twin fractions were also refined in ShelXle. The Cambridge Crystallographic Data Centre (CCDC) repository deposition codes for the compounds are as follow: o-FPh (1992977); m-FPh (1992978); p-FPh (1992979); m-CF_3Ph (1992980); p-CF_3Ph (1992981); and 3,4,5-F_3Ph (1992982).

3.7 Electrical Characterization

Organic thin film transistors (OTFTs) were fabricated in a bottom gate top contact configuration by PVD onto Si/SiO_2 organic semiconductor substrates with gold source-drain electrodes deposited atop (W = 1000 μm, L = 30 μm). Substrate preparation, testing instrumentation and measurement/characterization was performed in accordance with our previous publications [4,35]

3.8 Results and Discussion

3.8.1. Synthesis and Purification of 2,6-Anthracene Derivatives

The palladium-catalyzed Suzuki-Miyura cross-coupling reaction was used to synthesize the 2,6-disubstituted anthracenes (o-FPh, m-FPh, p-FPh, m-CF_3Ph, p-CF_3Ph and 3,4,5-F_3Ph) starting from commercially available reagents, as shown in Figure 1. 2,6-DPA was not synthesized, but rather purchased from a distributor (see Section 4.1). The procedure for the aforementioned cross-coupling reactions was based on literature methods [36,37]. Tetrakis(triphenylphosphine) palladium (0) ($Pd(PPh_3)_4$) was employed as the catalyst in a one-pot reaction with 2,6-dibromoanthracene and varying boronic acids in a degassed solvent mixture of NMP and water. Heating of the mixtures overnight achieved full conversion; completion of the reaction was

confirmed by thin layer chromatography. The crude product was isolated by removal of the solvent via vacuum filtration after precipitation in a 1.0 M NaOH solution. The crude was washed with water and dried overnight. Finally, the crude materials were sublimed to obtain each product as a semi-crystalline film in high electronic purity.

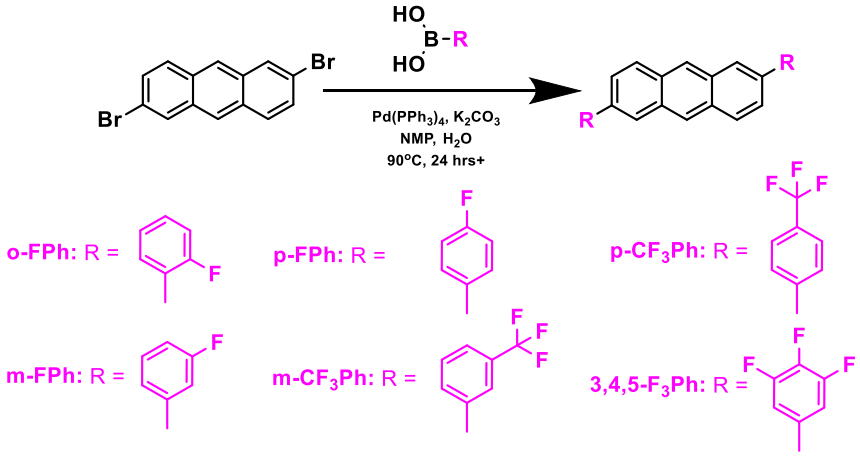

Figure 1. Synthesis of 2,6-disubstituted anthracenes via Suzuki-Miyura cross-coupling reactions using literature methods [35,36].

3.8.2. Optical and Electrochemical Properties

UV-visible (UV-Vis) and photoluminescence (PL) spectroscopy was conducted on all the compounds in dichloromethane (DCM).The maximum peak absorbance ($\lambda_{\max}^{\text{abs}}$), energy gap ($E_{\text{gap}}$), and photoluminescence maximum peak emissions ($\lambda_{\max}^{\text{em}}$) are reported in Table 1.The respective material spectra can be found in the electronic supplementary information (ESI) (Figures S1–S7). A characteristic triple finger-shape of the compounds is clearly identifiable amongst all the spectra. The characteristic peaks observed between 325–425 nm correspond to the π–π* (S_0 → S_1) transitions of the anthracene core [37–41]. The absorption profiles of the compounds display the The E_{gap} quantities are reported between 2.96–3.04 eV for the compounds which is slightly higher than typically observed for 2,6-disubstituted anthracene derivatives [14,20,27,37,42–46].

Table 1. Electrochemical and optical properties of compounds.

	$E_{1/2}$ (V)[a]	E_{HOMO} (eV)[b]	$\lambda_{\mathrm{max}}^{\mathrm{abs}}$ (nm)	E_{gap} (eV)[c]	$\lambda_{\mathrm{max}}^{\mathrm{em}}$ (nm)	Stokes Shift (nm)
2,6-DPA[d]	–	−5.60	360, 379, 400	2.95	411, 436	33
o-FPh	0.86	−5.69	351, 368, 388	3.00	407, 431	40
m-FPh	0.89	−5.69	365, 380, 398	3.04	411, 436	46
p-FPh	0.91	−5.70	345, 366, 387	3.00	412, 436	46
m-CF_3Ph	0.92	−5.72	359, 377, 399	2.97	412, 436	35
p-CF_3Ph	0.99	−5.80	361, 380, 401	2.96	412, 441	36
3,4,5-F_3Ph	0.99	−5.79	357, 369, 389	2.96	413, 436	44

a. Voltage versus saturated calomel electrode (SCE).
b. $E_{HOMO} = -4.80\ eV - \left(E_{onset}^{ox}\ vs \times \frac{Fc}{Fc^{+}}\right)$.
c. The lowest energy absorbance peak from onset was used to calculate theE_{gap};
d. E_{HOMO} obtained from Liu et al. [20].

The Stokes shifts varied slightly between the derivatives with both of the two trifluoromethylphenyl derivatives, m-CF_3Ph and p-CF_3Ph, showing smaller shifts than the fluorophenyl derivatives. Furthermore, there is a lack of mirror image quality and finer details are absent in the emission versus the absorption profiles. This is common, as fluorescent imaging tends to be more sensitive to high background signatures that obscure signals of interest [47]. Lastly, nearly identical emission profiles were observed for the excitation of two higher energy $\lambda_{\mathrm{max}}^{\mathrm{abs}}$, suggesting similar relaxation pathways.

The onset of the oxidation potential obtained by cyclic voltammetry (CV) was used to estimate the HOMO level energy. Dilute acetonitrile solutions of each compound were used for CV with 0.1 M *n*-Bu_4NPF_6 as the supporting electrolyte [46,48–51]. The stacked CV spectra can be found in the ESI (Figure S14). By adding the E_{gap} from UV-vis to the HOMO energy level determined from

CV, the LUMO energy levels could be estimated, resulting in a full energy level diagram for each compound, as shown in Figure 2.

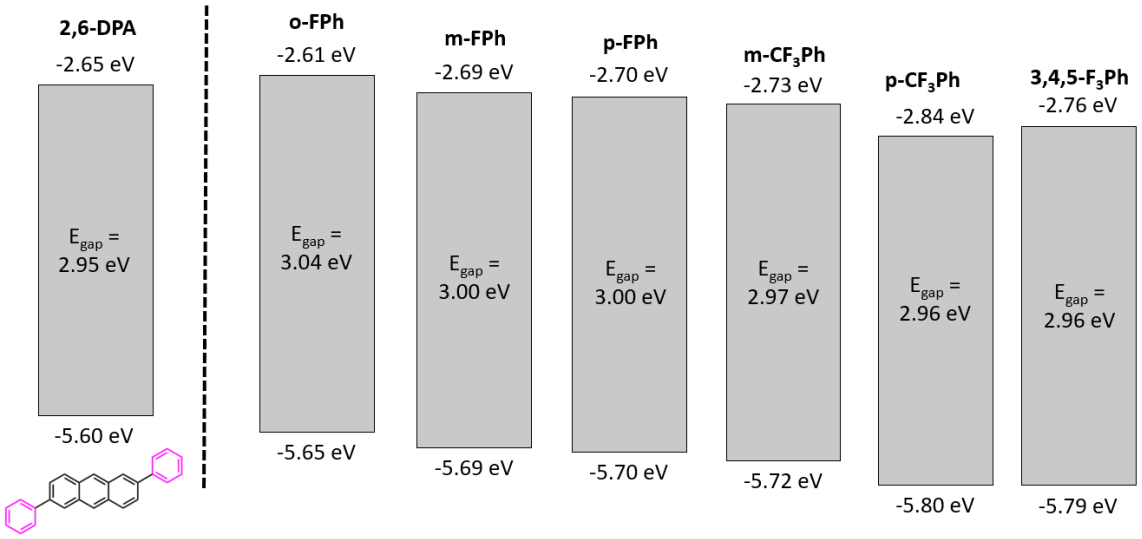

Figure 2. Energy level diagrams of compounds, plus 2,6-DPA for a non-fluorinated baseline [20, 21].

In general, the energy level diagrams suggest there is a noticeable drop in the energy levels of the compounds with more fluorination relative to 2,6-DPA. This is consistent with fluorine-base moieties acting as electron withdrawing groups leading to a drop in the frontier orbital energy levels, especially of the HOMO energy level [52–54]. This result indicates that despite the compounds having generally comparable energetics and oxidative stability, there might be a perceptible difference in performance on account of varying charge injection barriers between the Fermi work function of a selected metal electrode and the frontier orbital energy levels.

3.8.3 Thermogravimetric Analysis

The thermal stability of an OSC in a device is equally as important as the energetics for proper device functionality. High phase transition temperatures (i.e., fusion temperature) and decomposition temperatures are optimal in order to avoid morphologically changes in a thin film of a device, which would ultimately lead to its failure. Therefore, the melting points (T_m) and decomposition temperatures (T_d) were measured for each compound and are tabulated in Figure 3. Contrary to the energetic and optical properties, the type of moiety attached to the 2,6-position of

the anthracene core resulted in considerable differences in the melting point and decomposition temperature between the molecules. Thermogravimetric analysis (TGA) was used to determine the decomposition temperature whereby 5% weight loss would correspond to the T_d of a compound. TGA was performed in a nitrogen atmosphere at a ramp heating rate of 5.0 °C min^{-1}. 2,6-DPA was examined as well as a non-fluorinated base molecule. It was observed that the decomposition temperature of p-CF_3Ph was the highest (289 °C) among the compounds that we synthesized and purified–a trifluoromethylphenyl anthracene derivative. The decomposition temperature of the remaining fluorophenyl derivatives were significantly lower (225 °C–232 °C). Interesting, the melting point of p-CF_3Ph was consistently the highest as well (285 °C–290 °C). These results are indicative of solid-state packing with stronger and more intermolecular interactions, particularly for p-CF_3Ph and 2,6-DPA that show higher melting point and decomposition temperature.

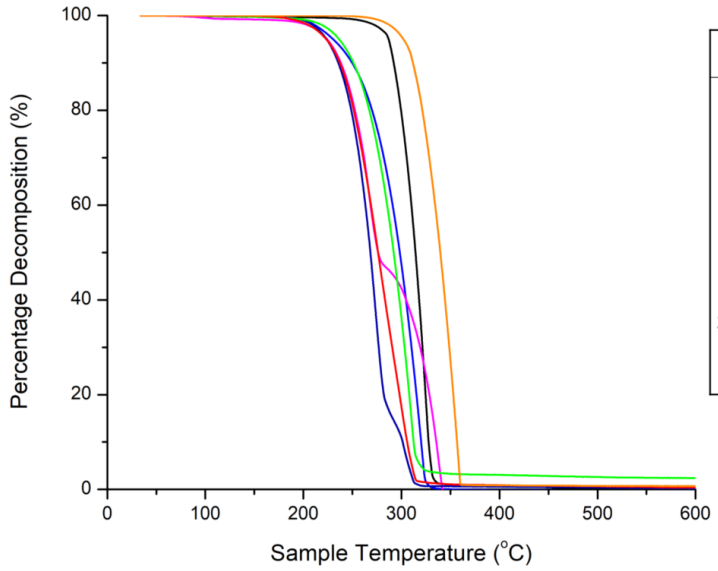

	T_m (°C)	T_d (°C)
o-FPh	195-205	231.75
m-FPh	250-258	225.58
p-FPh	255-265	225.08
m-CF_3Ph	160-170	237.58
p-CF_3Ph	285-290	287.70
3,4,5-F_3Ph	220-230	224.75
2,6-DPA	310-320	302.12

Figure 3. Thermogravimetric analysis curves: o-FPh (blue), m-FPh (magenta), p-FPh (navy), m-CF_3Ph (green), p-CF_3Ph (black), 3,4,5-F_3Ph (red), and 2,6-DPA (orange), as well their associated melting point (T_m) and decomposition temperatures (T_d) (corresponding to 5% weight loss).

3.8.4. Single Crystal X-Ray Diffraction

To gain insights on the structure–property relationship of 2,6-disubstituted anthracenes, single crystals of the compounds were grown using dynamic vacuum sublimation, and their solid-state architectures were elucidated using X-ray diffraction and are depicted in Figures S8-S13 of the

ESI. Crystallographic parameters are presented in Table S1 and Table S2 of the ESI. The Cambridge Crystallographic Data Centre (CCDC) repository deposition codes for the compounds' crystal structures are listed in Section *4.4 Crystallographic Characterization*. At the molecular level, the anthracene frameworks are relatively planar to within $0.028 \pm 1.0 \times 10^{-3}$ Å, indicative of little to no distortion about the anthracene core, as observed for other substituted derivatives [29]. Looking at the molecular framework of the seven derivatives, the mean torsion angle φ between the aryl substituents and the anthracene skeleton range between 7.2° and 48.3° (Figure 4). These angles are substantially lower in comparison to their 9,10-substituted isomers, as steric interactions are mitigated with the peri-hydrogen atoms [29]. Amongst the present molecules with monofunctional phenyl groups, an overall trend indicates an increase in ϕ as the fluoro-based group pivots from the para position inwards to the ortho placement (see Table 2). Interestingly, when comparing ϕ between p-FPh and p-CF_3Ph, the twisting is reduced by almost half. This co-planarization of the aryl groups may be associated with enhanced conjugation of the molecular π-system and the suppression of steric/electronic interactions with the central anthracene.

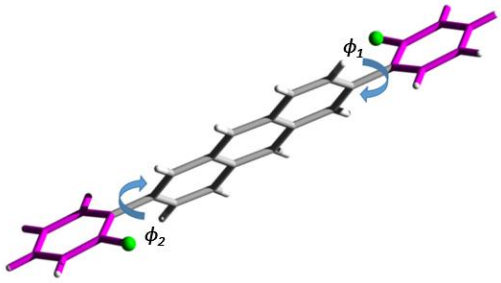

Figure 4. Example of torsion angle location and direction between 2,6-aryl groups to anthracene core of o-FPh derivative (ϕ_1, ϕ_2).

o-FPh, m-FPh, p-CF_3Ph, 3,4,5-F_3Ph crystallize in the monoclinic space group with one half a molecule in the asymmetric unit. p-FPh and m-CF_3Ph as these derivatives crystallize in the monoclinic space group with one unique and two halves of molecule in the asymmetric unit, respectively. Of the fluorine variants, p-FPh and p-CF_3Ph adopt a synonymous herringbone arrangement to that of 2,6-DPA, as shown in Figures 5 and 6, respectively.

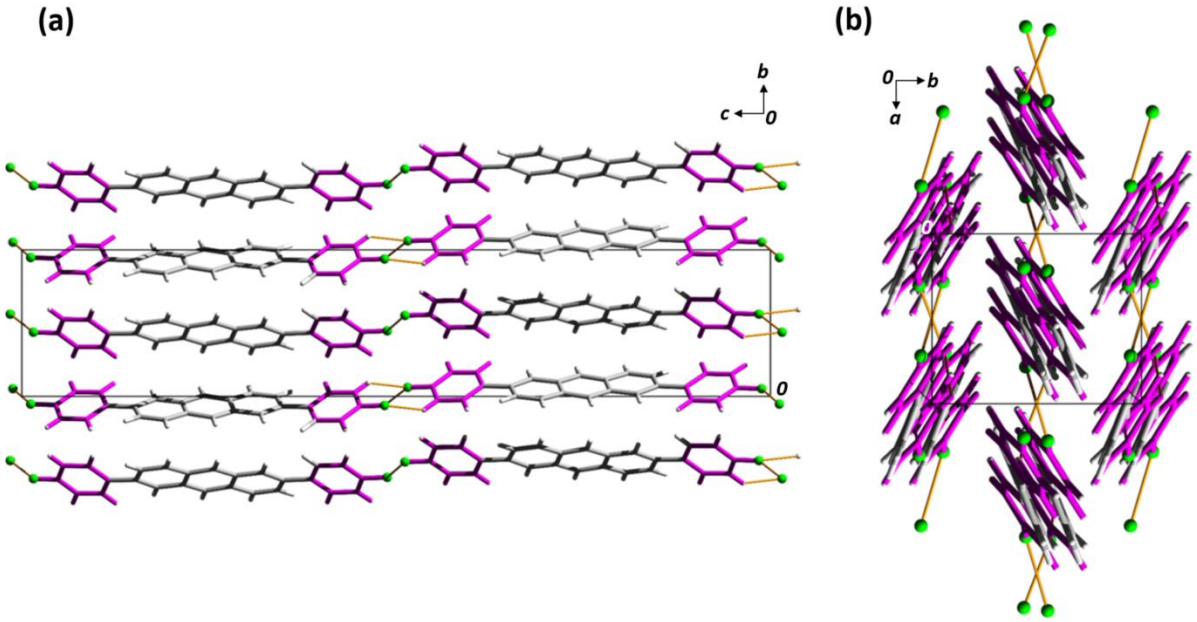

Figure 5. (a) Packing motif of p-FPh viewed along the *a*-direction (b) and *c*-direction. 2,6-position moieties are shown in magenta, and anthracene cores are shown in grey, while fluorine atoms are shown in green. Short contacts between molecules (within array) are shown in yellow.

The addition of the para-substituent appears to have a subtle influence on the overall crystal packing. For example, the herringbone domains are not as tightly packed in comparison to their phenyl counterpart, which is evident by the diminishing number and elongation of the edge-to-face interactions (i.e. C–H π contacts). In 2,6-DPA, sixteen interactions are present for one molecule within a range of 2.84–2.86 ± 1.0 × 10^{-2} Å, whereas six exist for p-FPh within a slightly larger range of 2.87 − 2.88 ± 1.0 × 10^{-2} Å. As for p-CF_3Ph, no interactions within the van der Waals separation exist between neighbouring molecules. Additionally, the herringbone angle increases between edge-to-face molecular pairs from p-FPh to p-CF_3Ph (i.e. DPA = 41.5°; p-FPh = 45.2°; p-CF_3Ph = 47.9°). Interestingly, this trend is not reflected in the centroid distances between anthracene moieties and suggests the less dense arrangement may not necessarily be a steric response, but rather be attributed to the incremental flattening of the herringbone assembly from the general planarization of the molecular framework.

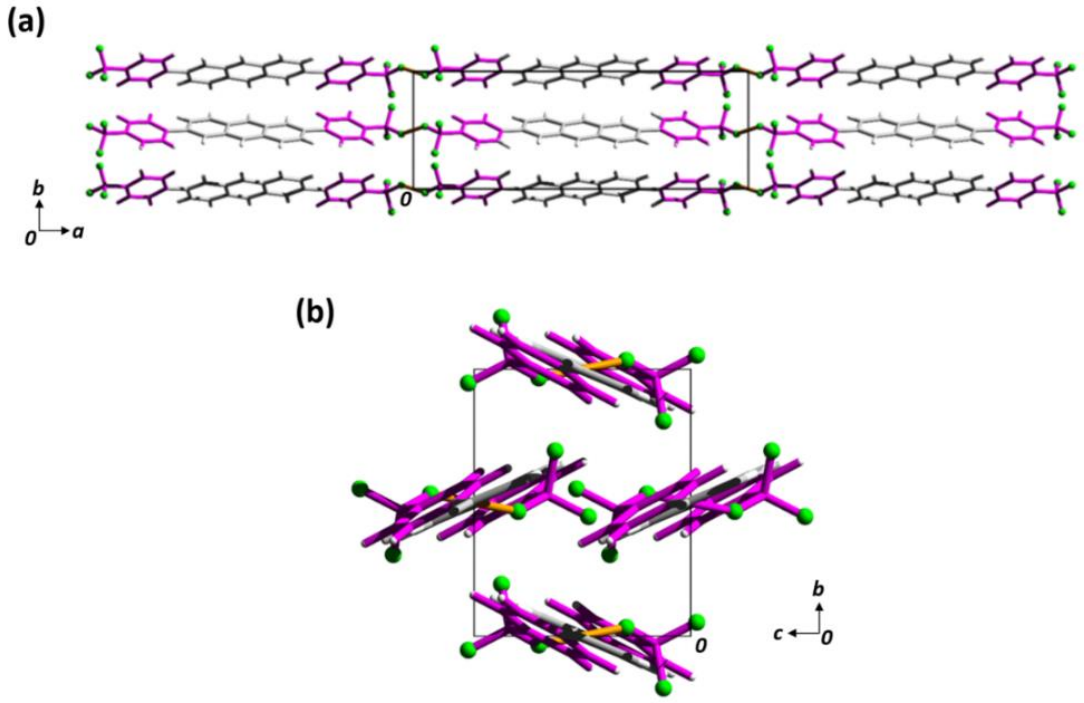

Figure 6. (a) Packing of p-CF_3Ph viewed along the *c*-direction (b) and *a*-direction. 2,6-position moieties are shown in magenta, and anthracene cores are shown in grey, while fluorine atoms are shown in green. Short contacts between molecules (within array) are shown in yellow.

The impact on the solid-state structure becomes more pronounced as the substituents migrate around the phenyl moiety (i.e. meta and ortho substitution vs. para). For both meta-substituted analogues m-FPh and m-CF_3Ph, a herringbone assembly can be observed along the short molecular axis of the anthracene core, but deviates from its classical definition of edge-to-face pairs. When viewing m-FPh and m-CF_3Ph crystals structures along the *a*- and *c*-directions respectively, it becomes apparent that there is an unfavourable degree of slippage along their long molecular axes (Figure S2 and S4). Interestingly, the herringbone angle is only slightly larger than that of its para-substituted cognates (i.e. m-FPh = 49.9°; m-CF_3Ph = 51.8°) (Table 2) and yet, there is an enhancement in the number and degree of intermolecular interactions between edge-to-face pairs. In spite of these ideal structural traits, the degree of π-stacking s reduced between neighbouring anthracene cores due to the aforementioned slippage. As for the o-FPh, the herringbone motif is replaced with a lamellar-like arrangement of the anthracene units, such that three distinct centroid distances exist between neighbouring molecules (Figure 7).

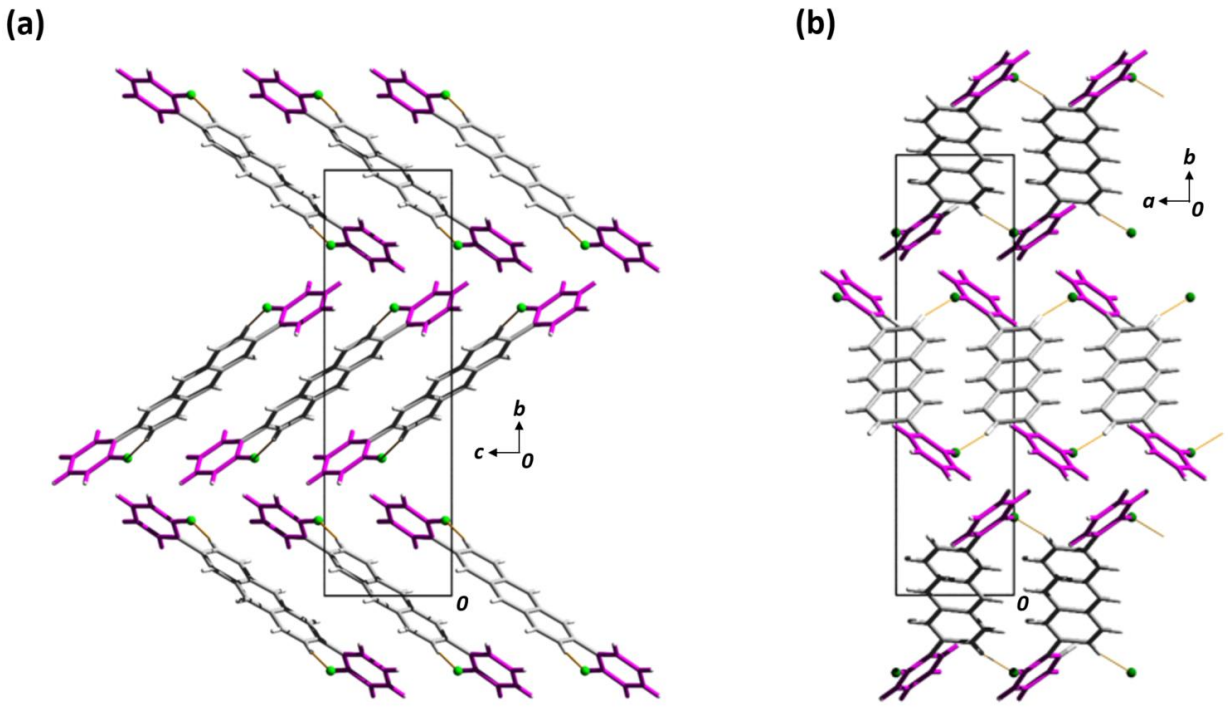

Figure 7. (a) Molecular packing of o-FPh viewed down *a*-direction (b) and *c*-direction. 2,6-position moieties are shown in magenta, and anthracene cores are shown in grey, while fluorine atoms are shown in green. Short contacts between molecules (within array) are shown in yellow.

A herringbone-like arrangement for o-FPh can be seen between adjacent molecules lengthwise (i.e. along the *b*-direction), where edge-to-face interactions occur between the terminal phenyl rings. The dihedral angle between the mean planes of anthracene frameworks is the highest amongst the compounds (i.e. 78.0°), restricting electronic dimensionality in two-dimensions through the lamellar layers parallel to the *ac*-plane.

Table 2. Torsion angle between 2,6-aryl groups to anthracene core (ϕ), herringbone angles, centroid distances and mean plane separation of π-molecule.

	ϕ_1, ϕ_2 (°)	Herringbone Angle (°)	Centroid Distances (Å)	Plane Distances (Å)
2,6-DPA[a]	20.6, 20.6	41.5	6.24	2.21
o-FPh	48.3, 48.3	78.0	6.37, 7.00, 7.40	2.43, 4.24, 1.81
m-FPh[b]	24.0, 24.0 27.3, 27.3	49.9	5.91	2.48, 2.50
p-FPh[c]	13.2, 13.2 14.7, 14.7	45.2	6.07	2.33
m-CF_3Ph	26.2, 26.2	51.8	6.14	2.68
p-CF_3Ph	7.2, 7.2	47.9	6.13	2.48
3,4,5-F_3Ph	39.3, 39.3	23.5	6.99	6.77

Error of the angle measurements is ± 1.0×10^{-1} °. Error of the distances measurements is ± 1.0×10^{-2} Å; a. Values obtained Liu et al. XRD crystal structure [20]. b. m-FPh contains two unique asymmetric units; b. Two unique halves of a molecule in the asymmetric unit; c. One unique molecule in the asymmetric unit.

When 3,4,5-trifluorophenyl substituents are employed along the anthracene backbone, the molecules adopt a herringbone motif resembling that of meta-functionalized derivatives, notably FPh (Figure 8).

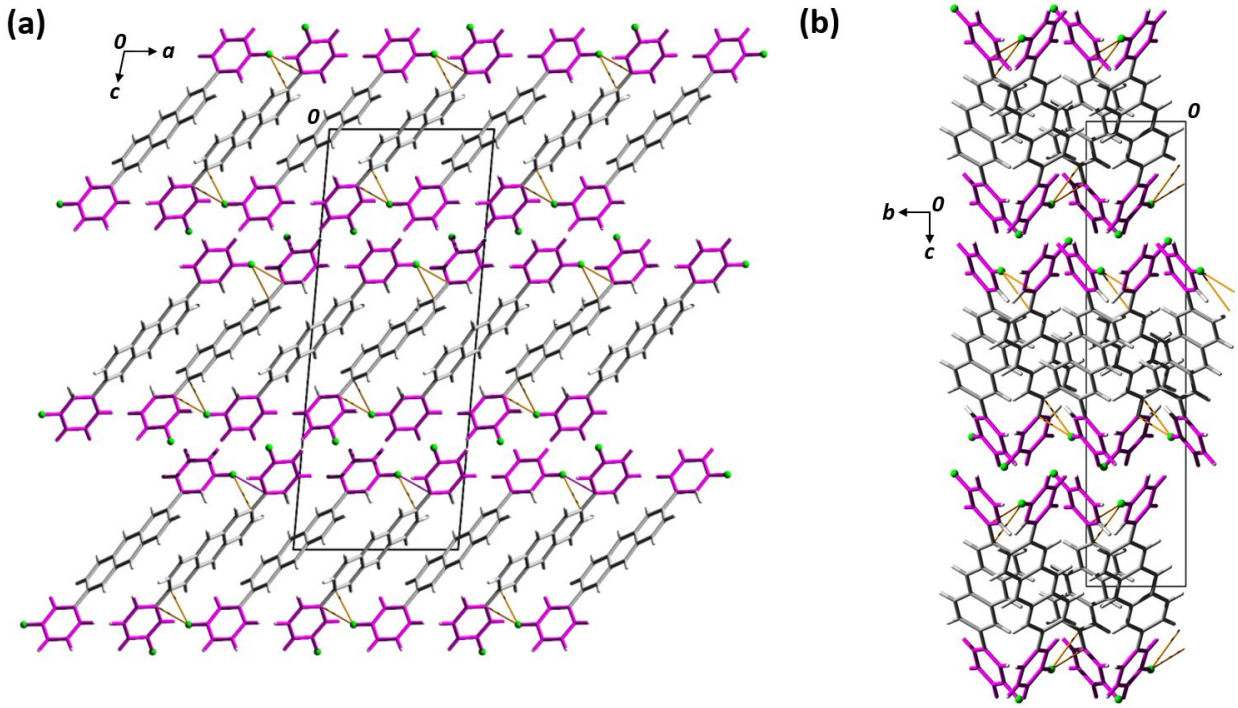

Figure 8. (a) Packing motif of m-FPh along the *b*-direction. (b) Interaction of two intercalating unit cells as viewed down the a-direction. 2,6-position moieties are shown in magenta, and anthracene cores are shown in grey, while fluorine atoms are shown in green. Short contacts between molecules (within array) are shown in yellow.

Instead of molecules inclining along the short molecular axis towards each other, the preference lies along the long molecular axis preventing any favourable C–H/F···π or π···π interactions. This is also supported by the lowest herringbone angle of 23.5°. From the various substitution patterns, replacement of ortho and/or meta- hydrogen atoms appear to have a profound effect on the crystallographic packing of 2,6-susbtituted anthracenes.

3.8.5 OTFT Performance

OTFT were fabricated by physical vapour deposition (PVD) of the anthracene semiconductors on Si/SiO_2 substrates pretreated with octyltrichlorosilane (OTS). A 30 nm thin film of the semiconductor was deposited at a rate of 0.05 Å s^{-1} onto the substrate that was being heated at 50 °C substrates, followed by 50 nm gold electrode in a bottom-gate top-contact configuration (Figure 6a). OTFT characteristics of compounds can be found in Table 3. All OTFTs were characterized

at room temperature, first under an inert environment, and followed by second characterization in air. Figure 9 shows typical output and transfer curves of devices using 2,6-DPA as the semiconducting.

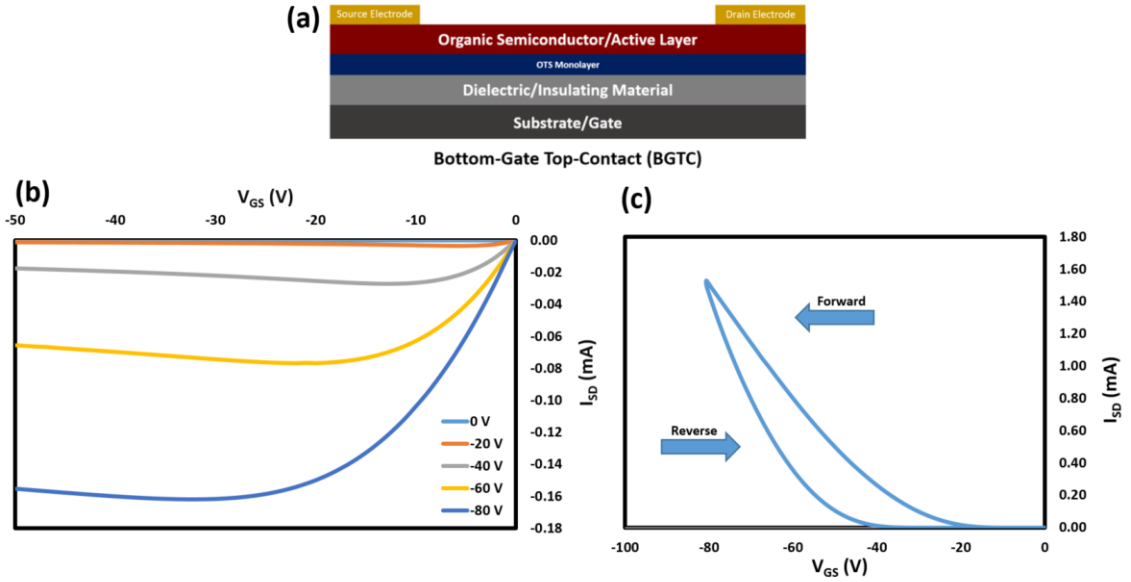

Figure 9. (a) OTFT device architecture (bottom-gate top-contact) used to characterize anthracene derivatives. (b) Typical output curve of 2,6-DPA fabricated OTFTs. (c) Typical transfer curve of 2,6-DPA fabricated OTFTs.

Table 3. Summary of organic thin film transistor performance of 2,6-anthracene semiconductors[a].

Compound	$\delta_{plane,}$[b] (Å)	Testing Atmosphere	$\mu_{avg,h}$ (p-type) ($cm^2\ V^{-1}\ s^{-1}$)	$\mu_{avg,e}$ (n-type) ($cm^2\ V^{-1}\ s^{-1}$)	$V_{T,\,avg}$ (V)	n	$I_{on/off}$
2,6-DPA	2.850	N_2	2.71 ± 1.04	–	−51.0 ± 4.9	57	10^7
		Air	0.145 ± 0.079	–	−49.9 ± 10.8	58	10^6
o-FPh	2.430, 4.344, 1.813	N_2	7.43 ± 2.78 × 10^{-5}	–	−64.8 ± 4.0	32	10^1
		Air	2.34 ± 1.42 × 10^{-5}	–	−87.0 ± 12.3	28	10^1
m-FPh	2.486, 2.503	N_2	1.74 ± 2.02 × 10^{-6}	–	−65.9 ± 22.7	28	10^1
		Air	8.08 ± 3.45 × 10^{-8}	–	−122.2 ± 11.3	35	10^1
p-FPh	2.330	N_2	5.89 ± 0.41 × 10^{-6}	–	−87.3 ± 30.4	31	10^2
		Air	3.52 ± 6.96 × 10^{-5}	–	−75.0 ± 25.9	23	10^1

m-CF_3Ph	2.549	N_2	–	$5.48 \pm 3.48 \times 10^{-6}$	79.8 ± 21.2	20	10^1
		Air	–	–	–	–	–
p-CF_3Ph	2.482	N_2	–	$3.11 \pm 1.27 \times 10^{-3}$	54.7 ± 1.1	35	10^3
		Air	–	–	–	–	–
3,4,5-F_3Ph	3.602	N_2	–	–	–	–	–
		Air	–	–	–	–	–

a. OTFTs were characterized to gate voltages of −80 V; Channel length = 30 μm and electrode width = 3000 μm, where $I_{on/off}$ are orders of magnitude of on/off current ratios, μ_{avg} = average mobility, $V_{T,\ Avg}$ = average threshold voltage, and $V_{T,max}$ = average threshold voltage; b. π–π contacts between adjacent molecules obtained by use of single crystal X-ray diffraction.

All of the compounds, except 3,4,5-F_3Ph, exhibited either p-type or n-type field-effect mobility. Compounds m-CF_3Ph and p-CF_3Ph were the only materials that operated as n-type, but as expected did not produce a field-effect when tested in air, likely due to suppression of n-type behaviour in air [24, 25]. The electron mobility, $\mu_{avg,e}$ of p-CF_3Ph was three orders of magnitude greater than that of m-CF_3Ph. Overall, the hole mobilities ($\mu_{avg,h}$) for all of the new compounds were on the order of $\approx 10^{-6}$ cm^2 V^{-1} s^{-1} with an average threshold voltage (V_T) between −65 V to −125 V, and $I_{on/off}$ ranging between 10^0–10^2 (Table 3). As a comparison, 2,6-DPA was purchased and purified by train sublimation prior to integration into devices. Liu et al. reported the molecular packing and intermolecular interactions of 2,6-DPA are ideally suited for favourable device performance, whereby 2,6-DPA stacks in an edge-on upright orientation, ensuring optimal hole conduction occurs parallel to the channel. This, in combination with relatively short π–π contacts between neighboring molecules (δ_{plane}) and strong C–H···π interactions, contribute to exceptionally high $\mu_{avg,h}$. The use of both 2,6-DPA and p-CF_3Ph have previously been reported in the literature with values similar to our findings [20, 21, 30]. Overall, the functionalization of the 2,6-positions is proving to have a much more significant effect on device performance compared to functionalization of the 9,10 positions [29].

The OTFT performance of o-FPh, m-FPh, p-FPh and m-CF_3Ph were modest, most likely due to weak intermolecular interactions and unfavourable molecular packing in thin film as discussed in the x-ray diffraction section, despite having comparable π–π contact distances (δ_{plane}) to 2,6-DPA, as observed by X-ray crystallography (Table 3). Specifically, the herringbone domains of these molecules are not as tightly packed in comparison to 2,6-DPA, which is evident by the diminishing

number and elongation of the edge-to-face interactions (i.e. C–H···π contacts). Ultimately, this leads to detrimental effects on π-stacking, which in turn would cause poor electrical charge conduction. This is corroborated by the relatively low melting point and decomposition temperatures of the materials as found in the thermogravimetric analysis section, in comparison to the higher performing 2,6-DPA and p-CF_3Ph, suggesting a correlation of lower performing materials to much weaker intermolecular interactions. p-FPh performed poorly even though its molecular packing is analogous to 2,6-DPA and p-CF_3Ph; however, its melting point and decomposition temperature are similar to the rest of the low performing materials.

While the p-type performance of o-FPh, m-FPh, p-FPh, m-CF_3Ph, and 3,4,5-F_3Ph were modest due to weak intermolecular interactions and unfavourable molecular packing, it is still likely that the $\mu_{avg,h}$, and the V_T of 2,6-DPA can be improved with interlayer engineering. 2,6-DPA is an excellent candidate for such device optimization as the morphological and thin-film properties are ideal under non-engineered conditions. Careful application of interlayer materials such as MoO_3 and N,N_0-bis(3-methylphenyl)-N,N_0-diphenylbenzidine (TPD) beneath the Au electrode contacts of a BGTC device can have the effect of reducing the injection barrier by sculpting the charge injection profile relative to the Fermi level of Au and the HOMO of the OSC [55, 56]. Analogous contact engineering techniques, such as the use of Mn or Cr interlayers, may be applied to n-type compounds m-CF_3Ph and p-CF_3Ph [57].

When further examining the electrochemical characterization, it becomes evident that fluorination of the molecules lowers both the LUMO and the HOMO energy levels, which favours electron transport. Both m-CF_3Ph and p-CF_3Ph experienced the greatest drop in HOMO/LUMO levels and they exhibited an $\mu_{avg,e}$. 3,4,5-F_3Ph also experienced a significant drop of their HOMO/LUMO energy levels, however, did not exhibit any field-effect likely associated with its large π–π contact distances (δ_{plane}) (3.602 Å) relative to all other derivatives. This is corroborated by X-ray diffraction that depict loosely arranged herringbone domains diminishing edge-to-face interactions (i.e. C–H···π contacts) of these molecules. The transition from p-type to n-type upon the addition of peripheral fluorine atoms has previously been reported for several materials such as copper phthalocyanines [12, 49, 58] or pentacene [59]. These results suggest that functionalization of the 2,6-positions are powerful handles which can be used to modulate the hole and electron mobility. Furthermore, 2,6-position functionalization simultaneously has significant effects on molecular

packing and intermolecular interactions which must be taken into account as a way to improve OTFT performance.

3.9 Conclusions

Six novel 2,6-anthracene-based molecules were synthesized and their optical, electrochemical, thermal properties and single crystal structures were characterized. It was found that functionalization of the 2,6-positions with various fluorinated phenyl derivatives results in negligible changes in optical behaviour, while dropping the frontier orbital energy levels, especially the HOMO. Moreover, the choice of fluorinated phenyl moiety had noticeable effects on the melting point and thermal stability ($\Delta T_m < 55$ °C and $\Delta T_d < 65$ °C). Organic thin transistors (OTFTs) were fabricated and characterized using the compounds as the semiconducting layer. With the addition of fluorine groups we observed an overall transition from p-type behaviour to n-type behaviour with Au contacts. We also found that the choice of substituent in the 2,6 position led to significant changes to the solid-state arrangement and device performance. These results indicate that functionalization of the 2,6-position of an anthracene core can offer a straightforward way to develop new n-type semiconductors, as well as a powerful handle to potentially improve OTFT device performance.

References

1. Y. L. Chang et al., “Highly efficient warm white organic light-emitting diodes by triplet exciton conversion,” Adv. Funct. Mater., vol. 23, no. 6, pp. 705–712, 2013.
2. J. Qiu, M. Greiner, Z. Liu, and M. G. Helander, “Unlocking the full potential of organic light-emitting diodes on flexible plastic,” Nature Photonics., vol.5 no.12, pp.753-757, 2015.
3. T. M. Grant, D. S. Josey, K. L. Sampson, T. Mudigonda, B.H. Lessard and T. P. Bender, “Boron Subphthalocyanines and Silicon Phthalocyanines for Use as Active Materials in Organic Photovoltaics,” Chemical Record, vol.19, no.6, pp.1093-1112, 2019.
4. O. A. Melville, B.H. Lessard and T. P. Bender, “Phthalocyanine-Based Organic Thin-Film Transistors: A Review of Recent Advances,” ACS applied materials & interfaces, vol.7, no.24, pp.13105-13118, 2015.
5. C. J. Bettinger, H. A. Becerril, D. H. Kim, B. L. Lee, S. Lee, and Z. Bao, “Microfluidic arrays for rapid characterization of organic thin-film transistor performance,” Adv. Mater., vol. 23, no. 10, pp. 1257–1261, 2011.
6. H. Meng et al., “2,6-Bis[2-(4-pentylphenyl)vinyl]anthracene: A stable and high charge mobility organic semiconductor with densely packed crystal structure,” J. Am. Chem. Soc., vol. 128, no. 29, pp. 9304–9305, 2006.
7. H. Z. Chen, M. M. Shi, T. Aernouts, M. Wang, G. Borghs, and P. Heremans, “A novel organic n-type material: Fluorinated perylene diimide,” Sol. Energy Mater. Sol. Cells, vol. 87, no. 1–4, pp. 521–527, 2005.
8. H. Tian, Y. Han, C. Bao, D. Yan, Y. Geng, and F. Wang, “An asymmetric oligomer based on thienoacene for solution processed crystal organic thin-film transistors,” Chem. Commun., vol. 48, no. 29, pp. 3557–3559, 2012.
9. C. Piliego, D. Jarzab, G. Gigli, Z. Chen, A. Facchetti, and M. A. Loi, “High Electron Mobility and Ambient Stability in Solution-Processed Perylene-Based Organic Field-Effect Transistors,” Adv. Mater., vol. 21, no. 16, pp. 1573–1576, 2009.
10. R.-Q. Ma et al., “Flexible active-matrix OLED displays: Challenges and progress,” J. Soc. Inf. Disp., vol. 16, no. 1, p. 169, 2007.

11. A. Glawe, D. Eggerath, and F. Schäfer, “Printing versus coating-What will be the future production technology for printed electronics?,” AIP Conference Proceedings, vol. 1646, no. 1 pp. 87–90, 2015.

12. N. T. Boileau, O. A. Melville, B. Mirka, R. Cranston and B. H. Lessard “P and N type copper phthalocyanines as effective semiconductors in organic thin-film transistor based DNA biosensors at elevated temperatures,” RSC Advances, vol.9, no. , pp. 2133–2142, 2019.

13. L. Zhang, W. Xiao, W. Wu, and B. Liu, “Research Progress on Flexible Oxide-Based Thin Film Transistors,” Applied Sciences, vol 9, no. 4, 2019.

14. M. Chen, L. Yan, Y. Zhao, I. Murtaza, H. Meng, and W. Huang, “Anthracene-based semiconductors for organic field-effect transistors,” J. Mater. Chem. C, vol. 6, no. 28, pp. 7416–7444, 2018.

15. H. Xie, C. Y. Cheng, L. Li, X. Y. Deng, K. K. Yang, and Y. Z. Wang, “Integrating shape-memory technology and photo-imaging on a polymer platform for a high-security information storage medium,” J. Mater. Chem. C, vol. 6, no. 39, pp. 10422–10427, 2018.

16. J. Kommandeur, “Photoconductivity in organic single crystals,” J. Phys. Chem. Solids, vol. 22, pp. 339–349, 1961.

17. O. H. LeBlanc, “Band Structure and Transport of Holes and Electrons in Anthracene,” J. Chem. Phys., vol. 35, no. 4, pp. 1275–1280, 1961.

18. J. T. E. Quinn, J. Zhu, X. Li, J. Wang, and Y. Li, “Recent progress in the development of n-type organic semiconductors for organic field effect transistors,” J. Mater. Chem. C, vol. 5, no. 34, pp. 8654–8681, 2017.

19. M. Chaari et al., “Photoluminescence in: M -carborane-anthracene triads: A combined experimental and computational study,” J. Mater. Chem. C, vol. 6, no. 42, pp. 11336–11347, 2018.

20. J. Liu et al., “Thin film field-effect transistors of 2,6-diphenyl anthracene (DPA),” Chem. Commun., vol. 51, no. 59, pp. 11777–11779, 2015.

21. J. Liu et al., “High mobility emissive organic semiconductor,” Nat. Commun., vol. 6, pp. 1–8, 2015.

22. L. Yan et al., “Influence of heteroatoms on the charge mobility of anthracene derivatives,” J. Mater. Chem. C, vol. 4, no. 16, pp. 3517–3522, 2016.

23. A. Li et al., “Highly responsive phototransistors based on 2,6-bis(4-methoxyphenyl)anthracene single crystal,” J. Mater. Chem. C, vol. 5, no. 22, pp. 5304–5309, 2017.

24. S. Brixi, O. A. Melville, N. T. Boileau, and B. H. Lessard, “The influence of air and temperature on the performance of PBDB-T and P3HT in organic thin film transistors,” J. Mater. Chem. C, vol. 6, no. 44, pp. 11972–11979, 2018.

25. J. Mai et al., “Effects of Ambient Gases on the Electrical Performance of Solution-Processed C8-BTBT Thin-Film Transistors,” Nanoscale Research Letters, vol.14, no.1, pp.1-8, 2019.

26. S. Brixi, O. A. Melville, B. Mirka, Y. He, A. D. Hendsbee, H. Meng, Y. Li and B. H. Lessard; “Air and temperature sensitivity of n-type polymer materials to meet and exceed the standard of N2200,” Scientific Reports, vol.10, no. 1, p.4014, 2020

27. J. Liu et al., “Enhancing field-effect mobility and maintaining solid-state emission by incorporating 2,6-diphenyl substitution to 9,10-bis(phenylethynyl)anthracene,” J. Mater. Chem. C, vol. 5, no. 10, pp. 2519–2523, 2017.

28. M. M. Payne, S. R. Parkin, J. E. Anthony, C. C. Kuo, and T. N. Jackson, “Organic field-effect transistors from solution-deposited functionalized acenes with mobilities as high as 1 cm2/V·s,” J. Am. Chem. Soc., vol. 127, no. 14, pp. 4986–4987, 2005.

29. Vorona, M. Y.; Yutronkie, N. J.; Melville, O.; Daszczynski, A. J.; Agyei, K. T.; Brusso, J. L.; Lessard, B. H., “Developing 9,10-anthracene Derivatives: Optical, Electrochemical, Thermal, and Electrical Characterization,” Materials, vol. 12, no. 17, pp. 1–16, 2019.

30. S. Ando et al., “Novel p- and n-Type Organic Semiconductors with an Anthracene Unit,” Chemistry of Materials, vol. 17, no. 6, pp. 2–5, 2009.

31. X. Diffraction, “APEX2 Release 2010,” no. May, 2010.

32. B. Y. R. H. Blessing, “An Empirical Correction for Absorption Anisotropy,” pp. 33–38, 1995.

33. G. M. Sheldrick, “A short history of SHELX,” pp. 112–122, 2008.

34. C. B. Hu, G. M. Sheldrick, and B. Dittrich, “ShelXle : a Qt graphical user interface for SHELXL,” pp. 1281–1284, 2011.

35. O. A. Melville, T. M. Grant, N. A. Rice, B. Wang, P. Josse, B. H Lessard,. Functionalization of commercial pigment Hostasol Red GG for incorporation into organic thin-film transistors. New J. Chem. 2020, 44, 845-851.

36. M. N. Zafar, M. A. Mohsin, M. Danish, M. F. Nazar, and S. Murtaza, “Palladium Catalyzed Heck − Mizoroki and Suzuki − Miyaura Coupling Reactions (Review),” Russ. J. Coord. Chem., vol. 40, no. 11, pp. 781–800, 2014.

37. G. B. Smith, G. C. Dezeny, D. L. Hughes, A. O. King, and T. R. Verhoeven, “Mechanistic Studies of the Suzuki Cross-Coupling Reaction,” J. Org. Chem., vol. 59, pp. 8151–8156, 1994.

38. R. De Angelis, I. Industriale, R. Tor, T. Chimiche, and R. Tor, “Synthesis and Photophysical Properties of 9,10 Disubstituted Anthracenes,” Materials Sciences and Applications, vol. 6, pp. 943–952, 2015.

39. Z. Wang, C. Xu, W. Wang, L. Duan, and Z. Li, “High-color-purity and high-efficiency non-doped deep-blue electroluminescent devices based on novel anthracene derivatives,” New Journal of Chemistry, vol. 36, no. 3, pp.662-667, 2012.

40. Z. Wan, W. Qi, F. Xing, and Y. Li, “Anthracene-based Derivatives : Synthesis , Photophysical Properties and Electrochemical Properties,” Chemical Research in Chinese Universities, vol. 33, no. 4, pp.603-610, 2017.

41. Y. H. Kim et al, “Extremely deep blue and highly efficient non-doped organic light emitting diodes using an asymmetric anthracene derivative with a xylene unit,” Chem. Comm., vol 49, no. 41. pp. 4664–4666, 2013.

42. O. Gidron et al., “Oligofuran-containing molecules for organic electronics,” J. Mater. Chem. C, vol. 1, no. 28, pp. 4358–4367, 2013.

43. H. Usta et al., “Anthracenedicarboximide-based semiconductors for air-stable, n-channel organic thin-film transistors: Materials design, synthesis, and structural characterization,” J. Mater. Chem., vol. 22, no. 10, pp. 4459–4472, 2012.

44. A. Dadvand et al., “1,5-, 2,6- and 9,10-Distyrylanthracenes As Luminescent Organic Semiconductors,” J. Mater. Chem. C, vol. 1, no. 16, pp. 2817–2825, 2013.

45. M. Chen et al., “A Unique Blend of 2-Fluorenyl-2-anthracene and 2-Anthryl-2-anthracence Showing White Emission and High Charge Mobility,” Angew. Chemie-Int. Ed., vol. 56, no. 3, pp. 722–727, 2017.

46. A. Dadvand et al., “Maximizing field-effect mobility and solid-state luminescence in organic semiconductors,” Angew. Chemie-Int. Ed., vol. 51, no. 16, pp. 3837–3841, 2012.

47. C. I. Richards, J. Hsiang, A. M. Khalil, N. P. Hull, and R. M. Dickson, “FRET-Enabled Optical Modulation for High Sensitivity Fluorescence Imaging,” no. 18, pp. 6318–6323, 2010.

48. S. Y. Ding et al., “Construction of covalent organic framework for catalysis: Pd/COF-LZU1 in Suzuki-Miyaura coupling reaction,” J. Am. Chem. Soc., vol. 133, no. 49, pp. 19816–19822, 2011.

49. J. R. Aranzaes, M.-C. Daniel, and D. Astruc, “Metallocenes as references for the determination of redox potentials by cyclic voltammetry — Permethylated iron and cobalt sandwich complexes, inhibition by polyamine dendrimers, and the role of hydroxy-containing ferrocenes,” Can. J. Chem., vol. 84, no. 2, pp. 288–299, 2006.

50. Y. Li, Y. Cao, J. Gao, D. Wang, G. Yu, and A. J. Heeger, “Electrochemical properties of luminescent polymers and polymer light-emitting electrochemical cells,” Synth. Met., vol. 99, no. 3, pp. 243–248, 2002.

51. M. T. Dang, T. M. Grant, H. Yan, D. S. Seferos, B. H. Lessard, and T. P. Bender, “Bis(tri-n-alkylsilyl oxide) silicon phthalocyanines: A start to establishing a structure property relationship as both ternary additives and non-fullerene electron acceptors in bulk heterojunction organic photovoltaic devices,” J. Mater. Chem. A, vol. 5, no. 24, pp. 12168–12182, 2017.

52. O. Jeannin, F. Barrière, and M. Fourmigué, “Trifluoromethyl-substituted tetrathiafulvalenes,” vol. 6226, 2015.

53. H. Nikoofard, “Theoretical study of fluorinated phenylthiophenes as candidate materials for charge-storage applications,” J. Fluor. Chem., vol. 185, pp. 181–186, 2016.

54. L. M. Yudi and L. M. A. Monzo, “Effect of electron acceptor groups on partition coefficient of phenothiazine derivatives at the water j 1,2-dichloroethane interface,” Journal of Electroanalytical Chemistry, vol. 591, no. 1 pp. 46–52, 2006.

55. R. Shiwaku, Y. Yoshimura, Y. Takeda, K. Fukuda, D. Kumaki, and S. Tokito, “Control of threshold voltage in organic thin- film transistors by modifying gate electrode surface with MoOX aqueous solution and inverter circuit applications,” vol. 053301, no. 2015, 2017.

56. S. Wang, “The interface state assisted charge transport at the / metal interface,” The Journal of Chemical Physics, vol.130, no. 9, 2009.

57. O. A. Melville, T. M. Grant, K. Lochhead, B. King, R. Ambrose, N. A. Rice, N. T. Boileau, . J. Peltekoff, M. Tousignant, I. G. Hill, B. H. Lessard, “Contact Engineering Using Manganese, Chromium, and Bathocuproine in Group 14 Phthalocyanine Organic Thin-Film Transistors” Applied Electronic Materials, vol. 10, 2020. Doi:10.1021/acsaelm.0c00104

58. Z. J. Comeau, N. T. Boileau, T. Lee, O. A. Melville, N. A. Rice, Y.Troung, C. S. Harris, B. H. Lessard, A. J. Shuhendler , “On-the-Spot Detection and Speciation of Cannabinoids Using Organic Thin-Film Transistors,” ACS Sens., vol. 10, pp. 2706-2715, 2019.

59. Y. Inoue et al., “Organic Thin-Film Transistors with High Electron Mobility Based on Perfluoropentacene,” 2005. Jpn. J. Appl. Phys. 44 3663.

4.0 General Conclusions:

We developed several novel 9,10-substituted and 2,6-substituted anthracene-based molecules, whereby their optical, electrochemical, and thermal properties were characterized to build a structure-property-mobility relationship for anthracene-based semiconductors. The materials' structures were analyzed by single crystal X-ray diffraction (SC-XRD) and they were incorporated into OTFTs, facilitating the comparison between solid-state arrangements and charge mobility. We determined that substitution of the 9,10-position is an effective way to tune the thermal stability of the materials while having negligible effects on the optical and electrochemical characterization and ultimately frontier molecular orbital energy levels. Furthermore, 9,10-position functionalization was determined to significantly effect the solid-state packing, as observed via SC-XRD. These changes in solid-state packing motifs resulted in OTFTs with modest performance. In a similar approach to 9,10-functionalization, six novel 2,6-anthracene-based molecules were synthesized and characterized. It was determined that 2,6-position functionalization with fluorinated phenyl derivatives resulted in negligible changes in optical behaviour, however had lowered the frontier orbital energy levels, particularly the E_{HOMO} level. Moreover, the choice of fluorinated phenyl group had a clear effect on the melting point temperature and thermal decomposition stability of 2,6-position functionalized molecules (ΔT_m < 55 °C and ΔT_d < 65 °C), but not to same extent as 9,10-functionalization had varied the thermal stability, whereby the T_d varied by as much as 128 °C between certain functionalized derivatives. Furthermore, it is notable that the E_{HOMO} of the 2,6-position functionalized derivatives was greatly reduced with progressively more fluorine substitution at the 2,6-postions than at the 9,10-postions, which is consistent with literature findings on the effect of fluorination on frontier molecular orbitals. Upon electrically testing and characterization, it was observed that the 2,6-position functionalized derivatives had transitioned from p-type behaviour to n-type behaviour with the addition of fluorine groups on the anthracene derivative. In comparison, the 9,10-position OTFT devices had not seen this effect and performed quite modestly, likely due their unfavourable packing motifs resulting in poor intermolecular orbital overlap. Accordingly, it was found that the choice of substituent in the 2,6-position led to significant changes in the solid-state arrangement, as correlated to device performance in an analogous way to the 9,10-position OTFT devices. Consequently, it was determined that functionalization of the 2,6-positions of an anthracene core

can be a useful way to develop new n-type semiconductors, as well as serve as a powerful handle to improve OTFT device performance.

Overall, we have explored and developed several novel anthracene-based molecules to be utilized in OTFTs, as well as uncovered unique molecular packing motifs and related them to OTFT performance characteristics. These results indicate that functionalization of the 9,10-positions and 2,6-positions of an anthracene core is a powerful strategy that can be used to develop new semiconductors of similar structure. These results also indicated that fluorine-based moiety substitutes are uniquely useful in tuning the electrical properties of anthracene-based molecules to be used for OTFT devices.

5.0 Recommendations and Future Work:

This section explores future avenues of research that may be conducted based on the findings and conclusions of this thesis.

Exploring Interlayer Engineering of 2,6-position Anthracenes Molecules:

Interlayer engineering is a technique by which conductive materials such as metals, metal oxides and organic molecules can be deposited between the metal electrodes and active organic semiconductors. In doing so, the charge injection barriers between the Fermi level of the metal electrode contacts and the frontier energy level may be reduced to facilitate for more efficient charge injection. It is likely possible to improve the $\mu_{avg,h}$, and the V_T of 2,6-DPA OTFTs device with interlayer material addition between the Au electrode contacts and 2,6-DPA. 2,6-DPA is an ideal candidate for such device engineering because the thin-film properties and packing morphology are favourable under non-optimized conditions. Careful application of interlayer materials such as MoO_3 and N,N_0-bis(3-methylphenyl)-N,N_0-diphenylbenzidine (TPD) beneath the Au electrode contacts of a BGTC device can reduce the injection barrier by sculpting the charge injection profile relative to the Fermi level of Au and the E_{HOMO} of the OSC. Similar techniques may be applied to n-type compounds, m-CF_3Ph and p-CF_3Ph, using metals such as Mn or Cr as OSC-electrode interlayers.

Industrial Scale-up Engineering:

The primary goal of "scale-up" is to develop an economical, robust, safe and environmentally sustainable process in order to manufacture a needed valuable good. Scale-up of chemical synthesis encompasses process engineering design techniques through which a small laboratory synthetic procedure (typically at a gram-scale) is enlarged in proportion to large-scale production. A reduction in unit manufacturing cost and improved quality are usually required and achieved upon scale-up, leading to a reduced cost to the end consumer while retaining high quality control of the final product. Accordingly, a largely unexplored field of research are the effects of synthetic scale-up of organic semiconducting materials on OTFT function.

There are both theoretical and practical factors that influence the performance of anthracene-derivatives in OTFTs. In theory, an OSC material may have ideal: (1) alignment of the frontier molecular orbital energy level with the source/drain electrodes; (2) solid-state molecular packing arrangement; and (3) ordered stacking and grain density of the thin film morphology, whereby few boundaries and traps optimize charge mobility. Environmental stability and operating conditions are also important considerations that affect overall device performance and longevity, but are commonly overlooked when studying OTFT performance. Practically, an OTFT is highly sensitive to impurity contamination that can detrimentally effect energy level alignment, molecular packing and grain structure, as well as undermine environmental performance and longevity/reliability of operation. This is an inherent issue with organic electronic fabrication techniques, such as PVD and solution processing techniques, including spin-coating, drop casting, and ink-jet printing. Therefore, during fabrication, careful attention must be paid to preventing contamination of the instruments, equipment and the OSC itself. However, contamination may also be sourced from the initial synthetic procedures that were used to derive the OSC. Unfortunately, as scale of synthesis increases, we commonly see a loss of product quality, such that some impurities might inadvertently be introduced into the OSC material during synthesis and/or purification. This is because scale-up of many reactions is not directly translatable from bench-top procedures due to variations in reaction rate and selectivity as functions of the reactor type and size. The primary sources of issues in such a large-scale synthesis can be allocated to the following categories of operational limitations: (1) heat-transfer limitations, whereby reduction in surface area/volume ratio limits heat transfer or vapor-liquid characteristics so that heat-up, cool-down, or temperature maintenance limits are achievable with standard equipment and gas or vapor dissolution and/or evolution are limiting; (2) mass-transfer limitations, whereby sensitivity to mixing (i.e. circulation time, shear, mass transfer between phases, etc.) does effect reactor performance; and (3) time sensitivity, whereby time of addition of a reactant and/or removal of a product in batch/semi-batch mode is a significant variable. Therefore, the combination of byproduct formation risk in a large reaction vessel from poor heating/mixing/timing and the risk of environmental impurity introduction from other unit operations of the process, pose a challenge to maintaining the purity demanded for commercially viable standards (>ppb).

Anthracene-based semiconductors have become a class of their own; however, there are no literature reports of studies examining scale-up and process engineering of anthracene-based molecules or other OSC molecules. Accordingly, I recommend designing a scalable synthetic and purification route that may be used to industrially derive kilogram-scale quantities of anthracene-based OSC, particularly of 2,6-DPA because of its industrial and academic interest. Such an engineered process would facilitate an investigation of batch-to-batch variation of fabricated OTFTs to determine the effects of scale-up on device performance. The findings would show that using chemical engineering techniques and principles, we may be able to scale-up production of key organic semiconductors in order to reduce cost to end consumers, while retaining high quality control of the integrated electronic materials at large synthetic scales.

6.0 Appendix

6.1 ^{1}H NMRs of Developing 9,10-anthracene Derivatives: Optical, Electrochemical, Thermal and Electrical Characterization:

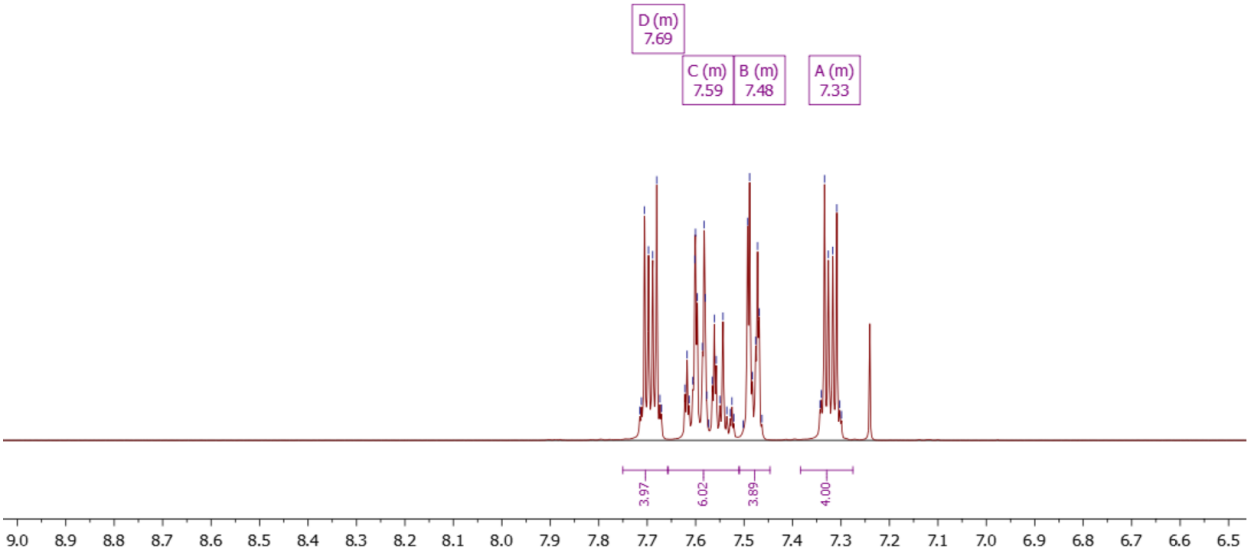

Figure 1: ^{1}H NMR (in $CDCl_3$) Compound 1a.

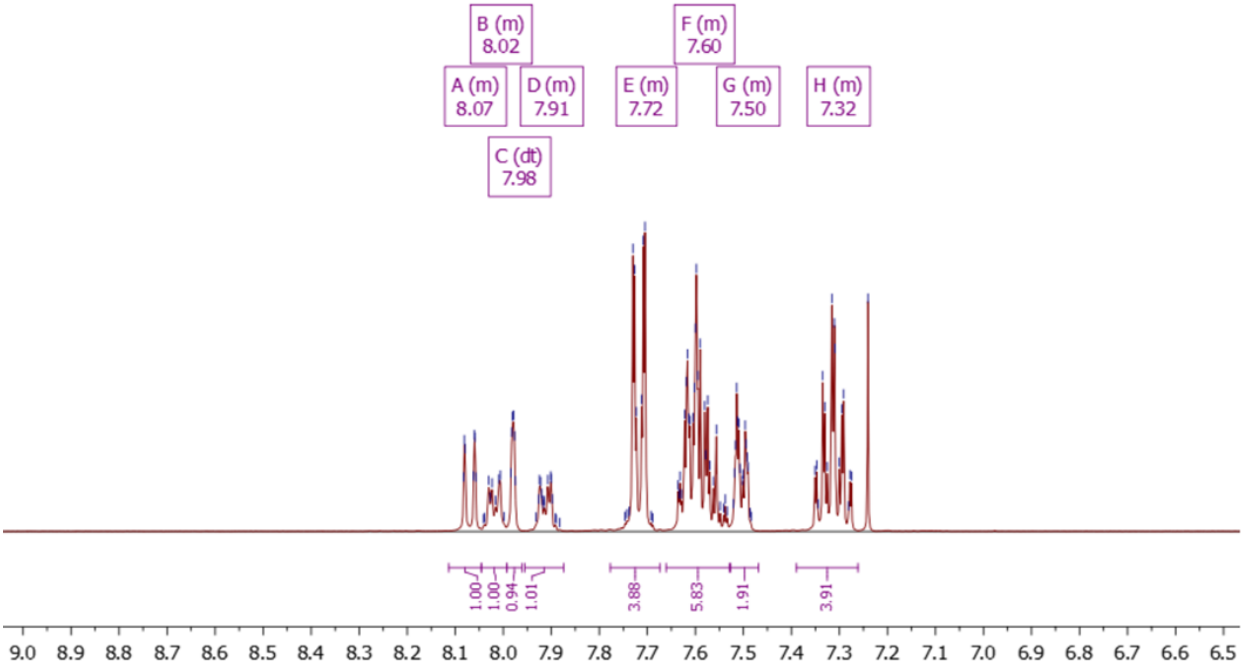

Figure 2: ^{1}H NMR (in $CDCl_3$) Compound 1b.

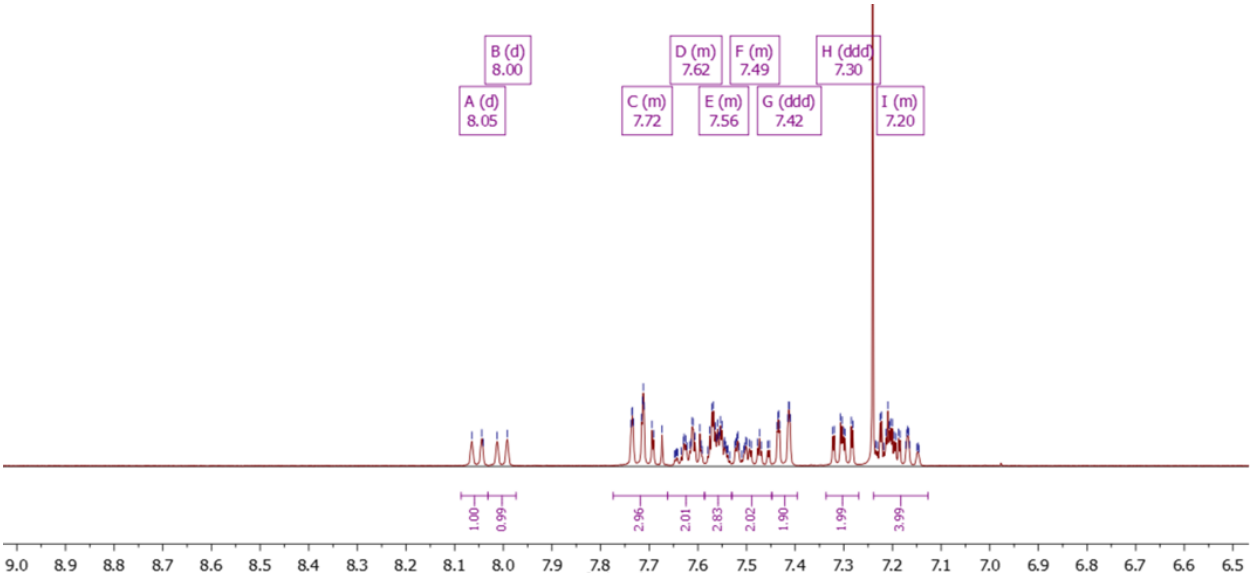

Figure 3: ^{1}H NMR (in $CDCl_3$) Compound 1c.

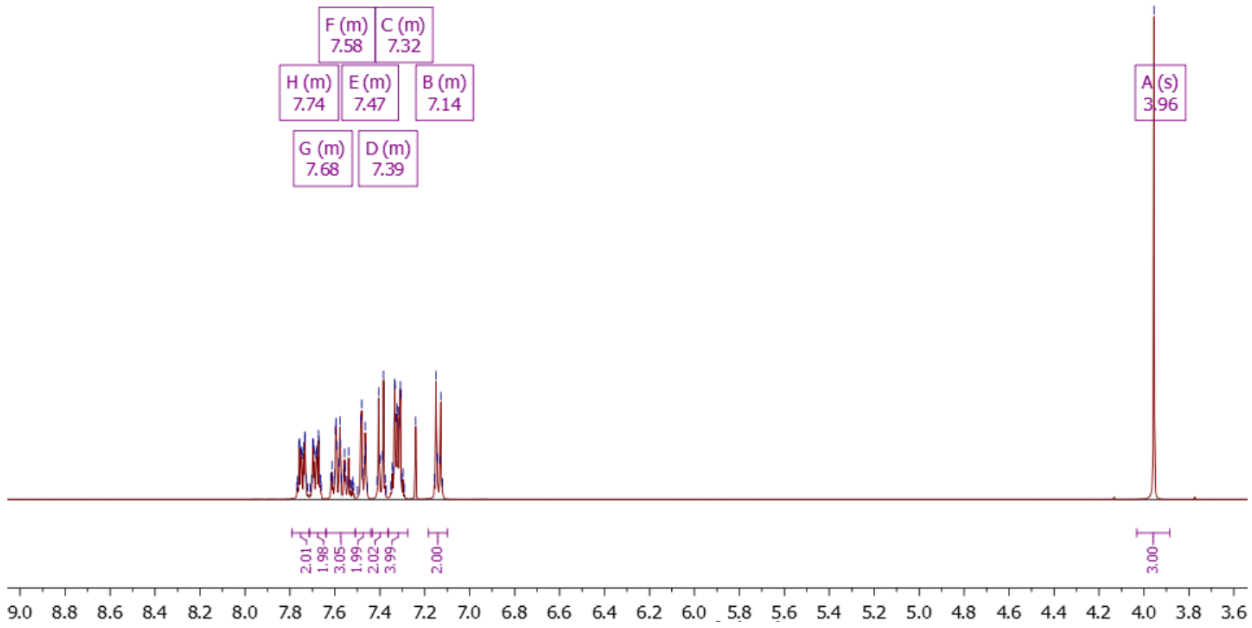

Figure 4: ^{1}H NMR (in $CDCl_3$) Compound 2a.

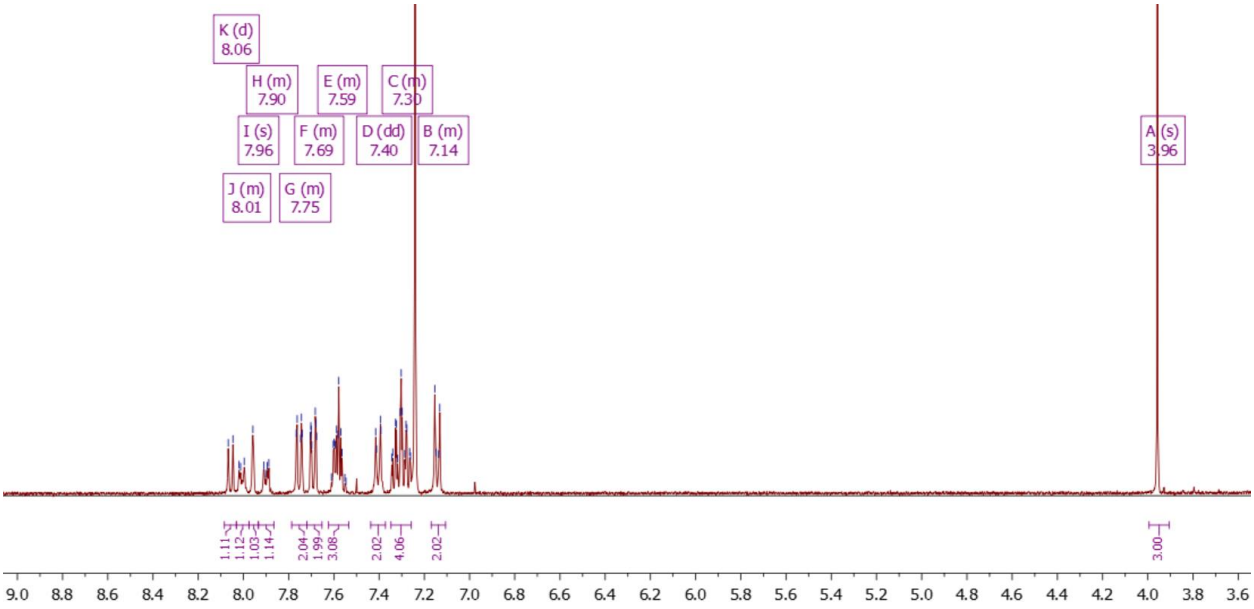

Figure 5: ^{1}H NMR (in $CDCl_3$) Compound 2b.

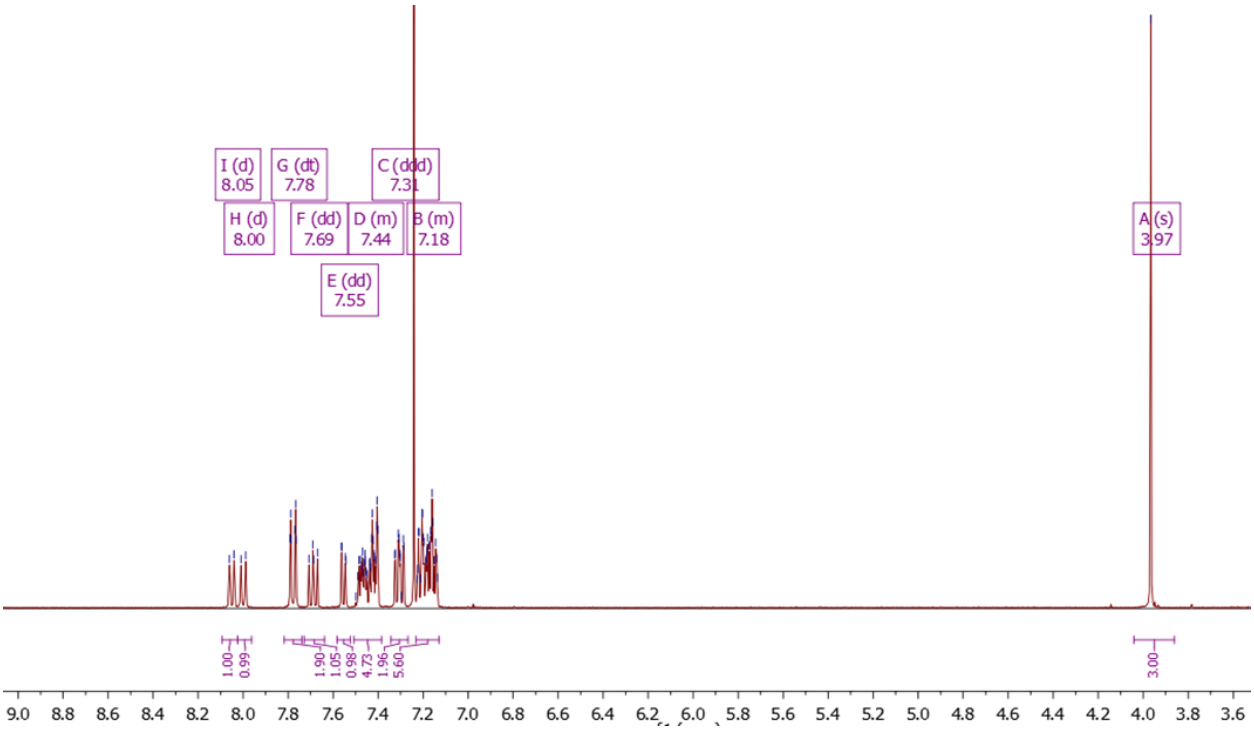

Figure 6: ^{1}H NMR (in $CDCl_3$) Compound 2c.

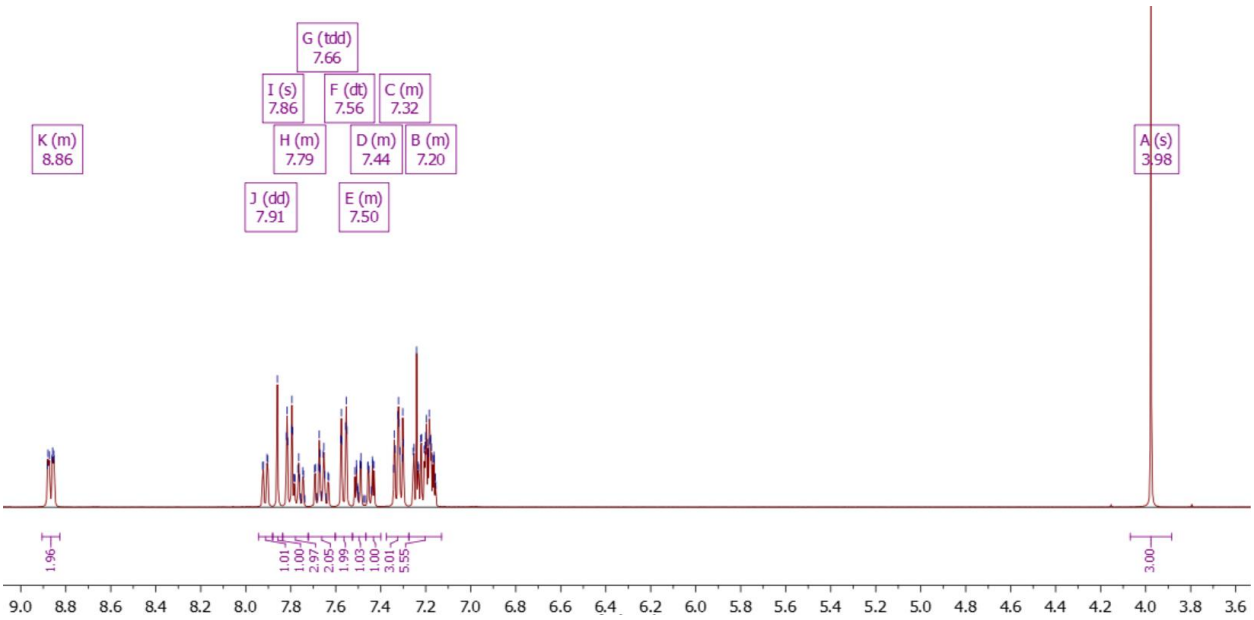

Figure 7: ^{1}H NMR (in $CDCl_3$) Compound 2d.

6.2 ^{1}H NMRs of Developing and Comparing 2,6-anthracene Derivatives: Optical, Electrochemical, Thermal, and Their Use in Organic Thin Film Transistors:

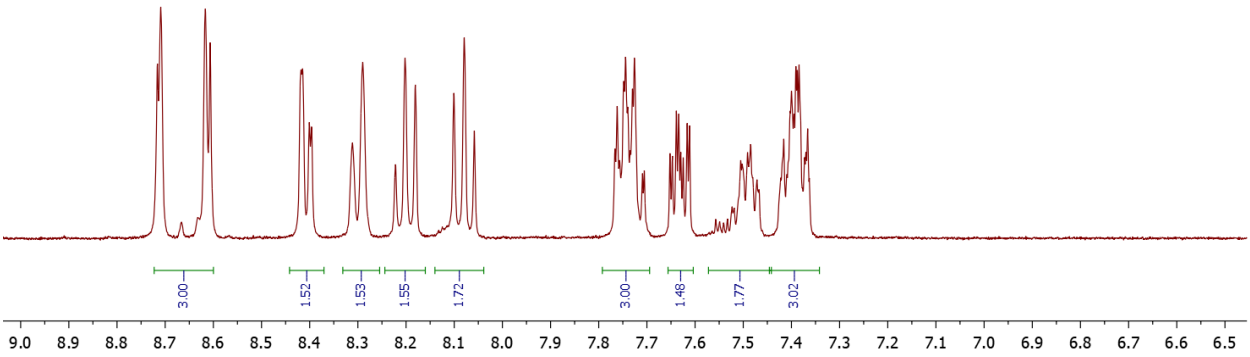

Figure 8: ^{1}H NMR (in DMSO) Compound o-FPh

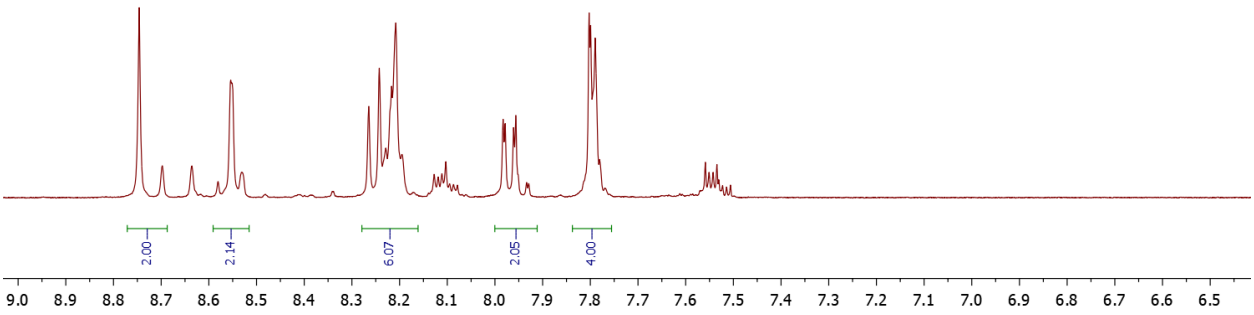

Figure 9: ^{1}H NMR (in DMSO) Compound m-FPh

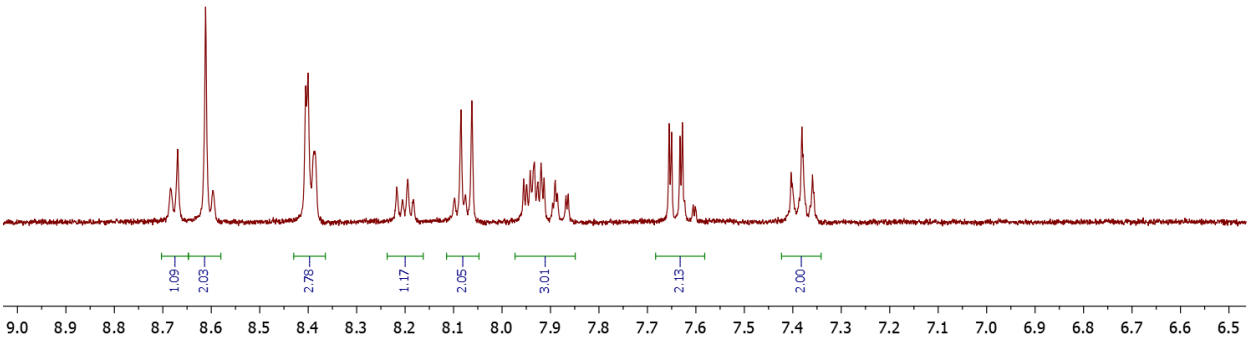

Figure 10: ^{1}H NMR (in DMSO) Compound p-FPh.

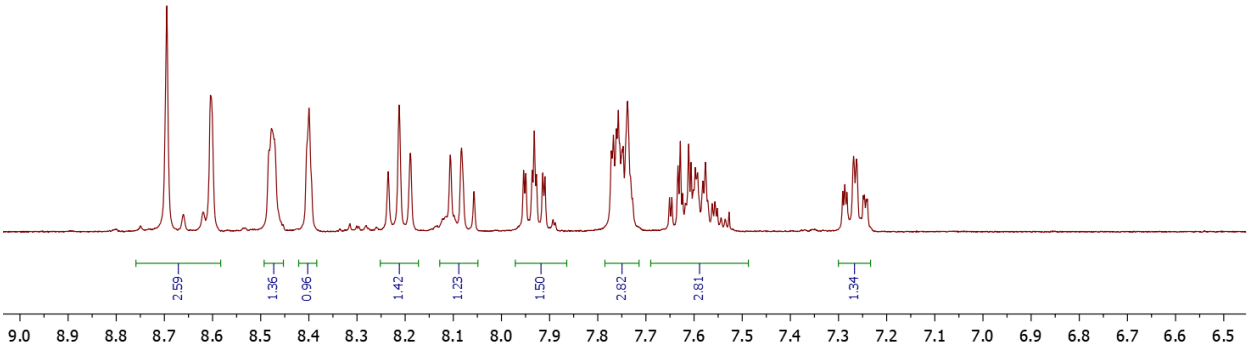

Figure 11: ^{1}H NMR (in DMSO) Compound m-CF_3Ph.

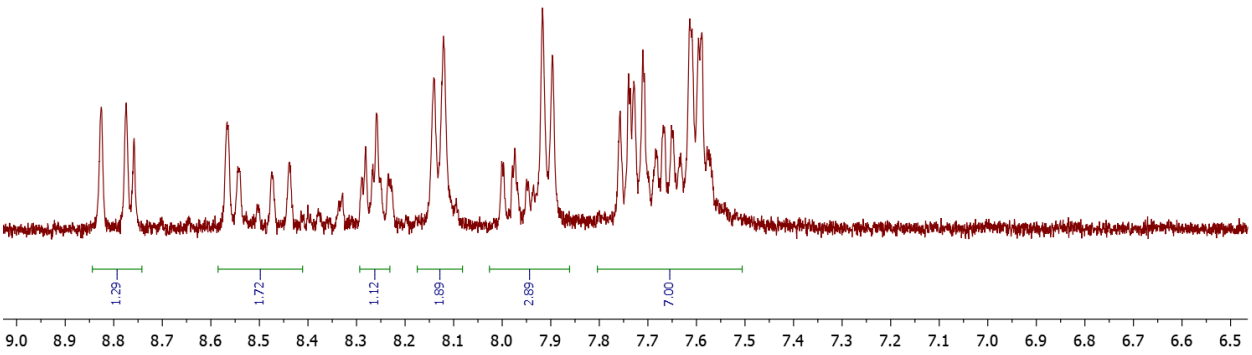

Figure 12: ^{1}H NMR (in DMSO) Compound p-CF_3Ph.

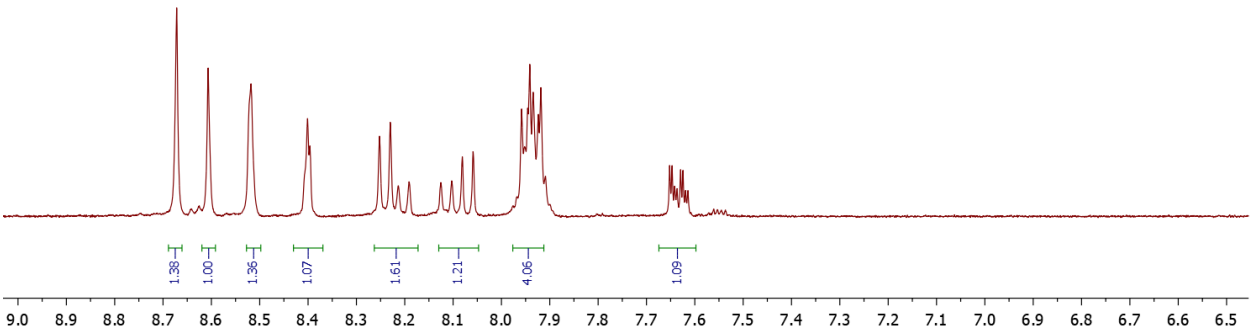

Figure 13: ^{1}H NMR (in DMSO) Compound 3,4,5-F_3Ph.